The Midcourse Space Experiment Point Source Catalog Version 2.3 Explanatory Guide

Air Force Research Laboratory Technical Report No. AFRL-VS-TR-2003-1589

E.R.P., No. 1250

M. P. Egan, S. D. Price, K. E. Kraemer
Air Force Research Laboratory

D. R. Mizuno, S. J. Carey, C. O. Wright, C. W. Engelke
Boston College/Institute for Scientific Research

M. Cohen
Vanguard Research, Inc.
University of California, Berkeley

G. M. Gugliotti
RADEX, Inc.

October 30, 2003

Contents

List of Figures

List of Tables

1 Introduction

Version 2.3 of the Midcourse Space Experiment (MSX) Point Source Catalog (PSC) has several improvements over the initial published catalog, MSX PSC Version 1.2 (hereafter V1.2; Egan et al. 1999). The data processing uses the improved ancillary data processing products developed by the Air Force Research Laboratory (AFRL) Celestial Backgrounds Team to create the MSX Image Products. The catalog now contains sources extracted from nearly all the fields observed by the MSX astronomy experiments, not just the long scan survey observations. Additionally, most of the photometry has been derived from the co-added image data rather than the single scan data.

The improved ancillary products include: dark offset matrices that were updated from the default values used to prepare the first catalog, pointing improvements using infrared observations to update the quaternions that define the pointing history, and the removal or mitigation of various artifacts in the data due to very bright or saturated sources. These improvements and complete background information on the MSX Satellite and SPIRIT III telescope are described by Price et al. (2001).

We briefly describe the infrared telescope system and the MSX astronomy experiments in the next two sections. This is followed by a detailed discussion of the calibration and data processing. Finally, we describe the catalog contents and present analyses of the reliability of the quoted fluxes and positions, and the completeness and reliability of the catalog as a whole. We detail the changes incorporated since the V1.2 Explanatory Guide and provide only a brief description of the aspects of the instrument and processing that have remained the same. The reader is referred to Egan et al. (1999) for a more detailed description of those topics.

1.1 The MSX SPIRIT III Instrument

The SPatial InfraRed Imaging Telescope (SPIRIT III) on MSX was a 35 cm clear aperture off-axis telescope with five line-scanned infrared focal-plane arrays. A Lyot stop at the first focus reduced the off-axis or sidelobe response of the telescope but it also decreases the effective aperture of the radiometer to $\sim$33 cm and the collecting area to about 890 cm^2. A solid H_2 cryostat cooled the entire telescope assembly. Each Si:As BiB array had eight columns with 192 rows of $18''\!.3$ square pixels. The second half the columns in each array were offset from the others by half a row. This provided critical or Nyquist sampling of the optical transfer function in the cross-scan direction under the program criterion that the optics be diffraction limited at 12 μm. The sensor system parameters are presented in Table 1. The Kurucz model for α Lyr adopted by Cohen et al. (1992a) is the source function used in calculating the zero magnitude flux.

Only half the columns were active, as indicated in the table, in order to reduce telemetry demand. However, at least one column was active on either side of the half row offset. Band B was divided in half in cross-scan by two different filters centered on the 4.3 μm atmospheric CO_2 band. This blocked about 10% of the pixels under the filter mask, thus reducing the number of active rows to 76 in each filter; otherwise less than 3% of the focal-plane detectors were non-responsive or rejected for various reasons. The detailed relative spectral response (RSR) for each band is available from Egan et al. (1999).

The SPIRIT III instrument was extensively calibrated both on the ground and in orbit. The ground calibration measured the entire throughput of the instrument by means of a specially constructed cryogenically cooled vacuum chamber to which the telescope was attached. The chamber used a variety of standard sources, all of which were traceable to National Institute for Standards and Technology (NIST) references. The ground calibration quantified the response as a function of the dynamic operating conditions of the instrument. For example, the focal plane warmed up during the mission when the instrument viewed the Earth and as the hydrogen in the cryostat evaporated. The result was a responsivity that was dependent on focal-plane temperature, and an increasing dark current and dark current noise with time. The ground calibration determined the relative variation with temperature of all significant parameters, such as response, linearity, dark current, and flat fielding. The results of extensive on-orbit calibration experiments were used to adjust the initial response parameters and to reduce the photometric uncertainties. The on-orbit references included stellar standards as well as five reference spheres released at various times during the mission. The uncertainties quoted in Table 1 are of the absolute values of the photometry. The precision, which is the usual measure of astronomical observations, is 2–5% in all spectral bands. The sensitivity ranges for the entries in Table 1 are estimates from the beginning and end of the mission.

1.2 The MSX Celestial Background Observations

MSX conducted seven astronomy experiments with the SPIRIT III radiometer. Each experiment consisted of a number of observations, labeled as Data Collection Events (DCEs), that had a duration from 20 to 40 minutes. The Celestial Background (CB) experiments were designated CB01 through CB09 in order of program importance; the objectives of the CB07 Zodiacal Background experiment were subsumed by other experiments and CB08 consisted of only two observations with the interferometer. Figure 1 shows the areas covered by the various MSX experiments on an Aitoff equal-area plot in Galactic coordinates. The 10° wide horizontal yellow band across the center of the plot is the MSX survey of the Galactic plane. The nearly circular, off-center strips (in red) highlight the 4% of the sky that the Infrared Astronomy Satellite (IRAS) did not survey. The patches at various places in the sky are isolated regions observed by MSX containing objects such as galaxies, star-forming regions, and solar system objects.

1.2.1 The Galactic Plane Survey

The point response of the MSX detectors is ~35 times smaller than that of the IRAS mid-infrared detectors. Also, the inherent sensitivity in Band A is ~4 times better than the IRAS 12 μm detectors. These performance factors combined to enable MSX to probe far deeper into the Galactic plane than IRAS. To this end, MSX surveyed the Galactic plane on two experiments. The CB02 survey covered the area within $|b|\lesssim 5°$ with scans along constant Galactic latitude that were 182° long. The initial scan rate of $0^\circ\!.125$/ sec was reduced to $0^\circ\!.1$/ sec during the last two months of the mission to partially compensate for higher dark current noise. Adjacent scans in a single survey were offset by $\sim 0^\circ\!.45$ to produce single coverage in each of the B bands

Table 1: SPIRIT III Spectral Bands

Band	No active cols.	Isophotal λ(μm)	50% peak intensity	Isophotal BW (μm)	Zero mag flux (Jy)	Abs. Photom. Accuracy	Survey Sens. (Jy)	Effective FOV Ω_{EFOV} ($\times 10^{-9}$ sr)
A	8	8.28	6.8–10.8	3.36	58.49	4.1%	0.1–0.2	10.6
B_1	2	4.29	4.22–4.36	0.104	194.6	8.5%	10-30	14.0
B_2	2	4.35	4.24–4.45	0.179	188.8	8.9%	6–18	14.0
C	4	12.13	11.1–13.2	1.72	26.51	5.0%	1.1–3.1	11.7
D	4	14.65	13.5–15.9	2.23	18.29	6.1%	0.9–2	11.3
E	2	21.34	18.2–25.1	6.24	8.80	6.0%	2–6	12.6

1 Jy = 10^{-26} W m^{-2} Hz^{-1}

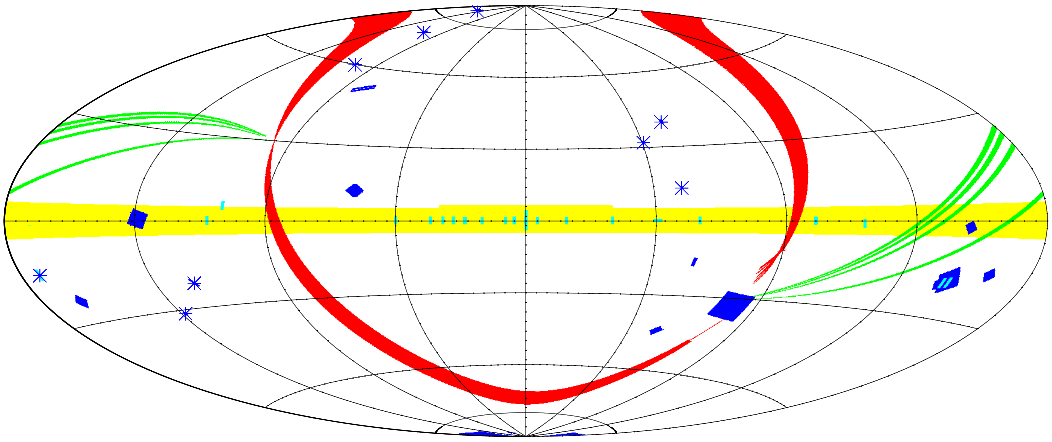

Figure 1: The areas surveyed by the MSX Celestial Background experiments. The map is an Aitoff equal-area projection in Galactic coordinates. The Galactic plane survey is shown in yellow, the Areas missed by IRAS in red, the five near Sun zodiacal scans in green, and the various raster scan observations of targeted areas in blue. Asterisks highlight those raster scans that did not cover a large enough area to show up on the plot.

and redundant coverage in the other bands. A second survey, with scans offset by $0^\circ\!.2$ from the first, covered the Galactic plane to $\pm3^\circ$ latitude and the area in the inner Galaxy between 300° and 120° longitude out to $b\pm4^\circ\!.5$. The 23 CB03 $1^\circ\times3^\circ$ raster scan observations at selected locations in the Galactic plane provided even deeper probes of Galactic structure as well as validation of the reliability and completeness of the Galactic plane survey.

1.2.2 Areas Missed by IRAS

Approximately 4% of the sky is missing from the IRAS catalogs because these areas were either never surveyed or they were surveyed only once before the IRAS mission ended. The "missing" areas are located between ecliptic longitudes of $157^\circ\!.5$–165° (referred to as Gap 1) and 338°–$344^\circ\!.7$ (Gap 2). The CB04 experiment surveyed the two IRAS gaps in order to complete the census of mid-infrared sky. Short (122° or 130°) and long (157° or 161°) scans were interleaved, using cone and clock angle geometry to reproduce IRAS-like coverage patterns. The scan pattern resulted in a minimum of three redundant surveys over each area. Nominally, the scans were along (nearly) constant ecliptic longitude (epoch 1983) at a rate of $0^\circ\!.125$/sec; the scan rate was slowed to $0^\circ\!.0625$/sec late in the mission to recover some of the sensitivity lost by the warming of the focal plane.

Analogously, five CB01 ecliptic pole-to-pole scans (in green on Figure 1) measured the zodiacal foreground close to the Sun, well inside the solar keep-out zones of IRAS and the Cosmic Background Experiment (COBE). The scans surveyed the area between Sun-centered longitudes of 330° and 335° (30° to 25° minimum angle from the Sun). The Earth was used to occult the Sun on this experiment. Price et al. (2003) present the zodiacal results from the IRAS gaps and near-Sun scans.

1.2.3 Mini-Catalogs of Selected Areas

The CB05 experiment also executed raster scans of varying amplitude and scan-to-scan offsets over a number of galaxies, star-forming regions, and three "blank" fields near the Galactic poles. The CB09 experiment raster-scanned fields containing comets or "extinct" comets.

Six MSX observations were required to cover the $10^\circ \times 10^\circ$ field centered on the Large Magellanic Cloud (LMC) with four-fold redundancy. This is the largest of the MSX targeted regions, and the source list from the LMC was the first catalog distributed. Egan, van Dyk, and Price (2001) did a population analysis of the brightest mid-infrared sources in the LMC by cross referencing the MSX source list with objects in the Two Micron All Sky Survey (2MASS). In the MSX PSC V2.3, the LMC data are supplemented by CB01 scans through the region, and the entire LMC source list appears in the higher latitude (defined as $|b|>6^\circ$) subcatalog file of the main survey catalog rather than as a separate supplemental mini-catalog.

Kraemer et al. (2002) presented the results of the MSX observations for eight large, well resolved galaxies (M31, M33, M83, M101, NGC253, NGC4631, NGC4945, and NGC5055). They used the FIND routine of DAOPHOT to identify sources in the images. These positions were used as priors to extract the MSX photometry (as described below in Section 2.4.3), and the Band A fluxes were included for each object. The mini-catalogs of these regions in the PSC V2.3 provide multicolor photometry extracted from the galaxy images, as well as from the Small Magellanic Cloud (SMC), which was not included in the Kraemer et al. study.

Kraemer et al. (2003) present images and source lists for the eight H II and star-forming regions (W3, the Rosette, Pleiades, G159.6−18.5 in Perseus, S263, Orion A, Orion B, and G300.2−16.80 in Chamaeleon) and three blank fields, two at high Galactic latitude and one near the south Galactic pole, that were scanned by MSX. Except for the Orion region, the source lists for these fields contain the image-based Band A fluxes from the mini-catalogs. Kraemer et al. also used FIND to identify fainter sources in the images, but do not provide photometry on these. The Kraemer et al. (2003) source lists provided the position priors for the Orion observations while the W3 and Rosette nebula observations were included in the Galactic plane subcatalogs discussed in Section 2.4.4.

2 Version 2.3 of the MSX Point Source Catalog

The current version of the MSX Point Source Catalog takes advantage of numerous improvements to the data processing. These changes are:

- Processing the telemetry data through CONVERT 6, the final version of the CONVERT routines, with AFRL-specified dark offset matrices and corrections to account for data that standard CONVERT rejected. The most significant of the corrections was to mitigate the effects of bright sources and saturation. The bad pixel mask for the specific gain state and operating mode used for the observation was used rather than the default that included all "out-of-bounds" detectors in every gain state. This reduced the number of rejected detectors.

- Updated Definitive Attitude Files that improved scan-to-scan registration and reduced the formal position uncertainty of sources in the catalog.

- Image-based flux extraction, which produced a higher signal-to-noise ratio (SNR) flux measurement and, consequently, decreased flux uncertainties. This also increased completeness in the MSX spectral bands other than Band A.

- Improved radiometric calibration.
- A candidate source selection threshold defined based on the absolute median of the background noise, rather than standard deviation. This yields better completeness at faint flux densities in high background regions of the Galactic plane.
- A source acceptance criteria based on SNR versus N measurements out of M observations statistics.

2.1 Data Processing and Calibration

SPIRIT III had two operating modes and several gain states that produced a dynamic range of $\sim 10^5$. An internal scan mirror could be used to rapidly sweep out a $1° \times 1°$ to $1° \times 3°$ field at a high data rate (25 Mbps) or the mirror could be fixed to provide longer integration time and a lower (5 Mbps) data rate. The instrument also had three gain states for the mirror scan mode and four gains in the mirror fixed mode. The Celestial Background experiments used the more sensitive mirror fixed mode and scanned the sky by moving the spacecraft. Most of the astronomy measurements used the highest gain but lower gains were used late in the mission when the rising focal-plane temperatures increased the dark offset and, consequently, drastically reduced the dynamic range.

The Space Dynamics Laboratory (SDL) of Utah State University (USU), the SPIRIT III manufacturer, calibrated the entire operating range of the sensor. SDL also created software routines, collectively called CONVERT, that converted the telemetry data stream into scientific units. The MSX program management required that the data be processed with the standard default version of CONVERT in order to produce certified results. The Principal Investigator teams created automated processing that further developed the CONVERT Level 2 output into scientifically usable products, such as this catalog.

The Data Certification and Technology Team (DCATT), with Dr. Thomas Murdock as the Principal Investigator (PI), was responsible for testing and certifying the CONVERT process and Dr. Ray Russell provided direct oversight of the SDL effort. The ground and on-orbit calibration and performance characterization experiments were planned and analyzed by the SDL Performance Assessment Team (PAT), which consisted of SDL engineers, Dr. Ray Russell, and Dr. Russell Walker, a MSX Celestial Backgrounds Team member.

2.2 MSX Data Pipeline and CONVERT Processing

The various data levels used by the MSX program are:

- Level 0 - the downlinked data stream. The Level 0 data are in the form of analog tapes exactly as downlinked and recorded at the ground station. Telemetry data from an observation were downlinked to the Mission Control Center (MCC) at the Applied Physics Laboratory (APL) of Johns Hopkins University (JHU) during satellite passes over the ground station in Columbia, Maryland.
- Level 1 - time ordered telemetry data and data products. The Level 0 analog tapes are converted into computer compatible formatted Level 1 tapes by the JHU/APL Mission Planning Center (MPC). These tapes were reorganized into computer-compatible Level 1A telemetry data that have been time-ordered for each DCE and separated by MSX instruments. The Level 1A data were sent concurrently to the SPIRIT III Data Processing Center (DPC) at USU/SDL and to the AFRL Data Analysis Center (DAC).
- Level 2 - calibrated raw data

- Level 3 - reduced data suitable for analysis; this catalog and the Galactic plane images are examples
- Level 4 - analyzed science results

2.2.1 Data Processing Center at SDL

The USU/SDL SPIRIT III Data Processing Center (DPC) Pipeline provided the DPC Products that are needed to process Level 1A data through CONVERT into Level 2 data. The DPC Pipeline software strips out housekeeping information and the calibration sequences for the DCE; the internal calibration sequences at the beginning and end of a DCE contain dark offset and stimulator measurements. The Pipeline flags anomalies such as "glitches" and saturated detectors and calculates the first four standard statistical parameters (mean, standard deviation, skew, and kurtosis) for each detector in $\sim$33 second blocks, called scenes. Data taken when the sensor was outside of its certified "operational envelope" is flagged in the Radiometer Anomaly file. The DPC also distributes the Radiometer Instrument Product files (RIPs) that are the calibration coefficients necessary to convert Level 1A into Level 2 files. These products essentially define the calibration of the infrared instrument for each DCE.

2.2.2 Definitive Attitude Files

The APL Attitude Processing Center (APC) generated the pointing time history in the form of quaternions for each DCE and issued the result as a Definitive Attitude File (DAF). The APC combines attitude history from the spacecraft gyroscopes with updates from the star camera and SPIRIT III pointing offset from the spacecraft optical fiducial reference. The SDL software, Pointing CONVERT, converts this information into Earth Centered Inertial (ECI) coordinates and corrects the inertial pointing for annual and spacecraft aberration.

Unfortunately, the APC was unable to achieve the mission goal of $1''.8$ (1/10 detector) pointing accuracy for a variety of reasons, some understood and some not. Large discontinuities could occur when the star tracker lost lock, either because of an insufficient number of stars in the field or by being swamped by glints or off-axis sunlight. Discrepancies after the sensor reversed direction on the raster scan measurements were never adequately explained or accounted for in the DAF files. The AFRL processing team corrected the DAFs using the procedures described by Price et al. (2001). Briefly, the brighter Band A sources were selected from each DCE with the point source extractor (PSX) described in Section 2.4 and using the initial positions from the APL DAF. These sources were associated with stars in the MSX astrometric catalog (Egan and Price 1996) or with 2MASS objects when too few of astrometric sources were available (such as along the Galactic plane). A least squares cubic spline fit, with a variable knot spacing of 7° to 10°, of the difference between the observed and astrometric positions was converted into quaternion updates and a new DAF was generated. The average area density of astrometric stars is such that there are 1 to 1.5 astrometric updates per degree of scan. The solution converged after an iteration or two. This correction was translated into a quaternion update for each DCE. The final DAFs for individual scans were about twice as accurate as the V1.2 processing techniques, which sought to correct the APL DAF with a fifth order polynomial boresight correction fit.

Once the best solution was obtained for each DCE, a global correction was found by requiring minimum mean square of the deviations of the multiply observed sources on overlapping scans from the average positions while constraining the solution to the best fit to the astrometric positions. This markedly improved the scan-to-scan registration, which was essential for creating good images from overlapping scans. The global solution further improved the positions by about 20%, to a level that exceeded the program goal.

2.2.3 The CONVERT Process

V2.3 of the MSX PSC was processed with CONVERT 6.0 and the final Instrument Product Files. The only significant change between CONVERT Version 5.2, which was used to process V1.2 of the MSX PSC, and CONVERT 6 is in the processing of the interferometer data; the radiance responsivity scale factors are the same. However, CONVERT 6 has some minor software changes that correct problems that caused CONVERT 5.2 to reject small blocks of the radiometer data. For V2.3, the data were processed with some of the CONVERT default rejection options turned off, such as the saturation flag. By default, all values after saturation were eliminated because the ground calibration was unable to accurately quantify the subsequent dark-offset recovery and the suspected changes in responsivity of the saturated detector. Not only has the Celestial Background processing team estimated and corrected for these effects, but these problems are removed by the cascade-average filtering used to condition the data for the PSX processing. The data were also processed with user-supplied bad-detector masks and dark-offset matrices.

The Radiometer Standard CONVERT processed the data through Equation (1) to obtain Level 2 data:

$$r_{c,d,t} = B\left[\frac{G_{i,a}}{R_d T_a F_a N_{i,d}} L_{i,a}(r_{d,t} - D_{i,d,t})\right] \tag{1}$$

where

$r_{c,d,t} \equiv$ corrected response in counts (Level 2 data) for detector (d) at time (t)
$B[\ \ ] \equiv$ bad detector operation
$G_{i,a} \equiv$ normalization of integration mode (i) for array (a)
$F_a \equiv$ correction of focal-plane response over the field of regard for array (a)
$N_{i,d} \equiv$ non-uniformity correction for integration mode (i) and detector (d)
$L_{i,a} \equiv$ non-linearity correction for integration mode(i) and array (a) (Larsen and Sargent 1997).
$r_{d,t} \equiv$ input data counts (level 1A data)
$D_{i,d,t} \equiv$ dark offset counts for integration mode (i), detector (d) at time (t)
$T_a \equiv$ responsivity correction as a function of temperature for array (a) (Sargent 1997)
$R_d \equiv$ responsivity trending correction for detector (d).

The bad detector operation for integration mode i labels a pixel as either bad or anomalous. A bad pixel designation eliminates data from that detector for the entire DCE. There were 84 dead pixels in the highest mirror-fixed gain state, 36 of which were under the Band B filter mask. The anomalous pixel designation rejects the data from detector d at specified times and time intervals.

Garlick et al. (1996) give explicit analytic expressions for each component of Equation (1), while the cited references provide considerably more detail on that particular component. With the exception of the non-linearity determination, all of these corrections can be, and were, determined without reference to the absolute radiance of the source. Standard CONVERT applies the components of Equation (1) to correct the measured response of a given detector to the same linear response for the array during the lifetime of the mission. Pointing CONVERT applies the focal-plane distortion map to locate the detectors in focal-plane coordinates.

The radiance responsivity for each band was calibrated in the ground chamber against flat plates with known emissivity and accurately measured temperatures that filled the entrance aperture of the telescope. The detector radiance responsivity in units of counts/(W cm^{-2} sr^{-1} detector^{-1}) is derived from the expression:

$$R_{L,a} = \frac{1}{L_{d,t}} r_{c,d,t} \tag{2}$$

where

$$\begin{aligned}
R_{L,a} &\equiv \text{ peak radiance responsivity in counts/(W cm}^{-2}\text{ sr}^{-1}\text{) for array } (a) \\
L_{d,t} &\equiv \text{ calibrated source radiance in W cm}^{-2}\text{ sr}^{-1}\text{ for detector } (d) \text{ at time } (t) \\
r_{c,d,t} &\equiv \text{ correct response in counts (Level 2 data) for detector } (d) \text{ at time } (t).
\end{aligned}$$

The initial irradiance responsivity for each band is derived from the effective beam size that was estimated during the ground based calibration from the relationship:

$$E_a = \frac{\Omega_{EFOV}}{R_{L,a}(1-S)} P[r_c, PRF_a] \tag{3}$$

where

$$\begin{aligned}
E_a &\equiv \text{ measured irradiance in W cm}^{-2}\text{ for array } (a) \\
\Omega_{EFOV} &\equiv \text{ effective field of view (EFOV) solid angle in steradians} \\
1-S &\equiv \text{ out-of-field-of-view scattering contribution to the solid angle} \\
P[r_c, PRF_a] &\equiv \text{ point source extraction operation} \\
r_c &\equiv \text{ correct response in counts (Level 2 data)} \\
R_{L,a} &\equiv \text{ peak radiance responsivity in counts/(W cm}^{-2}\text{ sr}^{-1}\text{) for array } (a) \\
PRF_a &\equiv \text{ point response function (PRF) for array } (a).
\end{aligned}$$

The radiance responsivities were determined on the ground and have remained essentially the same since the final ground chamber calibrations. The final ground-based irradiance responsivities determined through Equation (3) were updated with on-orbit stellar observations that essentially adjusted the value of $\Omega_{EFOV}/(1-S)$ and a scale factor in the point source extraction operation, $P[r_c, PRF_a]$. Such adjustments are implicit in the rescaling of the photometry of stars in the MSX V2.3 PSC to match that from infrared stellar standards.

2.3 Calibration and Radiometer Instrument Products

The Radiometer Instrument Products (RIPs), such as the (focal-plane array temperature dependent) system responsivities and the position dependent point response functions, are the calibration products that apply to all DCEs during the mission. There are also DCE unique terms such as the dark offsets and the bad detector flags. SDL released versions of the RIPs episodically as the calibration was improved. Thus, several versions of the RIPs were issued for each version of CONVERT. There were no significant changes to the

RIPs from CONVERT 5, which was used to process the data in V1.2 of the catalog, to CONVERT 6, which contains the final upgrade to the interferometer processing software that we do not use for the PSC. We used CONVERT 6 to process the observations for the V2.3 PSC to formally conform to using the latest processing routines available.

2.3.1 Calibration Methodology

SPIRIT III was calibrated by three different methods: on the ground with the sensor mated to a cooled vacuum chamber constructed for that purpose; on-orbit using stellar standards; and on-orbit against calibrated reference spheres that were released by the spacecraft periodically during the mission. Each method provides unique information on the sensor radiometric parameters but with sufficient overlap to cross-tie the different calibrations.

The SPIRIT III instrument was attached to the Multifunctional Infrared Calibrator (MIC2), a cryogenically cooled vacuum chamber built by SDL, for the ground calibration. Thurgood et al. (1998) show the chamber in its various configurations and outline the capability in calibrating the SPIRIT III instrument. The ground measurements calibrate the entire system throughput in a fashion that is difficult or impossible to do on-orbit. For example, determination of the relative system spectral responses for the SPIRIT III infrared filter bands (see Appendix A of Egan et al. 1999) can only be done from the ground using a spectral device. Furthermore, the non-linear response of the detectors at high fluxes or the conversion efficiencies for the photon noise are most accurately and efficiently measured with stable sources on the ground. Stable, uniformly emissive extended sources with accurately known radiance were used to calibrate the radiance responsivity of the system. Such sources are rarely available in space (see Price and Kraemer 2004 for a discussion of infrared calibration in space).

Standard stars are true point sources to the system and using them for the on-orbit calibration corrects for the systematic errors arising from the fact that the pinhole used with the ground chamber collimator only approximates a true point source. The MSX Program calibration stars are listed in Table 2 along with their absolute in-band irradiances, in units of W cm^{-2}, in each of the spectral bands. The in-band irradiances are those used in the analysis of Cohen et al. (2001).

One or more of these stars were measured during 94 dedicated calibration DCEs. Five of the DCEs compared either one or two of the stars to the measured fluxes from reference spheres. Eleven DCEs measured the variation of response over the entire $1^\circ \times 3^\circ$ field of regard to determine the position-dependent response function. Stellar calibration measurements were extracted from these observations, although as a

Table 2: MSX Program IR Calibration Stars (W cm^{-2})

Star	Band A	Band B_1	Band B_2	Band C	Band D	Band E	No. Obs.
α CMa	2.833×10^{-15}	1.146×10^{-15}	1.874×10^{-15}	3.195×10^{-15}	1.959×10^{-16}	$1.22\ \times10^{-16}$	35
α Tau	1.308×10^{-14}	4.628×10^{-15}	7.373×10^{-15}	1.570×10^{-15}	9.529×10^{-16}	6.046×10^{-16}	30
α Boo	1.463×10^{-14}	5.566×10^{-15}	8.813×10^{-15}	1.735×10^{-15}	1.059×10^{-15}	6.744×10^{-16}	25
α Lyr	8.196×10^{-16}	3.279×10^{-16}	5.364×10^{-16}	9.259×10^{-17}	5.686×10^{-17}	3.555×10^{-17}	19
β Gem	2.498×10^{-15}	9.759×10^{-16}	1.576×10^{-15}	2.858×10^{-16}	1.762×10^{-16}	1.098×10^{-16}	15
β Peg	7.516×10^{-15}	2.722×10^{-15}	4.365×10^{-15}	9.173×10^{-16}	5.711×10^{-16}	3.596×10^{-16}	14
γ Cru	1.883×10^{-14}	6.426×10^{-15}	1.018×10^{-14}	2.223×10^{-15}	1.359×10^{-15}	8.567×10^{-16}	3
γ Dra	3.111×10^{-15}	1.080×10^{-15}	1.722×10^{-15}	3.729×10^{-16}	2.281×10^{-15}	1.427×10^{-16}	2

by-product. The remaining 88 DCEs consisted of the bi-weekly calibrations that, generally, measured two of the stars in Table 2 on the same DCE. Mazuk and Lillo (1998) also used the standard stars to determine the cross-scan dependent Point Response Functions (PRFs) in each of the MSX spectral bands.

The calibration experiments were all taken in the mirror scan mode and processed through a source extractor, called Canonical CONVERT (Garlick et al. 1996). Canonical CONVERT identifies a source that exceeds a signal to noise of 10, then does a least square fit of the exceedances against the empirical point response function to obtain the flux and position of the extracted source. This procedure works well on reasonably bright isolated sources in regions where the background is flat, precisely the requirements for the MSX calibration stars. The Celestial Backgrounds automated processing used a much more sophisticated extraction routine. Consequently, the irradiances derived by the two extraction processes must closely agree for the SPIRIT III ground and on-orbit calibration pedigree to apply to the MSX PSC. The agreement was confirmed by a comparison of the irradiances extracted on the stellar standards using Canonical CONVERT and the CB source extractor, described in the next section.

2.4 Point Source Extractor Algorithms

The Celestial Backgrounds automated processing software operates on Level 2A MSX data. At this stage, the data have been time ordered, linearized and converted to units of W cm^{-2} sr^{-1} for each detector. The Celestial Automated Process reads the level 2A data and runs it through the USU/SDL Pointing CONVERT software, which assigns a focal-plane position and inertial coordinates to each detector value. The CONVERT software divides the data set into individual scenes of $384 \times 2400 \times M_a$ pixels, where M_a is the number of active columns ($1-4$) on either side of the half detector offset in the band a, 384 is the number of detector rows in the columns on both sides of the offset, and each detector is sampled 2400 times in a scene. The point source extractor (PSX) works on one of these scenes at a time, plus some overlap between adjacent scenes.

2.4.1 Point Source Identification

The background trends and residual detector-to-detector variation in dark offset from the data within a scene are removed with a pseudo-median filter that is applied to the time series of values from each detector, i. The pseudo-median filter produces two files, one containing the low frequency background and the other point sources and high frequency noise. The low frequency files from the CB04 Areas Missed by IRAS and the CB01 Near-Sun Zodiacal Background experiments were further processed to create zodiacal background files (Price et al. 2003; available from the Planetary Data System Dust Node: http://dorothy.as.arizona.edu/DSN). The high frequency data have a mean of approximately zero, and are used to compute the noise variance, σ_i^2, and the mean absolute deviation, for each detector.

After background removal, the high frequency data are ordered into the two-dimensional focal-plane coordinates and the data are convolved with an idealized Point Response Function (PRF) matched filter, which is centered on each output grid position. A gain of 1.7 in signal to noise is typically realized by the matched filtering in Bands B and E, which have two active columns; the eight active columns in Band A produce a gain of about 3.4. The convolved data are thresholded to find positions of candidate point sources. A Levenberg-Marquardt fitting procedure is applied to the candidate point sources to simultaneously determine the point source position (x, y) and radiance. The procedure also calculates a χ^2 goodness of fit measure, and returns a formal covariance matrix that we use as estimates of the errors in the three parameters.

The Cascaded Mini-Max Pseudo-Median Filter A pseudo-median filter is applied to the one-dimensional time series values from a given detector within a sliding window covering an odd number of data points. The center value in the window is replaced by the median of the data points in the window. This filter will remove impulse functions less than one-half of the window width but has little effect on discrete step or ramp variations in the data. Therefore, the median filter can be tuned to filter out point sources and high frequency noise in the MSX data, leaving behind the low-frequency background.

Since the computation of the median grows exponentially with the window size, we adopted a variation of the pseudo-median filter described by Pratt et al. (1984), which retains many of the advantageous properties of the median filter but is computationally simpler. For a window of length L, the pseudo-median, as defined by Pratt (1991), is calculated from the running values of the maxima and minima of the data, D, which are determined over an odd number of M samples centered on the N^{th} data point, d_N. That is:

$$MAX_N(D) = MAX(d_{N-\frac{1}{2}M}, d_{N+1-\frac{1}{2}M}, \cdots, d_{N+\frac{1}{2}M}) \tag{4}$$

$$MIN_N(D) = MIN(d_{N-\frac{1}{2}M}, d_{N+1-\frac{1}{2}M}, \cdots, d_{N+\frac{1}{2}M}) \tag{5}$$

The *MAXIMIN* and *MINIMAX* of the data are then calculated over L samples, where $L = 2M + 1$, by:

$$MAXIMIN_N(D) = MAX(MIN_{N-\frac{1}{2}L}(D), MIN_{N+1-\frac{1}{2}L}(D), \cdots, MIN_{N+\frac{1}{2}L}(D)) \tag{6}$$

$$MINIMAX_N(D) = MIN(MAX_{N-\frac{1}{2}L}(D), MAX_{N+1-\frac{1}{2}L}(D), \cdots, MAX_{N+\frac{1}{2}L}(D)) \tag{7}$$

The *MAXIMIN* value is greater than or equal to the median of the sequence of L values and the *MINIMAX* value is less than or equal to the median of the sequence.

A cascade operator is used to cancel any small biases produced by these operators:

$$C_{AVE} = \frac{1}{2}(MAXIMIN\{MINIMAX_N\{D\}\} + MINIMAX\{MAXIMIN_N\{D\}\}). \tag{8}$$

The cascade operator closely approximates the median of the data and preserves the edge information in the background reasonably well. The MSX images along the Galactic plane show that the background can be highly structured and it is critical that this background be correctly removed for accurate flux estimation of point sources in these regions.

The filter sub-sample length, M, is set by the number of data samples from a given detector within an angular extent defined by:

$$M = 1.75 \times \left(\frac{89\ \mu\mathrm{rad} + 2.44\lambda_{\mathrm{max}}/D}{\mathrm{scan\ rate}}\right) \mathrm{sample\ rate} + 1 \tag{9}$$

The nominal detector size is 89 μrad, the diameter of the primary, D, is 33 cm and the maximum wavelength, λ_{max}, adopted for each filter band is 11 μm (Band A), 13.2 μm (Band C), 16 μm (Band D), and 26 μm (Band E). For the astronomy experiments on MSX, the scan rates range from $0.^\circ125$/sec to $0.^\circ02$/sec (2.181 mrad/sec to 0.349 mrad/sec). The detector read-out rate was 72 Hz, which oversampled the in-scan data at the scan rates used for the astronomy experiments. The sample spacing varied between 30.3 and 4.85 μrad

(2.85 to 17.82 samples per 89 μrad detector) depending on scan rate and number of redundant columns in the array. In angular units, the filter length, L, spans $2\rlap{.}'3$ in Band A, $2\rlap{.}'5$ in Band C, $2\rlap{.}'7$ in Band D, and $3\rlap{.}'5$ in Band E. The background in the B bands was sufficiently flat after the updated dark offset matrices described by Price et al. (2001) were applied that there was no need to use the pseudo-median filter on those data.

Identifying Candidate Point Sources After the filter removed the background, the high frequency content of the noise was estimated and an SNR threshold of 2.8 used to select potential point sources in the scene. First, a two-dimensional matched filter is centered on each point in the output grid for the scene. The dimensions of the output grid are 384 cross-scan $\times$ 2400 in-scan. A subset of the data in a window surrounding the point is weighted by the values of the matched filter at each position within the window. The window is elliptical in data space, where the cross-scan extent is $2R/dx + 2$ samples, and $2R/dy + 2$ samples in-scan. The radius R is the expected extent of the source in pixels defined for each band. The quantities dx and dy are the in-scan and cross-scan sampling intervals, respectively, in terms of fractions of pixels in focal-plane coordinates. For the long scans at $0\rlap{.}^\circ125$/sec, the window size is $10\times M_a$ pixels in-scan (where M_a is the number of active columns on either side of the offset in band a), and 5 detectors cross-scan for each column. There are a total of 400 pixels in the window for Band A at the nominal scan rate but the number can be as much as 2100 pixels at the slower scan speeds.

Theoretically, the optimal filter should use the measured PRFs in each band. However, using the empirical PRFs in each band is computationally expensive as it would require as many as $2100\times384\times2400$ multiplications and additions for a given scene. Since we select and estimate the positions of potential sources, but do not extract their exact parameters at this stage, we use cubic B-splines to represent the PRFs to simplify the matched filtering. The cubic B-splines are a reasonable representation of the PRFs. The noise in the matched filtered scene is then estimated and the scene thresholded to values above this noise level. A given point source may produce a number of data points above the threshold. These are examined to find the local maximum, which is reported as the initial guess of the point source position.

Parameter Estimation Once a potential source has been identified in an MSX spectral band, a, we estimate the source radiance, R_a, and position, $(\xi, \eta)_a$, simultaneously using a χ^2 minimization. We model the data using the cross-scan position dependent PRF, H_a, measured by Mazuk and Lillo (1998). The PRF in each band was measured on-orbit at the top, middle, and bottom of each focal plane as part of the spacecraft calibration. The measured PRF, H', was normalized to a peak value of unity, such that the effective field of view of the PRF is given by

$$\Omega_{EFOV} = \Delta x \Delta y \sum_{k=1}^{M} H_k' \tag{10}$$

where Δx and Δy are the grid sample intervals (in radians) and the PRF is sampled over M values. The measured PRFs were volume renormalized for the point source extraction processing such that

$$H_k = \frac{H_k'}{\sum_{k=1}^{M} H_k'} \tag{11}$$

and

$$\sum_{k=1}^{M} H_k = 1. \tag{12}$$

The data are modeled as the convolution of the PRF with the true object data, without the noise. At a given point i for band a this may be expressed as:

$$d_{a,i} = R_a H_a(x_i - \xi, y_i - \eta). \tag{13}$$

For a single point source then, we calculate the radiance and position by determining the values that minimize the χ^2, which is given by

$$\chi^2 = \sum_{i=1}^{N} \left[\frac{\rho_{a,i} - d_{a,i}}{\sigma_{a,i}} \right]^2 . \tag{14}$$

In Equation (14), $\rho_{a,i}$ and $\sigma_{a,i}$ are the measured values and associated standard deviation within the scene for detector i in band a. N is the number of points in the data window. If we also account for the possibility of blended sources, the quantity minimized is

$$\chi^2 = \sum_{i=1}^{N} \left[\frac{\rho_{a,i} - \sum_{k=1}^{K} R_{k,a} H_a(x_i - \xi_k, y_i - \eta_k)}{\sigma_{a,i}} \right]^2 \tag{15}$$

where K is the number of point sources within the data window. We use the Levenberg-Marquardt technique, adapted from the code described by Press et al. (1992) to simultaneously fit the three parameters and to calculate a formal covariance matrix for the fit.

The datum, $\rho_{x,i}$, is the Level 2 radiance in units of W cm^{-2} sr^{-1}. The χ^2 minimization returns the radiance, R_a, and a refined source position. To determine the irradiance, we must multiply this result by the effective field of view of a PRF data element, ω_{EFOV}.

Mazuk and Lillo provide PRFs that are sampled on a regular grid with a sample interval of $\Delta x = \Delta y = 4.1667 \times 10^{-6}$ radians. The volume normalized PRF of a staring sensor has an effective field of view for the PRF element of

$$\omega_{EFOV}(staring) = \iint H d\Omega = \sum_{k=1}^{M} H_k \Delta x \Delta y = \Delta x \Delta y \sum_{k=1}^{M} H_k = \Delta x \Delta y. \tag{16}$$

However, the area scanned during the integration time must be taken into account. For example, a PRF that is circularly symmetric while staring, will be elliptical when the sensor is scanned. The cross-scan extent of the PRF is unchanged, but the in-scan response is that of the PRF convolved with a box function whose angular width is given by the product of the scan rate of ν radians/sec and the integration time of Δt seconds, that is $\nu \Delta t$.

Noise Estimation Each datum is weighted by a noise value in the parameter fit. The noise for the i^{th} detector at readout frame time, t, has two components: device noise that is inherent to the detector and Poisson noise. These are added in quadrature to derive the variance in the total noise:

$$\sigma^2(i,t) = \sigma^2_{\text{detector}}(i) + \sigma^2_{\text{photon}}(i,t) \tag{17}$$

The detector noise is computed from the 2400 values of the high frequency component of the filtered data in a scene for each detector in the focal-plane array after point sources have been removed. The Poisson noise is the statistical consequence of the fact that the detectors behave as photon counters. In such a case, the variance of the Poisson distribution is equal to the mean, that is:

$$\sigma_{\text{photon}} = A\sqrt{r} \tag{18}$$

where A is the photon noise coefficient, and r the offset and linearity corrected response in counts. The coefficient A was measured during the ground calibration at SDL and is listed in Table 2.52 of the *SPIRIT III Infrared Sensor Ground Calibration Report in Support of CONVERT 5.0* (SDL/97-056) for each band and gain. The conversion coefficients in this table were adopted for the point source extractor to determine $\sigma^2_{\text{photon}}(i,t)$.

2.4.2 Construction of the Catalog

The MSX survey experiments were designed to be highly redundant. All but about 20% of the Galactic plane was surveyed four times, and the coverage is much higher in portions of the IRAS gaps. The LMC, SMC, and most of the star forming regions were nominally covered four times while the deep CB03 probes of the Galaxy have 25 fold redundancy. The confirming observations were used to reject spurious sources and combined to improve parameter estimation.

Band Merge Because the MSX Band A is much more sensitive than the other bands, by at least a factor of 10, the sources that were extracted from the different MSX spectral bands within a single DCE were merged before searching for confirming observations from overlapping scans. This is in contrast with most surveys, such as IRAS, which treated the observations in each band as an independent survey. The focal-plane arrays in MSX bands A, D, and E arrays were accurately superimposed with dichroic filters, as separately were the B and C arrays. Thus, the positional criterion for band merging on a single scan was much tighter than it would be for merging sources from independent surveys in each band. The band merge program used associated sorts to quickly localize a comparison list to the neighborhood of the selected source. The sources are sorted in order of decreasing SNR and the highest SNR source is taken as the initial seed. After it has been band merged, the source with the next highest SNR becomes the seed and so forth.

Scan Merge Following Band Merge, sources from overlapping scans are merged in a two step process. The first pass identifies all possible source matches from candidate sources in scan M to a seed source from scan N. Because the sources in the individual scans have larger errors than those in the final catalog and we do not want to miss any matches, the first pass uses less stringent matching criteria than that in the second step. The first step often produces matches with multiple candidates from scan M to a given scan N seed. The second pass uses a stricter position association criterion, which determines which of any multiple associations are most likely. Once all matches to a given seed from all possible scans have been found, we calculate the weighted mean of the flux and position and the associated uncertainties. Sources are also flagged for variability, confusion, and for goodness-of-fit to the PRF.

Pass 1 Merge Initial associations are made if the positional difference, Δr_{N-M}, between the seed from scan N and a candidate source from scan M satisfies the condition:

$$\frac{(\Delta r_{N-M}/2)^2}{\sigma_{in}^2(N)+\sigma_x^2(N)+\sigma_{in}^2(M)+\sigma_x^2(M)} < 18.4. \tag{19}$$

where σ_{in} and σ_x are the uncertainties in the in-scan and cross-scan positions. As for the Band Merge procedure, we use a descending SNR ordered list to choose the seed sources.

Pass 2 Merge The second pass identifies the most likely association by the degree of overlap of the error ellipses and, when necessary, flux information. While the global root-mean-squared (RMS) error in the updated DAF positions is $<1\overset{''}{.}8$ in both in-scan and cross-scan, the magnitude and asymmetry of the error ellipse can vary from scan to scan.

The errors for the MSX source extractions have independent in-scan and cross-scan positional variances. The global fits to the updated DAFs have normal error distributions in both directions but with somewhat different variances. Thus, the errors have a bi-normal distribution. The criterion for acceptance of a match is

$$\chi^2 = \frac{(\Delta r_{in}/2)^2}{\frac{1}{2}[\sigma_{in,N}^2+\sigma_{in,M}^2]} + \frac{(\Delta r_x/2)^2}{\frac{1}{2}[\sigma_{x,N}^2+\sigma_{x,M}^2]} < \Omega. \tag{20}$$

We set $\Omega = 18.4$, which is the 99.99% confidence level in a bi-normal distribution. For these calculations, we assume that the mean position is the "truth" for each pair of sources and that the in-scan and cross-scan directions are defined by the reduced error ellipse for the pair, as described in the section on Position Data. The pass 1 merge, which is designed to capture all possible matches, uses the RSS'd uncertainties and the total position error to define the χ^2 parameter. For pass 2, the criterion is more stringent in that we compute both the in-scan and cross-scan components of the χ^2 parameter independently using the mean position and the mean variance, as is appropriate for the bi-normal distribution. For seed sources with more than one match from scan M, we compute additional χ^2 terms based on the flux in each band, comparing the fluxes of the scan N seed to those from each scan M associated source. The scan M source that gives the lowest total χ^2 term is accepted as the true match to the seed source. Because of the pixel size and the expected scan-to-scan astrometric error, we also accept any scan M source within $15''$ of the seed source to be a match to be merged regardless of the χ^2 value, if there are no other scan M matches.

Position Data The survey and raster scan observations were executed in an in-scan and cross-scan coordinate system. For example, the "in-scan" direction for the Galactic plane long survey scans corresponds to lines of constant Galactic latitude, while the raster scans that probe deeper into the Galactic plane are along constant Galactic longitude. For the IRAS gaps, the in-scan direction is along lines of nearly constant ecliptic longitude (epoch 1983). Most of the remaining raster observations were scanned along lines of declination. A few sources (M31, LMC, and the comets) were scanned along the principal axis of the object being measured. The large majority of sources in the catalog were observed on overlapping scans and have nearly co-aligned error ellipses. This geometry breaks down near the North Ecliptic Pole and where the ecliptic scans cross through the Galactic plane scans.

In the general case, with N detections of a source, the final right ascension (RA) and declination (Dec) (α, δ) are given by

$$\alpha = \frac{\sum\limits_{i=1}^{N} w_{i,\alpha}\alpha_i}{\sum\limits_{i=1}^{N} w_{i,\alpha}}; \qquad \delta = \frac{\sum\limits_{i=1}^{N} w_{i,\delta}\delta_i}{\sum\limits_{i=1}^{N} w_{i,\delta}} \tag{21}$$

where for a given scan (i) the weights are:

$$w_\alpha = \frac{1}{(\overrightarrow{\sigma_{in}} \cdot \widehat{\alpha})^2 + (\overrightarrow{\sigma_x} \cdot \widehat{\alpha})^2} = \frac{1}{\sigma_{in}^2 \sin^2(\theta) + \sigma_x^2 \cos^2(\theta)}, \tag{22}$$

$$w_\delta = \frac{1}{(\overrightarrow{\sigma_{in}} \cdot \widehat{\delta})^2 + (\overrightarrow{\sigma_x} \cdot \widehat{\delta})^2} = \frac{1}{\sigma_{in}^2 \cos^2(\theta) + \sigma_x^2 \sin^2(\theta)}. \tag{23}$$

The angle θ, of the in-scan axis of the error ellipse at the point in question, is measured East of North.

The errors in the reported position are determined from a convolution with the 2-D error ellipse, assuming that both the in-scan and cross-scan uncertainties have Gaussian distributions. Since the errors for individual scans have a bi-normal distribution, convolving the N uncertainty distributions results in another bi-normal distribution. As an example, consider the case of two error ellipses with parameters (θ, a, b) and (θ', p, q) where a and p are the in-scan 1σ uncertainties and the uncertainty distributions are given by

$$f = A \exp\left[-\frac{y^2}{a^2} - \frac{x^2}{b^2}\right], \qquad f' = A' \exp\left[-\frac{y^2}{p^2} - \frac{x^2}{q^2}\right]. \tag{24}$$

It can be easily shown that the resulting error ellipse has the parameters (ϕ, u, v) where

$$\frac{1}{2}\tan 2\phi = \frac{\cos\theta \sin\theta(\frac{1}{a^2} - \frac{1}{b^2}) + \cos\theta' \sin\theta'(\frac{1}{p^2} - \frac{1}{q^2})}{\cos 2\theta(\frac{1}{a^2} - \frac{1}{b^2}) + \cos 2\theta'(\frac{1}{p^2} - \frac{1}{q^2})}, \tag{25}$$

$$\frac{1}{u^2} = \frac{1}{2}\left[\frac{\cos 2\theta(\frac{1}{a^2} - \frac{1}{b^2}) + \cos 2\theta'(\frac{1}{p^2} - \frac{1}{q^2})}{\cos 2\phi} + \frac{1}{a^2} + \frac{1}{b^2} + \frac{1}{p^2} + \frac{1}{q^2}\right], \tag{26}$$

and

$$\frac{1}{v^2} = \frac{1}{a^2} + \frac{1}{b^2} + \frac{1}{p^2} + \frac{1}{q^2} - \frac{1}{u^2}. \tag{27}$$

In the majority of cases where the redundant observations are from co-aligned scans, the resulting in-scan and cross-scan axes of the error ellipse correspond to the actual in-scan/cross-scan directions. For those cases where the scans are not co-aligned, the reported axes *do not* correspond to any physical quantity, but only reflect the statistical distribution of error in the measurement.

Irradiance Data The calculated irradiance for each band is the weighted mean of the measurements. Because the variance reported out of the covariance matrix of the fit tends to be very small for very high SNR sources, we have found that weighting the irradiance by the reduced χ^2 quantity yields a better value for the irradiance. The rationale for doing this is that the global precision or repeatability in the measured fluxes for high SNR sources is several percent regardless of the SNR value. We calculate the irradiance, L, for N detections in a given band, a, from:

$$L_a = \frac{\sum_{i=1}^{N} \frac{L_{a,i}}{\chi^2_{a,i}}}{\sum_{i=1}^{N} \frac{1}{\chi^2_{a,i}}}. \tag{28}$$

The uncertainty associated with this value is given by

$$\sigma_{L_a} = \sqrt{\frac{\sum_{i=1}^{N} \frac{\sigma^2_{a,i}}{\chi^2_{a,i}}}{\sum_{i=1}^{N} \frac{1}{\chi^2_{a,i}}} + \sigma^2_{cal,a} + \sigma^2_{truth,a}} \tag{29}$$

where $\sigma_{a,i}$ is the uncertainty (%) associated with the extraction method in the band a, $\sigma_{cal,a}$ and $\sigma_{truth,a}$ are the uncertainties inherent in irradiance measurements from SPIRIT III band a due to the calibration as outlined in Sections 2.4.5 and 4.1.

We also calculate the variance of the N measurements about this weighted mean. If there is only 1 measurement in a band, this quantity is set to -99.0.

In cases where a source was not detected in an MSX spectral band, we give the negative of the upper limit of the irradiance. This limit is taken to be the limiting irradiance for source detection for the most sensitive scan covering the area of the sky in question. The flux uncertainty values and measurement variance are set to -99.0 in this case.

2.4.3 Image-based Fluxes

Price et al. (2001) describe the procedures used to create the images from the MSX Celestial Backgrounds data. Image-based photometry was performed only on images that were created from multiple scans. The CB01 scans were not made into images, and no image-based photometry was performed on them, as they do not overlap and there is no signal to noise advantage in processing the observations through the routines described in this section.

The relevant plates were selected for each subcatalog, then the sources within the subcatalog are identified for each plate. More than one image may cover an area in the Galactic plane. For example, the CB02 long survey scans of the Galactic plane were combined into a single set of 1,680 $1^\circ\!.51\times1^\circ\!.51$ images in each MSX spectral band while separate images were created from the CB03, 04, and 05 observations within this region. Photometry on sources within a plate is derived from a least squares fit of the PRF centered on the position priors from the PSX results. The source photometry results in a flux, signal-to-noise ratio, and the formal error in the flux. For regions that have more than one image, the photometry with the best SNR is retained.

Duplicate sources There were a number of instances where sources have almost the same coordinates after redundant observations were merged. The positions of these sources were well within the $<10''$ window used to combine sources. Typically, such duplications occurred for sources extracted from overlapping CB02 and CB03 DCEs. The observations from the two types of DCEs were processed separately and these duplicate sources were resolved in the photometric extraction processing.

Each of the five subcatalog files was processed separately, under the assumption that sources were not duplicated in different subcatalogs. Sources in the subcatalog file and in the singleton file that overlapped the subcatalog region were combined into a single search list. The search lists were sorted by right ascension and the sources then inter-compared in order of increasing RA. From the beginning of the list, position matches within a specified search radius are found for each unmatched source in sequence. If matches are found, then the original source is labeled as a seed and the matches are labeled "duplicate" sources, and all such sources are assigned a group number. Once a source has been matched to one higher in the list, it is eliminated as a seed source.

The process is iterated with increasing search radius until the maximum window size adopted is reached. This order of iteration gives precedence to smaller angular separations over larger ones. Each seed or unassociated source is compared to matches for ungrouped sources in the larger window on subsequent passes. If matches are found, the sources are added to the group, if the original source is a seed, or a new group is formed if not.

This process generates a list of the grouped sources that contains each source in each group, an indication of the subcatalog file that contains the source, and the angular separations to the other sources in the group. This information was then used to remove any duplicate sources.

Point Response Functions Image-based photometry is derived from a least squares fit of the PRFs centered on the position priors from the PSX processing described in Sections 2.4.1 and 2.4.2. The PRFs of Mazuk and Lillo (1998) were appropriately modified to apply to each plate, or set of observationally equivalent plates such as a row of the Galactic plane set at a given Galactic latitude. The Mazuk and Lillo PRF images are smoothed with a Gaussian filter of a width that was optimal for each band (the band A width is used for bands B1 and B2), and then convolved with a box-car filter that accounts for the scan-motion smearing. Finally, the PRF images are rotated with a cubic interpolation to the position angle appropriate for the image, which was defined by the scan direction across the plate. The result is then volume normalized. How these PRFs are applied to a given image depends on the type of experiment that created an image. For example, the three appropriately conditioned cross-scan dependent PRFs are interpolated to the cross-scan position of a source in the images created from the CB03 raster scans. The $4\farcs5$ cross-scan step between each raster leg is small enough to preserve the cross-scan variations in the response functions across the arrays. All the other images combine data from scans that overlap by various amounts and average out the cross-scan variations in the PRFs. These images have 2, 4, or more scans that overlap by $\frac{1}{2}$, $\frac{1}{4}$ or less of the cross-scan dimension of a focal plane, respectively. Consequently, the three cross-scan focal-plane PRFs are averaged to derive a mean PRF for the plate.

The satellite scan distorts the PRF by stretching it in the direction of motion. The stretching is accounted for by convolving PRFs with a 1-D box function with a width equal to the distance traveled by the telescope in the direction of motion during a single 1/72-second integration.

The widths of the Gaussian smoothing function in each spectral band were empirically determined rather than simply adopting the $6''$ full width at half maximum that was used to create the images as described by Price et al. (2001). One reason for this is that the Mazuk and Lillo PRFs were derived from mirror scan observations and are not really "static" PRFs. The PRF smoothing parameters were derived from the shapes of the PRFs in the images of two CB03 raster-scanned fields that were specifically created at a finer ($2''$) grid spacing for this purpose. These images have a reasonable number of sources detected against a smooth background that sample the entire cross-scan extent of the arrays. The Band A field was derived from the CB03_35 observation centered at l=171° and b=0°. As this field did not have enough reasonably bright sources in the longer wavelength Bands for a decent PRF analysis, the CB03_32 field centered at l=33° and b=0° was used for these bands.

An ensemble of sources at various cross-scan positions was selected from each image and the irradiances determined by aperture photometry to create a flux "truth" table. The sources were also extracted from the standard images with 6″ pixel spacing. The Mazuk and Lillo PRFs were convolved with a box-car filter and rotated to match the point source profiles extracted from the CB03 image. Since the CB03s preserve the cross-scan variation in PRF, the PRFs at the top, center, and bottom of the array were interpolated to the cross-scan location of a source. The PRFs were then smoothed with a Gaussian filter, the width of which was adjusted to fit the data. The process was repeated until the median of the ratio of the fitted flux to the "truth" flux was unity. This "optimum" Gaussian filter width thus derived for each band was used for all the images. The Gaussian filter width for Band A was adopted for Bands B1 and B2.

Caveats Sources at higher Galactic latitudes and at the edges of the IRAS gaps were observed only during a single DCE; a focal-plane-position dependent PRF would be appropriate for these but is not used. The averaged PRFs applicable to the Galactic plane images were used for all images within 6° of the plane. Also, the CB04 IRAS gap plates are in a projection/coordinate system in which the center of the gap is the equator and the in-scan/cross-scan PRF orientations are used, whereas the actual scanning angle varies somewhat depending on the ecliptic longitude of the particular DCE. Finally, there are some regions in the plane that are covered by scans with different scan rates; in these cases the scan rate most applicable to the row of plates was used.

Calculation of Noise in the Images Because the extended Galactic background emission has not been removed from the plates, there is no direct way to measure the local noise empirically as was done in the automated PSX processing. Instead, we use the local value of the weight plane created for each of the images to determine the noise. The weight plane contains the number of overlapping scans that went into the local average of the flux in the image. The local noise is assumed to be proportional to the inverse root of the values in the weight plane.

Proportionality factors are derived from the b=0° Galactic plane images to scale the weight plane. PRF fitted photometry was done on the sources in these images and the local image noise was assumed to be the RMS of the perimeter pixels in the 13×13 pixel box used in the fitting procedure. The dark offset noise is calculated from the scans that cover an image. The proportionality constant is the ratio of a locally determined noise to that from the dark offsets divided by the square root of the local value of the weight. While this may not be accurate for calculating the SNR for a single source, the median of the values over the entire plate is representative. Furthermore, the plate medians converged to a constant value well away from the Galactic center and it is these regions of convergence that are used to determine the proportionality constants.

This procedure calibrates the dark noise during the middle of the mission, well before the rise in focal-plane temperatures increased the dark noise. Since a single set of temperature-independent proportionality constants were used, the SNR values will be slightly overestimated for the highest latitude images of the outer Galactic plane. These images were created from DCEs that were taken late in the mission and at higher focal-plane temperatures.

Photometry from a Single Plate The sources within a plate are selected from the position priors generated by the automated PSX process. For the plate sets that overlap at the edge, the sources are divided into two groups, one with all the sources within the boundaries of the plate, and a second that contains only sources within the plate overlap regions. Typically, there is a $0\overset{\circ}{.}05$ overlap in longitude for the successive Galactic plane images. The PSF fitted photometry is done on the larger group, while the smaller group is retained for processing the next image in order to remedy edge effects in the iterated source-removal-and-fitting procedure.

All the sources within a plate in each Band are also divided into two groups: those that overlap with one or more sources within a 13×13 pixel window and those that do not. The coordinates for an isolated source are mapped onto the plate, and a 13×13 pixel region ($78''\times78''$) centered on the source is extracted along with the corresponding weight plane. The stellar image must have no more than 10 unassigned pixel values (zero in the weight plane) and must have at least 10 positive pixels in the 13×13 pixel window or it will not fit. The size of the region approximately matches (but may be slightly smaller than) the grid on which Mazuk and Lillo characterized the calibrated PSFs. Mazuk and Lillo used a 97×97 grid of $0\overset{''}{.}86$ pixels for a total of about $83''$.

The effects of adjacent sources are mitigated by rejecting the affected data on the perimeter of the 13×13 pixel aperture. A plane is fit through the perimeter pixel values and subtracted from these pixels. Perimeter pixels with values that are too high are deleted in decreasing order of deviation until the mean of the perimeter pixels is approximately equal to, or less than, the median. Up to 25% of the perimeter pixels may be deleted.

Since the source positions are the prior values given by PSX, the free parameters in the PSF fit are a scalar background and the amplitude or photometric flux. The SNR and a formal flux error are also derived and all the parameters listed for the source. The PRF appropriate to the MSX spectral band and the image being processed is centered onto the position prior and interpolated to the 13×13 source aperture with the Gaussian filter. A linear least square fit is calculated to derive a scalar offset for the background plus the amplitude of the PRF. The least square equations for scalar background B and PRF amplitude A are:

$$\partial/\partial A \sum W_i(Star_i - [B - A * PRF_i])^2 = 0 \tag{30}$$

$$\partial/\partial B \sum W_i(Star_i - [B - A * PRF_i])^2 = 0 \tag{31}$$

where the summation is over the pixels in the 13×13 stellar image aperture. The fitting is done twice for each source. The first fit sets the weights W_i either to 1 or, for the deleted pixels, 0. This initial stellar amplitude gives an estimate for the pixel-by-pixel radiance, which is then used to calculate the Poisson noise. Combining the Poisson noise with the dark noise determined from the weight plane values gives the total noise. For the second fit, the weight values, W_i, are the inverse normalized square of the total noise values for the pixels.

Once the amplitude has been evaluated for the star, the irradiance and flux density can be determined. The PRF is volume-normalized in pixel space, so the irradiance is determined by multiplying the fit amplitude by the solid angle of the original PRF pixels ($0\overset{''}{.}86^2$). The flux density is then calculated by dividing the irradiance by the spectral bandwidth.

Overlapping Sources Overlapping sources are sorted by decreasing flux using the PSX values in the subcatalogs. The PRF appropriate to an image is scaled by the flux of the brightest source and centered on the PSX position. The result in a 13×13 pixel aperture within the image is subtracted from the image. The procedure continues until all overlapping sources have been processed and produces an image that has all overlapping sources removed. Each source is then restored to the processed image in the same order as it had been removed. After a source is restored, the single source fitting is performed. The PRF is then scaled with the new fit amplitude, and an updated value of the source is removed from the image. The list of overlapping stars is stepped through this procedure three times, with the original flux ordering. No convergence criterion is applied, but changes to the photometry are generally negligible after the first iteration.

SNR, Noise, and Uncertainties The Poisson noise is proportional to the square root of the "counts" for the detector times scaling factors used in the PSX (see the *Noise Estimation* topic under Section 2.4.1). The Poisson noise is also reduced by the square root of the local value in the weight plane. The total noise is then the local noise in the image added in quadrature with the Poisson noise and the SNR is the amplitude from the fit in radiance units divided by the total noise evaluated at the center of the source aperture.

The inverse square of the amplitude error is the sum, over the 13×13 source grid, of the square of the partial derivative of the fit function with respect to the amplitude, divided by the square of the noise:

$$1/\sigma_A^2 = \sum[(\partial fi/\partial A)^2/\sigma_i^2)]. \tag{32}$$

The partial derivative is just the PRF function itself. In practice, the PRF is regridded to the image pixels and amplitude normalized in radiance units. As the pixel noise is also expressed in terms of radiance, this is the error in the peak amplitude of the source in radiance units, which can then be scaled to in-band irradiance and thence to flux density.

2.4.4 Source Selection for the Catalog

Prior to band merge, the single scan candidate source list contains sources with SNR>2.8. For merged PSX extracted sources, we calculated a weighted SNR$_{PSX}$ which is the root mean square of the set of SNR$_{PSX,i}$ for individual scans, i, for a multiply observed source (see Eq. [37]). An SNR$_{im}$ is also calculated for the photometry extracted from each image. We used a signal-to-noise criterion to select sources for this catalog, as opposed to the N observations out of M opportunities used by the IRAS PSC and the MSX PSC V1.2. The SNR criterion, requiring an SNR$_{im}\geq$5 in at least one band, was found to be more robust against spurious sources, and was more consistent with the image-based source flux extraction, in part because we did not keep detailed track of the locations on the sky of the various holes in the scan created by such things as clusters of bad detectors. Also, we had a number of user requests for a catalog that included the regions, especially along the Galactic plane, that were scanned only once. A discussion of the SNR cutoff criterion, and its impact on catalog reliability, is given in Section 4.3.

Comparison of PSX and Image Derived Photometric Results The ratios of the extracted irradiances derived from both the PSX and image-based photometry to calibration star irradiance values are plotted in Figures 2 through 4. The flux ratios are plotted in these figures against the SNR for each measurement; the RMS SNR value (SNR$_{PSX}$) is used for the PSX photometry. The network of calibration stellar spectra used for the V2.3 photometric calibration is the same that is described in Cohen, Hammersley, and Egan (2000) but with a more stringent selection criterion applied to eliminate possible variable stars. The network derives from Cohen, Walker, and Witteborn (CWW; see Cohen et al. 1992a, Cohen et al. 1992b)

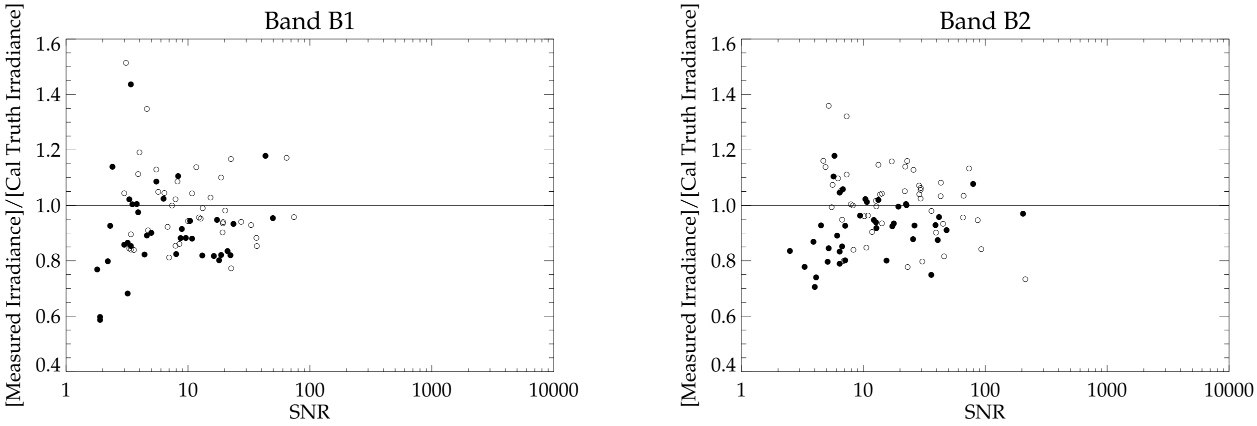

Figure 2: (left) Band B_1 initial calibration results for PSX process (filled circles) and image-based extraction (open circles). (right) Band B_2 results.

and the all-sky network (version 4) of Cohen et al. (1999), supplemented by several hundred model calibration spectra developed for the Infrared Space Observatory (ISO) program (see Cohen, Hammersley, and Egan 2000 for details). The weighted means for ratios of the stars are given in Tables 3 and 4.

A downturn or falloff below a SNR_{PSX} of 10 in the flux ratios of the PSX values is seen in the figures. This flux underestimation at low PSX fluxes is caused by the cascaded minimax-maximin filter removing some of the flux from the wings of the sources. Lower flux (SNR) sources are affected proportionally more than brighter sources, as the background error is related to the amplitude of the noise rather than to the local source flux. We confirmed this effect by running the PSX extraction routines on CB02_90 with increasingly larger window sizes for the cascaded minimax-maximin pseudo-median filter, and comparing the resulting PSX fluxes. This scan is in the outer Galaxy and was chosen to eliminate confusion, large scale crowding, and overlapping of sources. The extracted fluxes of low SNR sources asymptotically increase as

Table 3: Ratio of PSX In-band Irradiance to that Calculated for the Calibration Stars

Band	F_{PSX}/F_{Cal}	σ	$F_{\min}$ (W cm^{-2})	$F_{\max}$(W cm^{-2})	$N_{sources}$
B_1	0.926	0.105	2.99×10^{-17}	7.64×10^{-16}	33
B_2	0.930	0.106	3.29×10^{-17}	3.12×10^{-15}	40
A	0.998	0.087	2.0×10^{-18}	4.1×10^{-15}	105
C	0.991	0.006	2.8×10^{-18}	4.8×10^{-16}	55
D	0.987	0.008	1.7×10^{-18}	2.9×10^{-16}	56
E	1.069	0.025	1.3×10^{-17}	1.8×10^{-16}	15

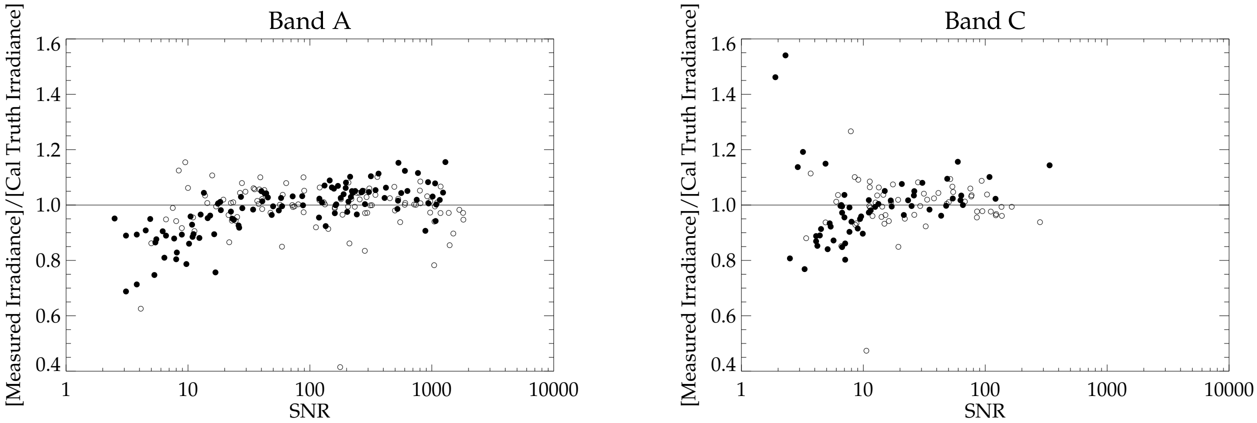

Figure 3: As for Figure 2, but for Bands A and C.

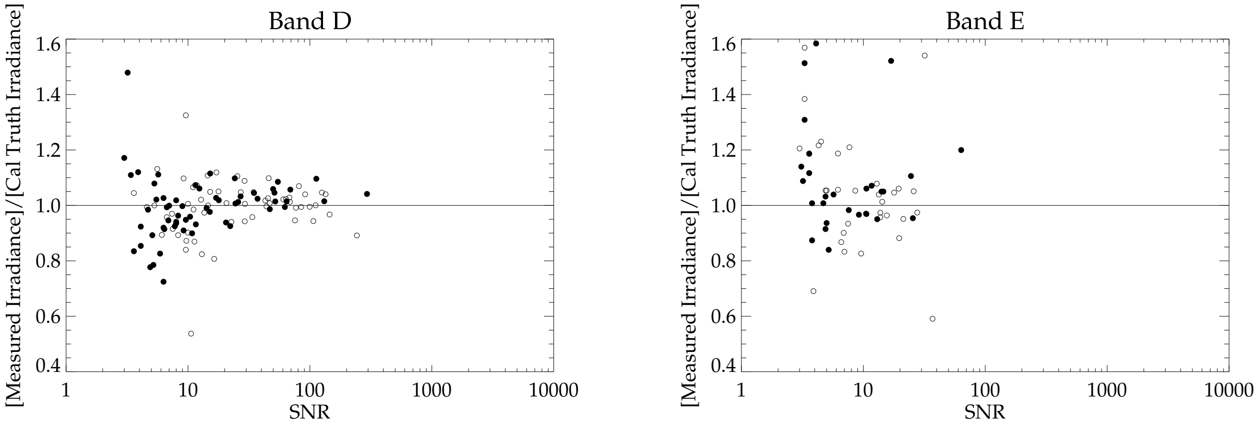

Figure 4: As for Figure 2, but for Bands D and E.

the filter width increases to a value ~20% larger than that from the window size used in the PSX. Some flux underestimation may also be seen in the image-based fluxes due to overestimation of the background. The trend in the image-based fluxes is less pronounced because of the inherently higher SNR of the image data and the 2-D background estimator. We also find that in all bands but Band A, both extraction methods overestimate the flux for a sampling of stars at low SNR (SNR<7). This is the well known statistical flux enhancement of low SNR sources found in catalogs using SNR criteria for source selection/rejection.

For bright sources (SNR>10), both flux extraction algorithms tend to yield results that are fairly consistent (within a constant bias term) with calculated values for the calibration stars. For the image-based photometry, we do note a strong flux underestimation at SNR_{im}>1000 in band A. This appears to be due to saturation effects and the reduced sampling available in the image data. For the PSX results there is evidence of a flux overestimation bias of 1.0466 for SNR_{PSX}>500 in band A. The mean calibration flux ratios for sources with the PSX and image-based fluxes with 10<SNR<1000 and $|1.0 - F_{measured}/F_{Cal}|$ <0.3 (outlier rejection) are listed in Tables 5 and 6, respectively. The biases in the ratios shown in Table 6 were used to correct the image-based fluxes listed in the PSC V2.3 Catalog, for all the sources with SNR_{im}>3 and SNR_{PSX}<500. If SNR_{PSX}>500, the quoted flux is from the PSX extraction algorithm and has been bias corrected by a factor of 1.0466 for Band A sources and 1.0 for all other bands.

Image-based photometry acceptance criteria The image-derived signal-to-noise ratio (SNR_{im}) of the photometric fit to a source was used to determine whether the image-based photometric results would be retained in the catalog or discarded in favor of the photometry calculated through the PSX process. The minimum acceptable SNR_{im} was chosen to be 3 for the initial image-fit criterion. Image-derived photometry on sources for which the PSX determined RMS signal-to-noise ratio (SNR_{PSX}) was 500 or greater was rejected in favor of the PSX photometry because the pixels in the center of such sources can have significant saturation effects. The superior oversampling of the data available in the PSX processing results in more accurate photometric fitting for these bright sources. The SNR_{im} for sources whose fluxes are not retained are still recorded in the final catalog file. In cases where multiple images exist, e.g. CB03 and CB02 images, the highest SNR_{im} is recorded.

For sources with 3<SNR_{im}<500, the image-derived flux-density is retained in the catalog. In cases where multiple image plates exist, SNR_{im} from each plate is examined and the photometry and statistics associated with the highest SNR_{im} are retained. This generally occurs for source photometry from the CB03 plates as they have a higher SNR than that obtained from the CB02 images.

Table 4: Ratio of Image-based In-band Irradiance to that Calculated for the Calibration Stars

Band	F_{im}/F_{Cal}	σ	$F_{\min}$ (W cm^{-2})	$F_{\max}$ (W cm^{-2})	$N_{sources}$
B_1	0.988	0.110	2.99×10^{-17}	7.64×10^{-16}	38
B_2	0.985	0.112	3.29×10^{-17}	3.12×10^{-15}	46
A	1.003	0.005	2.0×10^{-18}	4.1×10^{-15}	107
C	0.991	0.006	2.8×10^{-18}	4.8×10^{-16}	55
D	0.987	0.008	1.7×10^{-18}	2.9×10^{-16}	56
E	1.069	0.025	1.3×10^{-17}	1.8×10^{-16}	15

2.4.5 Calibration and Errors of V2.3 Photometry

The MSX calibration has been revised since the publication of V1.2 of the catalog. Price et al. (in preparation)

- derive responsivity corrections as a function of focal-plane temperature from the MSX stellar calibrations
- derive the in-band fluxes of the stellar standards listed in Table 2 and the absolute calibration error made by adopting α CMa as the primary standard star. These values are somewhat different than those listed in Table 2.
- validate the absolute calibration with the results from the emissive reference sphere measurements.

Calibration Accuracy The averaged ratios of the bias-corrected MSX final catalog photometry to the calibration fluxes are shown in Tables 7 and 8. Table 7 lists the results for the complete set of calibration network stars found in the PSC V2.3, which span the entire range of SNR in each band. In Table 8 we show the mean flux ratios for the calibration stars with $10<\mathrm{SNR}_{im}<1000$ and $|1.0 - F_{measured}/F_{Cal}| <0.3$. All of these ratios should equal unity after bias corrections, which is indeed the case for all bands except B_2. A source that had originally been rejected was included in the Band B_2 calculation based on the outlier rejection criterion after correcting for the bias. This changed the sample, which changed the mean ratio.

After removing the bias relative to our calibration stars, the photometric uncertainties are a combination of the precision of the measurement, systematic trends, and the bias between the measured and the absolute flux (from Table 2) for the primary standard. The estimated photometric uncertainties in each of the MSX spectral bands are give in Table 9.

Precision is a measure of how repeatable the flux is for a number of measurements on the same source under the same operating conditions. We derive the precision from the CB06 observations analyzed by Cohen et al. (2001). Each of the CB06 DCEs scanned 19–20 times across a standard star; 9 or 10 times in Bands B_1 and B_2. Cohen and Walker kindly supplied us with the images they created for each scan. We calculate the flux of a given standard star in a chosen image by fitting the data with the point response function, analogous to the image-based photometry done for the PSC. Note that Cohen et al. (2001) did aperture photometry on the data; we re-evaluated the photometry with PRF fitting to make the result compatible with the manner in which photometry was done for the catalog. We determine the mean and standard deviation of the fluxes thus derived from the 19–20 such images on a given DCE and divide the standard deviation by the mean to obtain a percent precision for that DCE. The percent deviation should

Table 5: Ratio of PSX In-band Irradiance to that of Calibration Stars where 10<SNR<1000

Band	F_{PSX}/F_{Cal}	σ	$F_{\min}$ (W cm^{-2})	$F_{\max}$ (W cm^{-2})	$N_{sources}$
B_1	0.908	0.107	1.43×10^{-16}	7.64×10^{-16}	12
B_2	0.945	0.076	1.16×10^{-16}	3.12×10^{-15}	21
A	1.010	0.066	6.32×10^{-18}	8.10×10^{-16}	81
C	1.032	0.051	2.14×10^{-17}	6.55×10^{-16}	27
D	1.020	0.054	1.30×10^{-17}	4.09×10^{-16}	29
E	1.049	0.080	3.46×10^{-17}	2.57×10^{-16}	9

Table 6: Ratio of Image-based In-band Irradiance to Calibration Stars where 10<SNR<1000

Band	F_{im}/F_{Cal}	σ	$F_{\min}$ (W cm^{-2})	$F_{\max}$ (W cm^{-2})	$N_{sources}$
B_1	0.995	0.106	4.91×10^{-17}	7.64×10^{-16}	19
B_2	0.931	0.099	7.52×10^{-17}	1.23×10^{-15}	33
A	0.957	0.052	3.36×10^{-18}	1.65×10^{-15}	83
C	0.925	0.047	8.77×10^{-18}	6.55×10^{-16}	48
D	0.950	0.065	5.86×10^{-18}	4.09×10^{-16}	43
E	0.946	0.053	1.29×10^{-17}	1.01×10^{-16}	13

Table 7: Ratio of Bias Corrected Fluxes in the V2.3 Catalog to All Calibration Network Stars

Band	$F_{PSC\_2.3}/F_{Cal}$	σ	$F_{\min}$ (W cm^{-2})	$F_{\max}$ (W cm^{-2})	$N_{sources}$
B_1	0.988	0.110	2.99×10^{-17}	7.64×10^{-16}	38
B_2	0.985	0.112	3.29×10^{-17}	3.12×10^{-15}	46
A	1.004	0.005	2.0×10^{-18}	4.1×10^{-15}	104
C	1.004	0.006	2.8×10^{-18}	4.8×10^{-16}	60
D	0.993	0.008	1.7×10^{-18}	2.9×10^{-16}	58
E	1.010	0.025	1.3×10^{-17}	1.8×10^{-16}	28

Table 8: Ratio of Bias Corrected Fluxes in Catalog to Calibration Stars with High Quality Measurements

Band	$F_{PSC\_2.3}/F_{Cal}$	σ	$F_{\min}$ (W cm^{-2})	$F_{\max}$ (W cm^{-2})	$N_{sources}$
B_1	1.000	0.110	2.99×10^{-17}	7.64×10^{-16}	19
B_2	0.988	0.112	3.29×10^{-17}	3.12×10^{-15}	34
A	1.000	0.005	2.0×10^{-18}	4.1×10^{-15}	83
C	1.000	0.006	2.8×10^{-18}	4.8×10^{-16}	48
D	1.000	0.008	1.7×10^{-18}	2.9×10^{-16}	43
E	1.000	0.025	1.3×10^{-17}	1.8×10^{-16}	13

be independent of the temperature-dependent response variations. We estimate the precision as the average of the values from high quality (SNR) standards measured on a number of DCEs.

Price et al. (in prepration) derived a global calibration against the stars in Table 2. The sum of the observations exhibited a responsivity trend with focal-plane temperature in all the bands and corrections were derived in the form of low order polynomial expressions. Unfortunately, the PSX processing and the images from which the photometry was obtained were created long before the corrections were known and cannot be easily corrected *post facto* as they combined data taken at different times and, consequently, with different focal-plane temperatures. Fortunately, the variations are small (<2%) and are included in the error term in the bias correction derived from Table 4. The final component of the absolute uncertainty is the absolute flux errors for the CWW stars used to determine the bias correction ("truth"). The uncertainties in "truth" have been estimated by Burdick and Morris (1997).

The calibration uncertainty is dominated by the precision. The value given is for one scan and the uncertainty in this quantity should decrease as square root of the number of overlapping scans that went into that portion of the image from which the photometry on the source was obtained. Alternatively, it is the square root of the number of times a source was observed that is listed in the catalog. The final flux uncertainty also must include a term (see Eq. [34]) reflecting the uncertainty in the "truth" catalog. These values for the ensemble of calibration stars are given in the final column of Table 9. The absolute accuracy is also listed in Table 1.

2.4.6 Flags

We include a number of flags as indicators of data quality that provide the user with information as to whether a source measurement might be problematic. The catalog has four flags for each band: one for the quality of the overall measurement and three flags that specify the source variability, confusion, and measurement reliability. Each flag has a value for each band a.

The overall flux quality flag, Q_a, has a value from zero to four. Table 10 lists the meaning of the flag values and the conditions under which values are assigned. SNR_{im} can take on a value of -800 if no image plate exists at the source location and -999 if the image-based PRF fitting was unable to extract a positive irradiance value. In these cases, we default to the SNR_{PSX} to set the flux quality flag. This primarily occurs in the region where three of the CB01 scans overlap, but for which no images were made.

The variability flag, V_a, reflects the variance in the individual measurements against the expected uncer-

Table 9: SPIRIT III Absolute Photometric Accuracy by Spectral Band

Band	Precision (%)	Systematics (%)	Cal Total (%)	Truth (%)	$\mathrm{RSS}_{cal,truth}$ (%)
B_1	4.62	1.0	4.73	7	8.45
B_2	5.42	0.5	5.44	7	8.87
A	2.95	0.7	3.63	2	4.14
C	4.53	0.3	4.54	2	4.96
D	5.66	1.0	5.75	2	6.09
E	3.1	2.0	4.51	4	6.03

Table 10: Flux Quality Flag Levels

Value	Meaning	Conditions
0	Not Detected	Not detected in this band in any scan
1	Limit	$\mathrm{SNR}_{im}<5.0$
2	Fair/Poor	$5.0\leq\mathrm{SNR}_{im}<7.0$; or $\mathrm{SNR}_{im}=-800$ and $5.0\leq\mathrm{SNR}_{PSX}<10.0$
3	Good	$7.0\leq\mathrm{SNR}_{im}<10.0$; or $\mathrm{SNR}_{im}=-800$ and $\mathrm{SNR}_{PSX}\geq10.0$
4	Excellent	$\mathrm{SNR}_{im}\geq10.0$

tainty of the quoted irradiance for band a. It can be either 0 or 1 under the conditions

$$\sqrt{\frac{(\sum_{j=1}^{N} L_{a,j}^2) - NL_a}{(N-1)\sigma_{L_a}^2}} \leq 3 \quad \Rightarrow \quad V_a = 0 \tag{33}$$

$$\sqrt{\frac{(\sum_{j=1}^{N} L_{a,j}^2) - NL_a}{(N-1)\sigma_{L_a}^2}} > 3 \quad \Rightarrow \quad V_a = 1.$$

The actual quantity calculated from this equation is also listed in the catalog.

The confusion flag, C_a, can also take on values of either 0 or 1. Zero denotes an unconfused source, while 1 indicates that there is a potential confusion problem. Confusion in this case means that there were two (or more) sources in the band in question in at least one scan that fell within the 99.99% confidence position ellipse, **or** there were at least two sources in a given scan and band within a radius of 1.5 detector pixels ($27''$) of the seed source.

The final flag is a measurement reliability flag, R_a, which is based on how well the source extractor was able to fit the PSF, as determined by the value of the reduced χ^2. If all detections in band a have $\chi^2<3$, R_a is set to zero. R_a is given a value of 1 if some χ^2 values are greater than three and some are less than three. It is set to 2 if all extractions in the band have $\chi^2>3$. If all extractions are poor fits to the PRF, this is generally an indication that the source is embedded in some nebulosity. It is often the case that quality 2 flags are seen in bands A and E for sources in the Galactic plane. Examination of the MSX image data shows that nebulosity is more of a problem at these wavelengths, and to a lesser degree in band C. Quality flags of 1 tend to show up for brighter sources and are likely a result of a source detection being corrupted by bad pixels. In any case, the reported positions and flux densities of sources for which $R_a>0$ are likely to have larger uncertainties than those quoted in the catalog. $R_a=9$ if the source was not detected in that band.

3 Catalog Format and Statistics

A catalog of sources with positions, band-merge fluxes, and appropriate flags was derived using the PSX described above. The catalog is comprised of eight subcatalogs or files consisting of:

- Five latitude bands in the Galactic plane :$-6\overset{\circ}{.}0$ to $-2\overset{\circ}{.}0$, $-2\overset{\circ}{.}0$ to $-0\overset{\circ}{.}5$, $-0\overset{\circ}{.}5$ to $+0\overset{\circ}{.}5$, $+0\overset{\circ}{.}5$ to $+2\overset{\circ}{.}0$, and $+2\overset{\circ}{.}0$ to $+6\overset{\circ}{.}0$. These subcatalogs contain all the CB02 Galactic Survey scans, the CB03 raster scanned observations along the plane, and the measurements from the CB04 IRAS gap survey that fell within 6° of the Galactic plane. The CB05 Structured Background experiment observations on W3 and the Rosette nebula are also included as they are within 6° of the plane.

- A single subcatalog of sources from the CB04 IRAS gap survey that were greater than 6° from the Galactic plane, sources in the LMC, and sources from the overlapping CB01 scans.

- A subcatalog of singleton sources observed only on a single scan that derived from the five non-overlapping CB01 near-Sun zodiacal background scans, scans at the edge of the Galactic plane survey, and the edges of the LMC and Areas Missed by IRAS surveys.

- A set of mini-catalogs that contain sources and photometry extracted from the raster scanned observations of galaxies and star-forming regions.

The catalog files are in ASCII format with entries as given in Table 11. The columns are space delimited (except for the variability, confusion, and measurement reliability flags, which are each given as a block), and were written out using the following FORTRAN format statement:

```
2002 format(a23,1x,f9.4,1x,f9.4,2(1x,f4.1),1x,f5.1,1x,i3,
     & 6(1x,1pe12.4,i2,1x,0pf5.1,1x,f6.1,1x,f6.1,1x,i3,1x,f5.1),1x,6i1,1x,6i1,1x,6i1)
```

The MSX catalog names of the sources have been defined according to International Astronomical Union (IAU) conventions with a unique identifier combined with the position of the source. In this case, the MSX PSC V2.3 sources are named using the convention MSX6C GLLL.llll±BB.bbbb, where MSX6C denotes that this is MSX data run using Version 6.0 of the CONVERT software, and GLLL.llll±BB.bbbb gives the Galactic coordinates of the source.

For ease of handling, the main catalog is broken into six files. The coverage of the subcatalogs is listed in the "Location" column of Table 12.

3.1 Source Statistics

Version 2.3 contains a total of 440,487 sources in the main catalogs. Of these, 431,711 are included in the Galactic plane survey (lying within $|b|<6°$), and 8,776 are in the areas missed by IRAS at latitudes higher than $|b|=6°$ or in the LMC. Given the characteristic sensitivities of the SPIRIT III infrared arrays, most ($\sim$73%) of the sources were only detected in band A. The breakdown of sources with non-limit detections ($Q_a \geq 2$) in each band is given in Table 12.

3.2 Flag Statistics

3.2.1 Flux Quality

The flux quality flag, Q_a, should, generally, be used to decide the trustworthiness of a quoted flux density. Table 13 details the number of sources in each quality category for each SPIRIT III radiometric band. The statistics are also given by subcatalog region. To be included in the catalog, there must be at least one band for which $Q_a \geq 2$.

Table 11: Format of MSX Point Source Catalog Files

Column	Format	Field	Units
	a23	Name	
25	f9.4	Right Ascension	J2000 decimal degrees
35	f9.4	Declination	J2000 decimal degrees
45	f4.1	in-scan uncertainty (1σ)	arcseconds
50	f4.1	cross-scan uncertainty (1σ)	arcseconds
55	f5.1	scan angle	degrees E of N
61	i3	total number of sightings	
65	e12.4	Band B_1 flux density	Jy
77	i2	Band B_1 flux quality flag	
80	f5.1	Band B_1 flux uncertainty (1σ)	%
86	f6.1	Image extraction SNR value, Band B_1 detections	
93	f6.1	RMS automated extraction SNR value, Band B_1 detections	
100	i3	number of Band B_1 detections	
104	f5.1	variation of Band B_1 measurements	
110	e12.4	Band B_2 flux density	Jy
122	i2	Band B_2 flux quality flag	
125	f5.1	Band B_2 flux uncertainty (1σ)	%
131	f6.1	Image extraction SNR value, Band B_2 detections	
138	f6.1	RMS automated extraction SNR value, Band B_2 detections	
145	i3	number of Band B_2 detections	
149	f5.1	variation of Band B_2 measurements	
155	e12.4	Band A flux density	Jy
167	i2	Band A flux quality flag	
170	f5.1	Band A flux uncertainty (1σ)	%
176	f6.1	Image extraction SNR value, Band A detections	
183	f6.1	RMS automated extraction SNR value, Band A detections	
190	i3	number of Band A detections	
194	f5.1	variation of Band A measurements	
200	e12.4	Band C flux density	Jy
212	i2	Band C flux quality flag	
215	f5.1	Band C flux uncertainty (1σ)	%
221	f6.1	Image extraction SNR value, Band C detections	
228	f6.1	RMS automated extraction SNR value, Band C detections	
235	i3	number of Band C detections	
239	f5.1	variation of Band C measurements	
245	e12.4	Band D flux density	Jy
257	i2	Band D flux quality flag	
260	f5.1	Band D flux uncertainty (1σ)	%
266	f6.1	Image extraction SNR value, Band D detections	
273	f6.1	RMS automated extraction SNR value, Band D detections	
280	i3	number of Band D detections	
284	f5.1	variation of Band D measurements	
290	e12.4	Band E flux density	Jy

Table 11: Format (cont.)

Column	Format	Field	Units
302	i2	Band E flux quality flag	
305	f5.1	Band E flux uncertainty (1σ)	%
311	f6.1	Image extraction SNR value, Band E detections	
318	f6.1	RMS automated extraction SNR value, Band E detections	
325	i3	number of Band E detections	
329	f5.1	variation of Band E measurements	
335	i1	Band B_1 variability flag	
336	i1	Band B_2 variability flag	
337	i1	Band A variability flag	
338	i1	Band C variability flag	
339	i1	Band D variability flag	
340	i1	Band E variability flag	
342	i1	Band B_1 confusion flag	
343	i1	Band B_2 confusion flag	
344	i1	Band A confusion flag	
345	i1	Band C confusion flag	
346	i1	Band D confusion flag	
347	i1	Band E confusion flag	
349	i1	Band B_1 measurement reliability flag	
350	i1	Band B_2 measurement reliability flag	
351	i1	Band A measurement reliability flag	
352	i1	Band C measurement reliability flag	
353	i1	Band D measurement reliability flag	
354	i1	Band E measurement reliability flag	

3.2.2 Variability

A variability flag of V_a=1 denotes that the variation of the measurements over the MSX SPIRIT III mission is greater than $3\sigma_a$. Table 14 lists the number of sources in each band for each subcatalog that exhibited variability over the mission lifetime that are not likely to be due to statistical error in the measurements.

3.2.3 Confusion

Table 15 reports the number of confused sources in each band in each subcatalog. As expected, confusion is an increasing problem toward the Galactic equator. The lowest confusion density is away from the plane, in the IRAS gaps.

3.2.4 Measurement Reliability

Table 16 lists the measurement reliability flag statistics for the entire PSC V2.3 for each SPIRIT III spectral band. In this case, a value of R_a=9 means that the source was not detected in band a. Most of the detected sources in each band fall in the R_a=0 category, which means that they fit the point source function well.

Table 12: Source Count Numbers by Band and Location

Location	B_1	B_2	A	C	D	E
$\|b\| > 6°$	111	195	8600	693	698	372
$2° < b \leq 6°$	182	355	68725	5847	5653	2013
$0.°5 < b \leq 2°$	286	594	86342	10607	10321	3991
$-0.°5 < b \leq 0.°5$	436	951	106453	19911	19481	10063
$-2° < b \leq -0.°5$	269	790	91799	12204	11855	4908
$-6° < b \leq -2°$	211	521	76898	6931	6679	2235
Total	1495	3406	438817	56193	54687	23582

Table 13: Statistics of Flux Quality Flags

		B_1	B_2	A	C	D	E
$Q = 0$	$\|b\| > 6°$	8141	8231	118	7152	7236	7941
	$2° < b \leq 6°$	66131	67099	8	54733	56547	63646
	$0.°5 < b \leq 2°$	81809	83872	103	63540	65424	76841
	$-0.°5 < b \leq 0.°5$	100284	103381	499	68625	72743	88263
	$-2° < b \leq -0.°5$	87663	88814	166	66140	69036	81327
	$-6° < b \leq -2°$	73783	74624	4	61053	62474	71154
$Q = 1$	$\|b\| > 6°$	524	350	58	931	842	463
	$2° < b \leq 6°$	2468	1327	48	8201	6581	3122
	$0.°5 < b \leq 2°$	4484	2113	134	12432	10834	5747
	$-0.°5 < b \leq 0.°5$	6589	2977	357	18773	15085	8983
	$-2° < b \leq -0.°5$	4184	2512	151	13772	11225	5881
	$-6° < b \leq -2°$	2932	1781	24	8942	7773	3537
$Q = 2$	$\|b\| > 6°$	50	68	1775	206	192	98
	$2° < b \leq 6°$	75	132	18447	1708	1601	589
	$0.°5 < b \leq 2°$	128	268	18239	3191	3000	1114
	$-0.°5 < b \leq 0.°5$	186	402	15087	5466	4942	2303
	$-2° < b \leq -0.°5$	98	325	18475	3508	3246	1316
	$-6° < b \leq -2°$	78	182	18362	1963	1942	656
$Q = 3$	$\|b\| > 6°$	17	38	1983	155	187	151
	$2° < b \leq 6°$	36	85	15515	1261	1239	472
	$0.°5 < b \leq 2°$	63	133	18147	2352	2237	879
	$-0.°5 < b \leq 0.°5$	104	227	19875	4393	3997	1890
	$-2° < b \leq -0.°5$	64	187	19272	2745	2605	999
	$-6° < b \leq -2°$	62	139	17513	1578	1458	543
$Q = 4$	$\|b\| > 6°$	44	89	4842	335	319	123
	$2° < b \leq 6°$	71	138	34763	2878	2813	952
	$0.°5 < b \leq 2°$	95	193	49956	5064	5084	1998
	$-0.°5 < b \leq 0.°5$	146	322	71491	10052	10542	5870
	$-2° < b \leq -0.°5$	107	278	54052	5951	6004	2593
	$-6° < b \leq -2°$	71	200	41023	3390	3279	1036

Table 14: Statistics of Variability Flags

		B_1	B_2	A	C	D	E
$V = 1$	$\|b\| > 6^\circ$	0	0	1260	134	82	20
	$2^\circ < b \leq 6^\circ$	0	0	7975	1152	744	159
	$0\overset{\circ}{.}5 < b \leq 2^\circ$	0	0	11131	2073	1456	269
	$-0\overset{\circ}{.}5 < b \leq 0\overset{\circ}{.}5$	0	0	15499	4188	3188	699
	$-2^\circ < b \leq -0\overset{\circ}{.}5$	0	0	13249	2831	2053	437
	$-6^\circ < b \leq -2^\circ$	0	0	8905	1197	815	140

Table 15: Statistics of Confusion Flags

		B_1	B_2	A	C	D	E
$C = 1$	$\|b\| > 6^\circ$	8	2	483	18	16	28
	$2^\circ < b \leq 6^\circ$	21	13	1880	140	87	55
	$0\overset{\circ}{.}5 < b \leq 2^\circ$	49	19	3528	296	229	218
	$-0\overset{\circ}{.}5 < b \leq 0\overset{\circ}{.}5$	148	39	8922	1095	967	1104
	$-2^\circ < b \leq -0\overset{\circ}{.}5$	48	11	4357	486	368	367
	$-6^\circ < b \leq -2^\circ$	25	14	2368	127	123	67

Table 16: Statistics of Measurement Reliability Flags

	B_1	B_2	A	C	D	E
$R = 0$	22656	14236	430188	117482	104872	48126
$R = 1$	1	3	6324	290	508	1175
$R = 2$	3	6	3073	333	705	1579
$R = 9$	417827	426242	902	322382	334402	389607

4 Analysis of the Content of the MSX Point Source Catalog Version 2.3

4.1 Photometric Accuracy

In contrast to V1.2 of the PSC, which relied on the CONVERT based radiance calibration, we calculated and applied calibration corrections to the flux density measurements extracted for V2.3. Accurate point-spread functions (PSFs) derived from on-orbit measurements for three positions across the focal plane in each band were used in the PSX to produce more accurate irradiance measurements from the single scan data. The PSFs used for the image-based photometry were either interpolated for the CB03 scans or averaged superpositions of the true PSF for the other images, then weighted by the smoothing functions as described in Section 2.4.4.

The quoted flux error (as a percentage of the source flux) has been computed for each measurement as the root-sum-squared (RSS) of the formal extraction (PSF fitting) error and the instrument calibration uncertainty (discussed in Section 2.4.5 and listed in Table 9). Expressed mathematically, the flux uncertainty for a given band, a, is

$$\sigma_{flux,a} = \sqrt{\sigma^2_{fit,a} + \sigma^2_{cal,a} + \sigma^2_{truth,a}}. \tag{34}$$

For a large enough sample of stars with truth measurements, the standard deviation of this ensemble should approach the uncertainty we expect based on repeated measurements of the same star (precision), as long as $\sigma_{fit,a}$ in Equation (34) is negligible. We computed the standard deviation and the mean absolute deviation (MAD) of the distribution for the high quality measurement sample of calibration network stars in PSC V2.3 with $10<\mathrm{SNR}_{PSX,a}<1000$, which have relatively negligible $\sigma_{fit,a}$. The results for each band are given in Table 17, along with the number of sources in each sample and the absolute calibration error from Table 9. For Bands B_1, A, C, and D, the absolute calibration uncertainty lies between the two deviations in the source distribution. For Band B_2, both the standard and mean absolute deviations are larger than expected from the calibration uncertainty, while for Band E, the distribution is narrower than expected in both measures.

The quoted 1σ flux uncertainty distributions for each band for flux qualities $Q_a\geq2$ are shown in Figures 5 through 7. The high flux quality sources Q_a=4 are plotted in green, the moderate flux quality, Q_a=3, in blue, and the fair flux quality Q_a=2 in red. As expected, the highest flux qualities have the smallest flux uncertainties, while the low flux quality sources have the highest uncertainties, due to larger fitting errors.

Table 17: Measured Flux Error by Spectral Band

Band	σ_{CWW} (%)	MAD_{CWW} (%)	N_{CWW}	$\mathrm{RSS}_{cal,truth}$
B_1	10.43	8.09	20	8.45
B_2	11.23	9.02	35	8.87
A	5.48	3.92	83	4.14
C	5.07	4.09	49	4.96
D	6.87	4.99	43	6.09
E	5.40	4.44	14	6.03

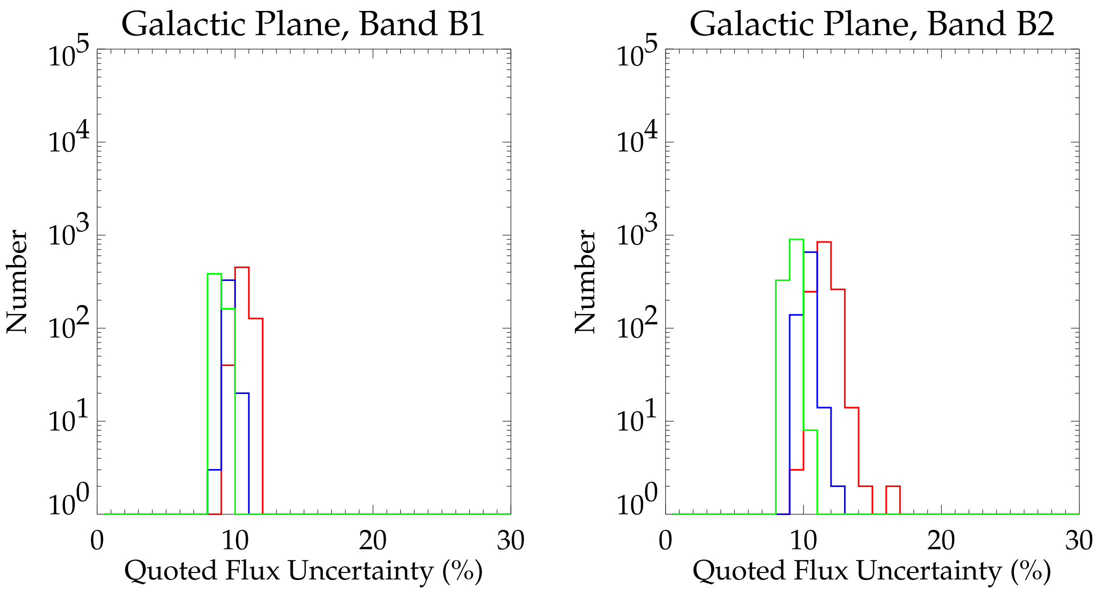

Figure 5: Quoted 1σ flux uncertainties for Bands B_1 and B_2.

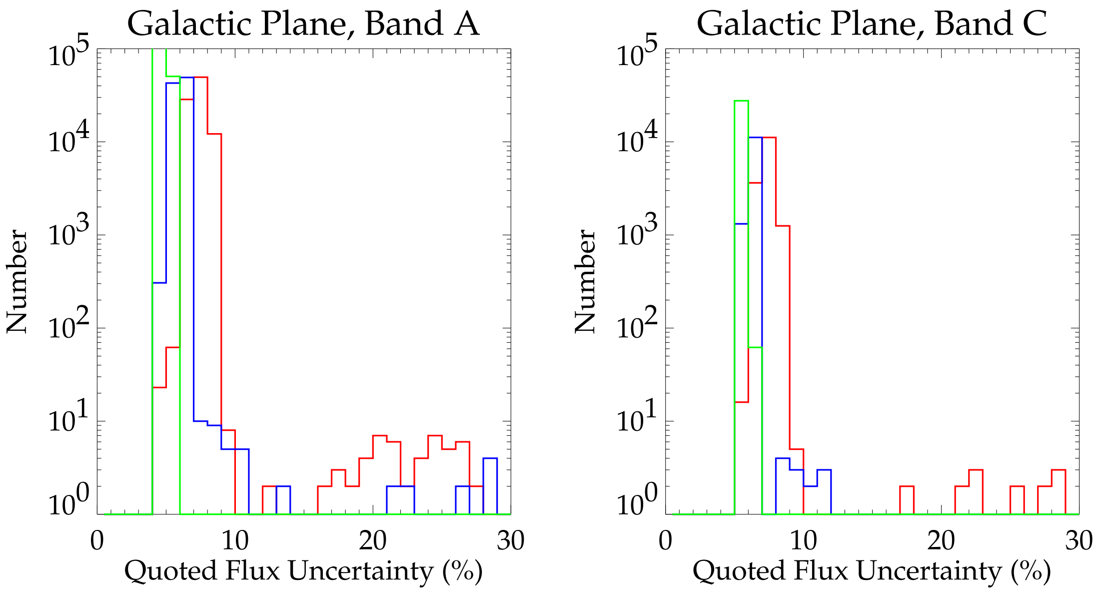

Figure 6: Quoted 1σ flux uncertainties for Bands A and C.

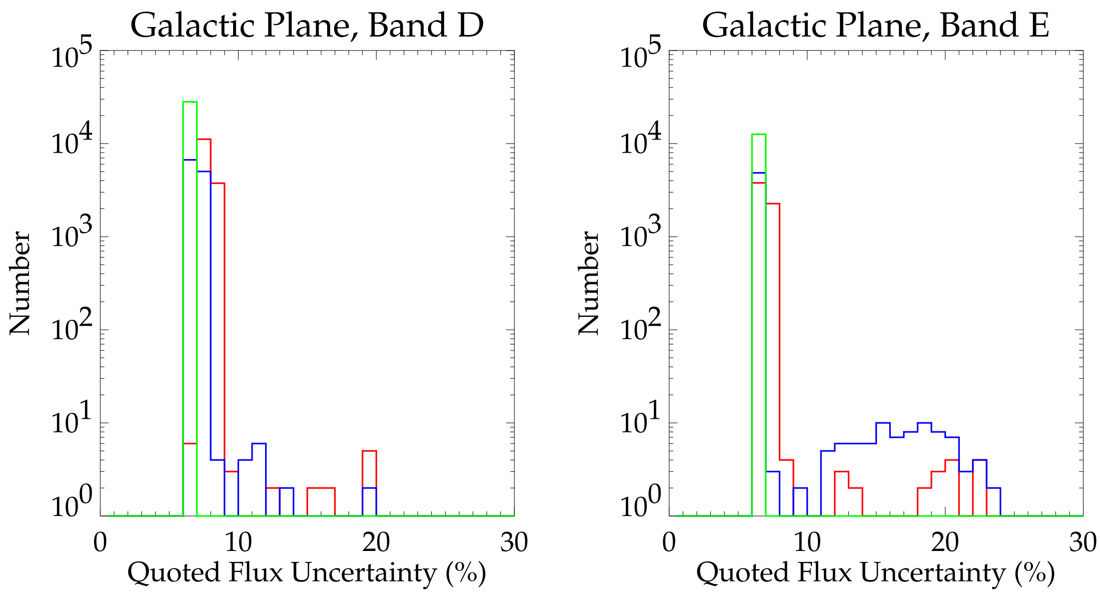

Figure 7: Quoted 1σ flux uncertainties for Bands D and E.

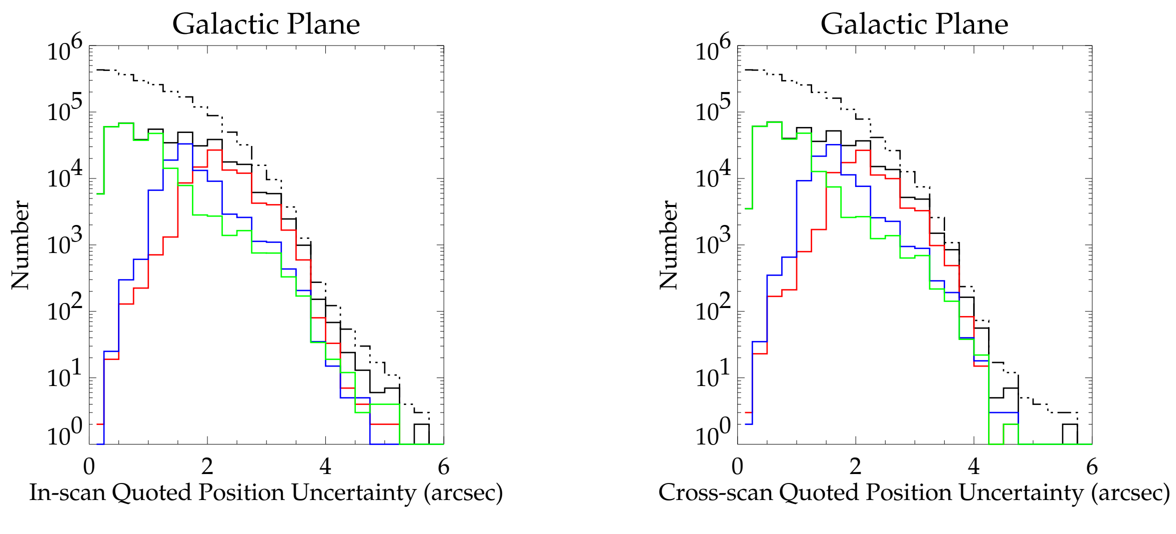

Figure 8: Quoted 1σ in-scan (left) and cross-scan (right) position uncertainties of the Galactic plane catalog sources.

4.2 Astrometric Accuracy

The in-scan and cross-scan positional uncertainties listed in the catalog are determined by the formulas in Section 2.4.2. If the error ellipses from confirming scans were aligned, we simply took the RSS of the uncertainties inherent in the point source extraction procedure and the uncertainty in the spacecraft attitude determination. Mathematically, the in-scan or cross-scan uncertainty of a single scan is given by

$$\sigma = \sqrt{\sigma_{pos}^2 + \sigma_{DAF}^2}. \tag{35}$$

For a given scan, Price et al. (2001) demonstrated that the revised definitive attitude files (DAF) have in-scan and cross-scan global uncertainties (σ_{DAF}) on the order of $1\farcs5$ in each dimension. The source extraction procedure is able to fix the position of the PSF (σ_{pos}) in focal-plane coordinates within about 0.1 pixel, or $\sim1\farcs8$ for both in-scan and cross-scan. This yields a typical error ellipse semi-major axis of $\sim2\farcs34$. For those areas of the sky for which we have quadruply redundant scans, we expect to gain a factor of two improvement in the positional uncertainty. This translates to an expected typical uncertainty in the catalog of $\sim1''$ in each direction. In the following sections we examine the statistics of the quoted positional uncertainties for the Galactic plane and the IRAS gap catalogs, and estimate the true positional accuracy by comparing the positions of catalog stars to those from the Tycho-2 astrometric catalog.

4.2.1 The Galactic Plane

Quoted Uncertainties - The quoted in-scan and cross-scan 1σ positional uncertainties are shown in Figures 8. The solid black lines are the number of stars per bin, while the dashed black lines shows the cumulative distribution of position uncertainties for all Galactic plane catalog sources. The colored differential histograms show the distribution of the position uncertainties for the 430,217 sources with band A flux qualities of $Q_A \geq 2$. These have been further broken down by Q_A with green denoting $Q_A=4$, red $Q_A=3$, and blue $Q_A=2$. Because the flux quality flag is based on the SNR of the source, the higher quality flux measurements also have less uncertainty in their positions. The mean values of each of these distributions can be found in Table 18.

Measured Position Accuracy - The quoted position uncertainties are derived from statistical errors associated with the point source extraction and the uncertainties inherent in the DAF. These numbers should accurately reflect the trustworthiness of the quoted position. To test our results, we cross-referenced the MSX PSC V2.3 to the Tycho-2 catalog (Høg et al. 2000). In order to avoid incorrect matching of IR stars with nearby Tycho visible stars, we required that positionally matched Tycho/MSX pairs also pass color criteria (Wright, Egan, and Price 2002; Wright, Egan, and Price in prep.). We defined

$$\chi^2 = \left[\frac{\Delta r_{in}^2/2}{\sqrt{(\sigma_{in\_Tycho}^2 + \sigma_{in\_MSX}^2)/2}}\right]^2 + \left[\frac{\Delta r_{x}^2/2}{\sqrt{(\sigma_{x\_Tycho}^2 + \sigma_{x\_MSX}^2)/2}}\right]^2 \tag{36}$$

where σ_{in} and σ_x are the 1-sigma in-scan and cross-scan errors, respectively, from the given catalog, and Δr_{in} and Δr_x are the in-scan and cross-scan components of the separation distance. Matches were found for 30,745 stars with $\chi^2<18.5$ and a (V_T – [A]) color within 3σ of the value expected based on the spectral type or the (B_T – V_T) color (Wright et al. 2003). The results are shown in Figure 9, where the in-scan distribution of error (truth position − MSX PSC position) is shown in black, and the cross-scan distribution in red. We fit a Gaussian model to each distribution and include the results in Table 18.

The in-scan and cross-scan error distributions are very similar, and both show the same non-Gaussian wings. The wings are due to the fact that the distribution in either direction is essentially the sum of two Gaussians: a relatively broad distribution corresponding to the $Q_A = 2$ objects, and a much narrower distribution corresponding to objects with higher flux qualities, $Q_A \geq 3$. This is consistent with Figure 8, and it is verified in Figure 10, which shows the $Q_A = 2$ and $Q_A \geq 3$ distributions for the in-scan (black) and cross-scan (red) positional differences. In both directions, the Gaussian fit to the $Q_A = 2$ distribution has a width of $(Q_A = 2) \sim 1''\!.8$, while the Gaussian fit to the $Q_A \geq 3$ distribution in each direction has a width of $(Q_A \geq 3) \sim 0''\!.8$.

The distributions of position differences are very close to Gaussian when separated by flux quality flag. The mean quoted uncertainties tend to be larger than the actual errors derived in this analysis, which suggests that the quoted positional uncertainties are slightly overestimated. This is consistent with Figure 11, in which we show the cumulative χ^2 distribution for the MSX/Tycho-2 matches as a solid line, and the expected distribution for a two-dimensional Gaussian as a dashed line. We see that there is a moderate excess of objects with small values of χ^2, which is what we would expect to see if the quoted uncertainties are somewhat overestimated.

4.2.2 The $|b| > 6°$ Catalog

We also independently examined the positional accuracies of the stars in the high latitude catalog to explore the possibility that the difference in scan pattern with respect to the Galactic plane might have introduced a different behavior to the in-scan and cross-scan error. We find that both the measured errors and quoted uncertainties in the IRAS gaps and LMC are somewhat larger than those found in the Galactic plane.

Quoted Uncertainties - The quoted 1σ uncertainty in in-scan and cross-scan position is shown in Figure 12. The black line shows the distribution of uncertainties for the 8,600 sources with $Q_A \geq 2$. As in the Galactic plane figures, green denotes $Q_A = 4$, red denotes $Q_A = 3$, and blue denotes $Q_A = 2$. The mean values of each of these distributions are listed in Table 18.

Measured Position Accuracy - Cross referencing of the MSX PSC to the Tycho-2 catalog using the matching and confirmation criteria described above produces 6,141 matches in the high latitude CB04, CB01, and LMC data. This means that ~71% of the sources catalogued with Galactic latitude $|b| > 6°$ are matched to a Tycho-2 star. Histograms of the in-scan and cross-scan positional differences were computed and the results are shown in Figure 13. A Gaussian model fit was made to each distribution and the resulting width parameter for each model is listed in Table 18. The σ values of the Gaussian fits are quite similar to the mean measured uncertainties in the in-scan and cross-scan direction but the in-scan error is somewhat larger than the cross-scan error. As with the Galactic plane, the mean quoted uncertainties tend to be larger than those actually measured and the effect is more pronounced than in the Galactic Plane. This shows up in Figure 14 as a significant excess of objects with small values of χ^2 in the cumulative χ^2 distribution for the MSX/Tycho-2 matches plotted against the expected distribution.

The histograms may be represented by a combination of two Gaussian distributions: a relatively broad distribution corresponding to stars with $Q_A = 2$ and a narrower distribution corresponding to stars with $Q_A \geq 3$, just as in the Galactic plane. The Gaussian fit to the $Q_A = 2$ distribution has a width of $(Q_A = 2)$ $\sim 1''\!.6$ in the in-scan direction, and $(Q_A = 2) \sim 1''\!.8$ in the cross-scan direction, while the Gaussian fit to the $Q_A \geq 3$ distribution has a width of $(Q_A \geq 3) \sim 1''\!.1$ in the in-scan direction, and $(Q_A \geq 3) \sim 1''\!.0$ in the cross-scan direction.

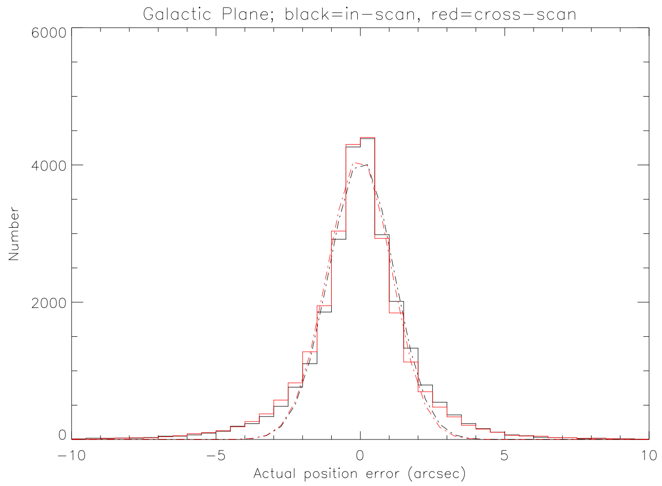

Figure 9: Comparison of the difference between the position of sources in the MSX PSC V2.3 and Tycho-2. The in-scan histogram of the differences are in black and cross-scan in red. The dashed lines are Gaussian fits to the histograms.

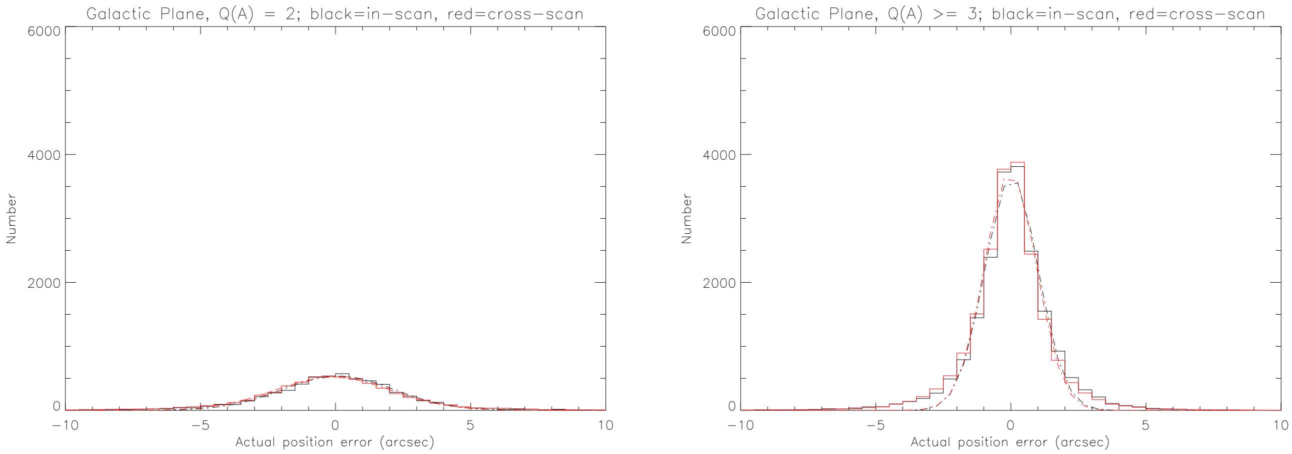

Figure 10: Position error (truth-measured) distribution of Galactic plane sources with (left) Q_A=2 and (right) $Q_A \geq 3$.

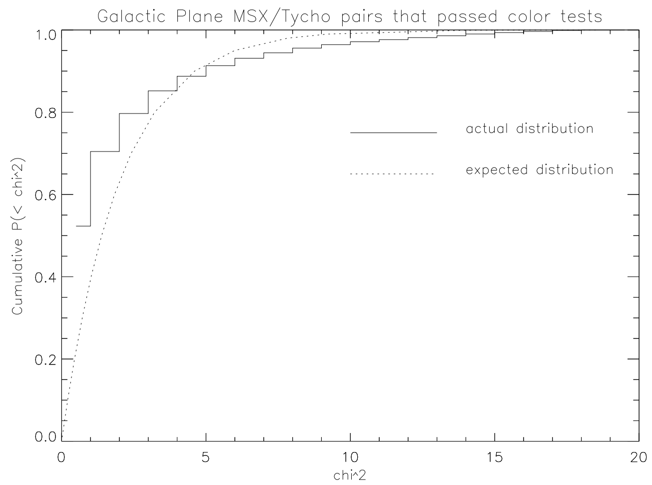

Figure 11: Distribution of the χ^2 statistics for the PSC V2.3 matches to the Tycho 2 catalog in the Galactic plane.

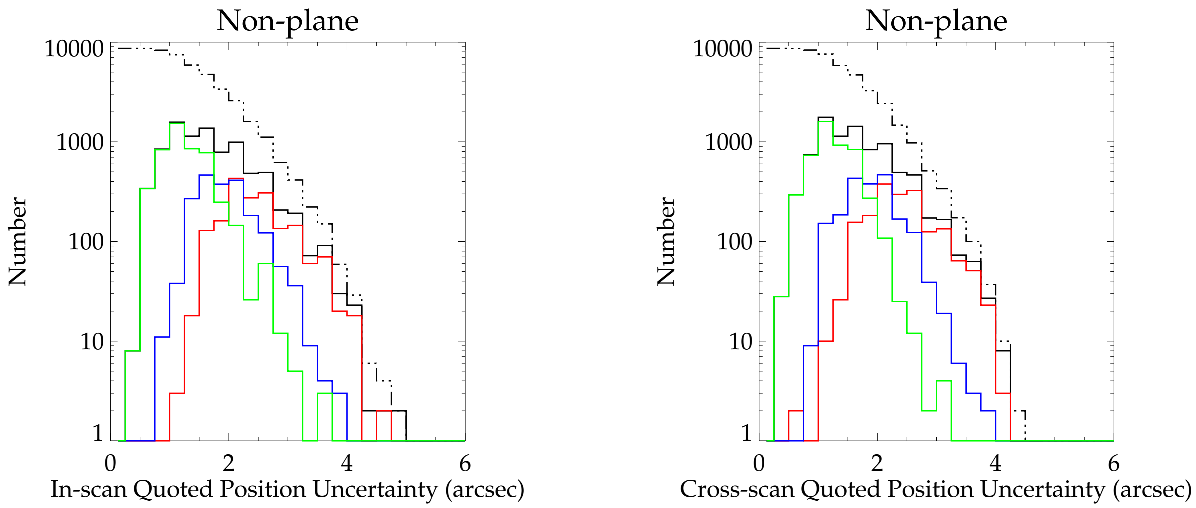

Figure 12: Quoted 1σ in-scan (left) and cross-scan (right) position uncertainties of the high latitude catalog sources.

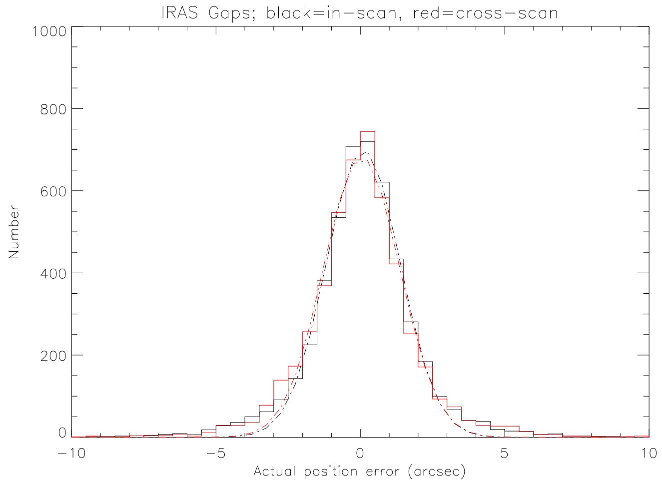

Figure 13: Histograms of the positional difference between MSX PSC V2.3 high latitude sources and Tycho-2 catalog positions. The in-scan histogram of the positional differences are in black and the cross-scan values in red. The dashed lines are gaussian fits to the histograms.

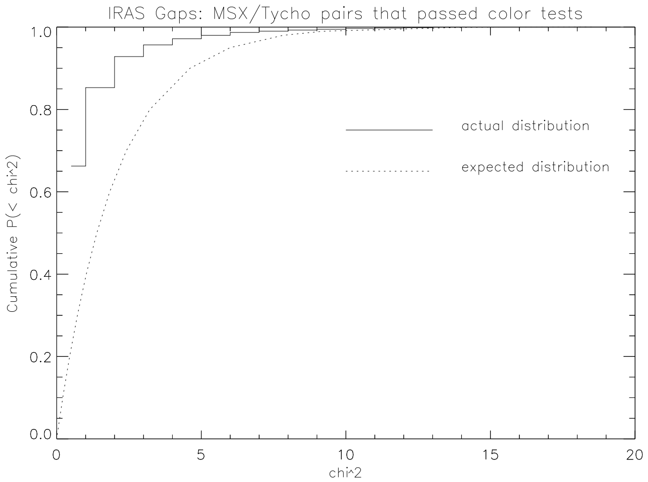

Figure 14: Distribution of the χ^2 statistics for PSC V2.3 matches to the Tycho 2 catalog for the sources in the high latitude catalog.

Table 18: MSX PSC V2.3 Positional Uncertainties

	σ_{FIT}	$\langle\sigma_{\mathrm{quoted}}\rangle$ $(Q_A \geq 2)$	$(Q_A = 4)$	$(Q_A = 3)$	$(Q_A = 2)$
Galactic Plane in-scan	$1''.12$	$1''.28$	$0''.81$	$1''.69$	$2''.21$
Galactic Plane cross-scan	$1''.11$	$1''.25$	$0''.80$	$1''.64$	$2''.13$
$\lvert b\rvert>6$ in-scan	$1''.28$	$1''.64$	$1''.24$	$1''.90$	$2''.44$
$\lvert b\rvert>6$ cross-scan	$1''.32$	$1''.62$	$1''.23$	$1''.88$	$2''.38$

4.3 Reliability

To increase the reliability of PSC V2.3 over that in V1.2, we changed the source acceptance and flux quality criteria from the N out of M type selection criteria used in V1.2 (and the IRAS PSC) to a signal-to-noise based cut-off. The overly generous N measurements out of M opportunities criterion used for V1.2 produces too many spurious sources in regions where there were more than the nominal number of MSX scans in the sky adopted for the value of M, such as where the IRAS gap scans crossed the Galactic plane or near the ecliptic poles. For example, a value of M=6 was adopted for the IRAS gaps as this was the number of overlapping scans at the ecliptic plane: M could be larger at higher ecliptic latitudes. This problem in V1.2 was acknowledged in Section 8.1.3 of the V1.2 Explanatory Guide (Egan et al. 1999) but was not properly addressed. This problem was also been noted by Lumsden et al. (2002).

We used a SNR cut-off criterion for V2.3 of the PSC and argue in the following sub-sections that our choice results in a catalog that is both reliable **and** complete to the lowest possible level. The flux quality flags also reflect limits that correspond to a certain level of reliability in the catalog, based on the tests outlined below.

4.3.1 Root-mean-square SNR from PSX Automated Extraction

We calculated the RMS average SNR for the automated PSX results as:

$$\mathrm{SNR}_{PSX} = \sqrt{\frac{\sum_{i=1}^{N} \mathrm{SNR}^2_{PSX,i}}{N}} \tag{37}$$

where there are N PSX measurements, each with an associated signal to noise ratio, $\mathrm{SNR}_{PSX,i}$ for scan i. The relationship between SNR_{PSX} and the signal-to-noise ratio expected from the image-based extraction, SNR_{im} can be illustrated as follows. Assume that there are four scans of a region, each with identical values of noise and that the PSX produces four measurements with the same SNR. In this case, $N = 4$, $\mathrm{SNR}_{PSX,i}$=SNR, and

$$\mathrm{SNR}_{PSC} = \sqrt{\frac{\sum_{i=1}^{N} \mathrm{SNR}^2_{PSX,i}}{N}} = \sqrt{\frac{4\mathrm{SNR}^2_{PSX,i}}{4}} = \mathrm{SNR}. \tag{38}$$

The image at the position of the source was created by coadding the data from the four scans. Consequently, we expect the noise level to be reduced by a factor of two ($\sqrt{N}$) in the image-based extraction, and the

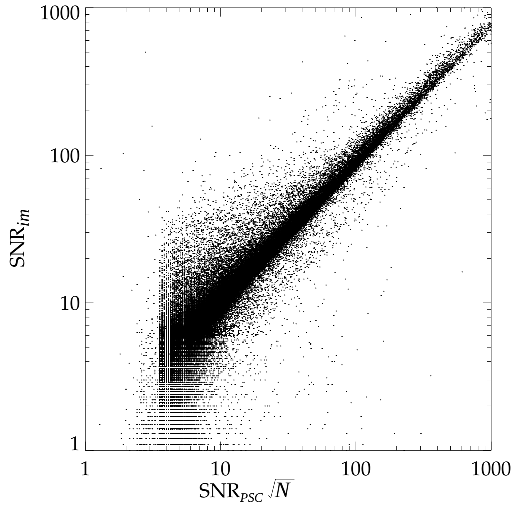

Figure 15: SNR from the image-based photometry compared to weighted PSX SNR for candidate source data in the region $-2<l<-0.5$.

signal-to-noise ratio for this source to be increased by the same amount, so

$$\mathrm{SNR}_{im} = \sqrt{N}\mathrm{SNR}. \tag{39}$$

Thus, in general, we expect that

$$\mathrm{SNR}_{im} = \sqrt{N}\mathrm{SNR}_{PSX} \tag{40}$$

for sources in PSC V2.3. Figure 15 shows that this is, indeed, a good approximation.

4.3.2 The Large Magellanic Cloud as a Test of Reliability

The sources extracted from the DCEs covering the LMC were used to ascertain the reliability of extractions as a function of the signal to noise in an image prior to compilation of the PSC V2.3. The PSX extracted sources and fluxes from the individual LMC scan legs that had an $\mathrm{SNR}_{PSX,i} > 2.7$ for an individual MSX Band A observation. Generally, the LMC was surveyed with four-fold redundancy. Sources from the individual scans were merged and the RMS SNR_{PSX} for the redundant measurements were calculated as described above. Twenty-five $2° \times 2°$ images with $6''$ grid spacing were created that cover the entire LMC area surveyed in a manner similar to that described by Price et al. (2001). About 1,500 of the candidate point sources were visually examined on the co-added images and a notation was made as to whether or not a point source could be detected by visual inspection at each source position. Grayscale images and 3-D surface plots of a $120''\times120''$ window centered on the coordinates of each source were examined for a PSF-like structure. Extended sources were accepted as "real" sources. The SNR of each real source in the image should be about a factor of $\sqrt{N}$ greater than the weighted mean flux from the single scan PSX extraction.

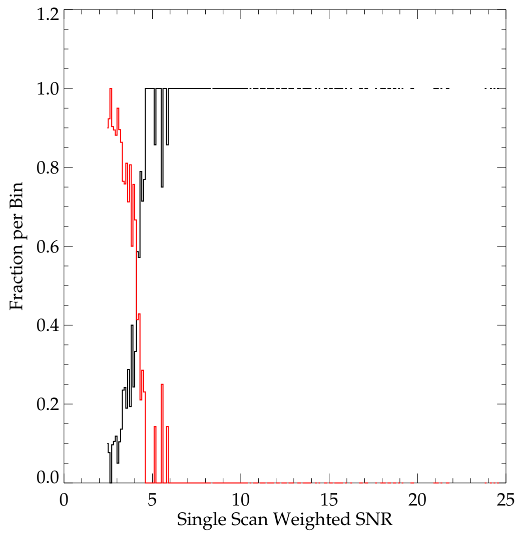

Figure 16: Cumulative distribution of the 1,500 LMC source candidates as a function of weighted SNR. Black histogram shows fraction with visible source on co-added image plate, red histogram are candidates not detectable on co-added image.

The results of this analysis are shown in Figure 16. The black cumulative distribution shows the fraction of sources in each SNR bin that were deemed to be real in the images. The red distribution quantifies the sources that were not seen in the co-added image data and, therefore, were judged likely to be spurious detections in the single scan, traceable to noise spikes. The plot shows that extractions with $\mathrm{SNR}_{PSX}>4.5$ in the LMC data have very high reliability, approaching 100%, while for $\mathrm{SNR}_{PSX}<4$ a given source is less than 50% likely to be real.

4.3.3 Source Reliability and Relation to Flux Quality Flags

We used the expected reliability based on the LMC analysis to set the flux quality flags by tying them to the expected reliability limits for the catalog. We examined the candidate point sources in the Galactic latitude range $-2<b\leq-0.5$. We extrapolated the expected reliability for a single scan RMS SNR to the image-based photometric SNR. We expect sources with an $\mathrm{SNR}_{im}>4.5$ to be highly reliable. This criterion requires single PSX measurements of sources to have $\mathrm{SNR}_{PSX}>4.5/\sqrt{N}$. Thus, sources with $\mathrm{SNR}_{PSX}>4.5/\sqrt{N}$ were deemed to be real and those with $\mathrm{SNR}_{PSX}<4.5/\sqrt{N}$ to be spurious. The cumulative distribution of the SNR from the image-based photometry, SNR_{im}, is shown in Figure 17. Sources with $\mathrm{SNR}_{PSX}>4.5/\sqrt{N}$ are plotted in black and the sources for which $\mathrm{SNR}_{PSX}<4.5/\sqrt{N}$ are in red.

More than 99% of the sources with $\mathrm{SNR}_{im}>10$ are expected to be real as judged by their SNR_{PSX} value. The sources have equal probability of being real or spurious at $\mathrm{SNR}_{im}\approx4$. We have set the minimum reliability in the MSX PSC to be 80%, which occurs at $\mathrm{SNR}_{im}=5$. Approximately 95% of sources are real at $\mathrm{SNR}_{im}=7$. Therefore, we can trace source reliability directly to the flux quality flag: a source with a maximum flux quality flag of 4 and $\mathrm{SNR}_{im}\geq10$ is reliable at the >99% confidence level. The reliability of flux quality flag = 3 sources will be at least 95%, and a flux quality flag of 2 implies a reliability for the source of >80%.

4.4 Completeness

Completeness is a difficult quantity to judge, especially in regions of high confusion and complex, structured emission such as along the Galactic plane. We estimated the completeness limits of PSC V2.3 both statistically, through the behavior of the differential and cumulative source counts in each band, and by comparing the catalog sources to a more extensive extraction of stars from two of the MSX deep raster scans.

4.4.1 Flux Histograms

We examined the differential and cumulative source counts in each band for the high latitude subcatalog and by quadrant for each of the five Galactic plane subcatalogs. We fit a linear slope to each cumulative distribution and find as expected that the slopes in the $\log N - \log F$ plots are shallower than those predicted by a Euclidean source distribution ($m \geq -3/2$). The slopes are generally consistent from band-to-band for each region. The steepest slope occurs in the first quadrant ($0° < l \leq 90°$), while the shallowest slope is seen in the high latitude data, which lies between Galactic latitudes of 6° and 80°. We also find that the cumulative source count slope is higher, by about 20%, in the B bands in all regions, which is likely due to the fact that the lower sensitivity B band data sample only relatively nearby stars which approximate a uniform density distribution.

The catalog completeness is estimated in two ways. First, the completeness is determined from the turnover point in the differential source counts. Second, it is estimated from the fraction of sources seen in the cumulative distribution versus the number expected from the linear fit to the distribution. This latter method is somewhat problematic in the first and second quadrants of the Milky Way, where Galactic structures (primarily the bulge and spiral arms) cause deviations from a linear slope to the source counts taken over such large areas. However, the plots should give a reasonable indication of the catalog completeness.

Band B_1 Figure 18 shows differential and cumulative source counts in Band B_1 from the high latitude catalog. The differential source counts for the highly reliable flux measurements ($Q \geq 2$) rise to about 30 Jy, then flatten out and fall off completely by 10 Jy. The source counts with lower quality flagged fluxes ($Q=1$) continue to rise below 30 Jy, peak at 20 Jy, then gradually decline to a minimum measured flux of $\sim$3 Jy. Comparison of the red and black dashed lines in the cumulative source counts indicates that including the $Q=1$ sources results in a deviation from the linear $\log N - \log F$ behavior, which is likely due to the flux overestimation in the lowest SNR sources. In the high latitude region, the B_1 data appear to be complete down to 30 Jy, and likely to 20 Jy if $Q=1$ sources are included.

The Band B_1 differential and cumulative counts of sources in the Galactic plane are shown in Figure 19, subdivided into quadrants. The differential source counts for the highly reliable flux measurements ($Q \geq 2$) also rise to about 30 Jy, then roll over and fall off by 20 Jy. The secondary peak between 3 and 12 Jy is due to faint sources extracted from the CB03 deep scan images within the Galactic plane; the source counts in the other MSX bands in the Galactic plane show a similar secondary peak. The images from the CB03s are approximately a factor of 6 more sensitive than the regular survey images, and therefore augment the lower flux density numbers in the catalog. The lower quality flagged fluxes ($Q=1$) also show a similar behavior as in the high latitude data, though the minimum detectable flux in the CB03 deep-scan regions is $\sim$1 Jy.

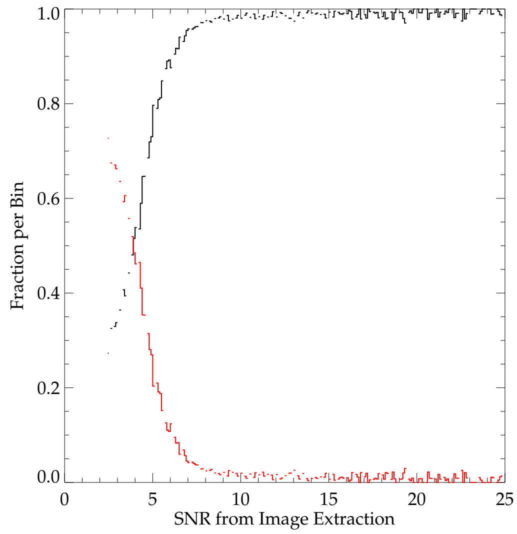

Figure 17: Reliability of image extracted sources under the assumptions given in Section 4.3.3.

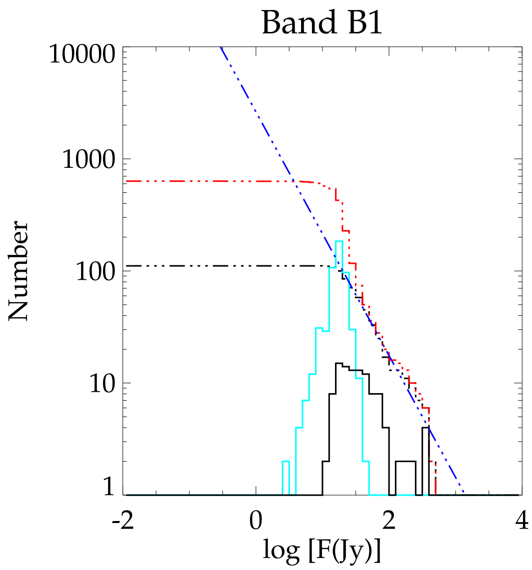

Figure 18: Band B_1 source counts (differential - solid line; cumulative - broken line) for the high latitude catalog. The black lines are those sources with $Q \geq 2$, the cyan line shows sources with $Q=1$, and the red dashed line plots cumulative source counts for $Q \geq 1$. The blue broken line is a linear fit to the cumulative source distribution between 30 and 150 Jy.

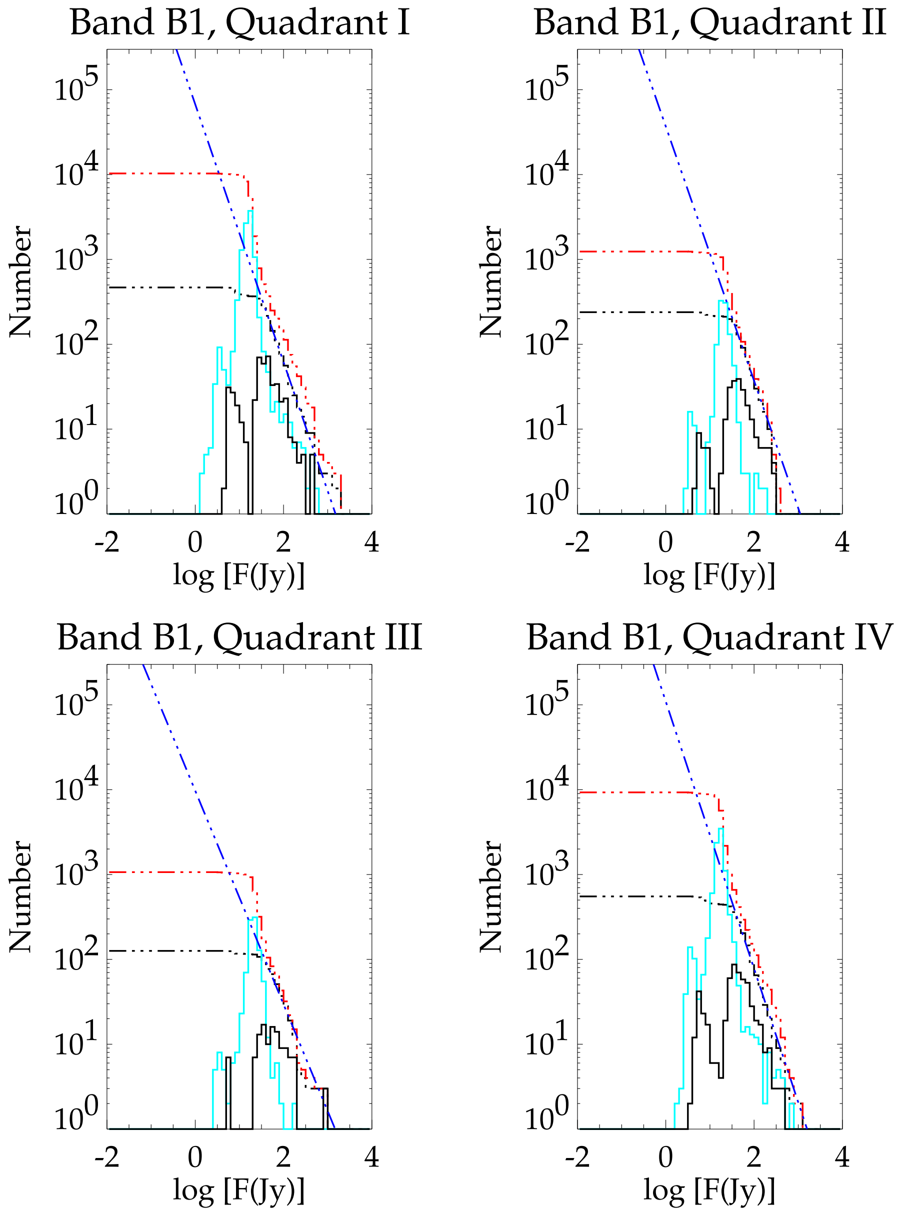

Figure 19: Band B_1 source counts (differential - solid line; cumulative - broken line) by Galactic quadrant. The lines are as for Figure 18.

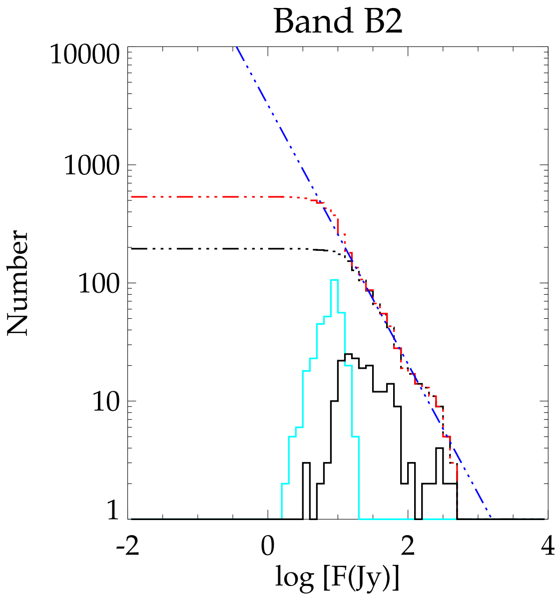

Figure 20: As for Figure 18, but for Band B_2

Band B_2 The Band B_2 differential and cumulative source counts are shown in Figure 20 for the high latitude subcatalog. The differential source counts for the highly reliable flux measurements ($Q \geq 2$) show an increase in cumulative counts to about 12 Jy, after which they flatten out and fall off completely by 3 Jy. The lower quality fluxes ($Q = 1$) continue to rise below 12 Jy, peak at 8 Jy, then gradually decline, with a minimum measured flux of $\sim$1.5 Jy. Comparing the red and black lines in the cumulative source counts indicates that including the $Q = 1$ sources results in a slight excess over the linear $\log N - \log F$ trend at fainter fluxes. The size of this excess indicates that we are seeing somewhat less flux overestimation in the lowest SNR sources than is seen in Band B_1. The better noise characteristics of the B_2 data is likely responsible for this. The B_2 data appear to be complete down to 12 Jy in the high latitude subcatalog, and likely to 8 Jy with inclusion of the $Q = 1$ sources.

Figure 21 shows differential and cumulative source counts for the B_2 band sources from the Galactic catalog. Here the differential source counts for the highly reliable flux measurements ($Q \geq 2$) rise until about 12 Jy, then roll over and fall off by 8 Jy. There is a secondary peak between 1 and 5 Jy from the CB03-based extractions. Again, from the cumulative source counts and the linear fit, we see that the $Q = 1$ sources introduce slight flux overestimation in the flux bins below 10 Jy in the first quadrant, but this effect is minimal or absent in the other quadrants. This indicates that the $Q = 1$ source fluxes may be included in the completeness estimate. Therefore, it appears that the survey is $> 90\%$ complete in Band B_2 above 10 Jy, and $> 50\%$ complete above $\sim$4 Jy.

Band A Figures 22 and 23 show the source counts in Band A out of and in the Galactic plane, respectively. The number of sources in the catalog with $Q_A = 1$ is negligible compared to the other bands. This results from the combination of the normal colors of astronomical sources and the fact that Band A is at least

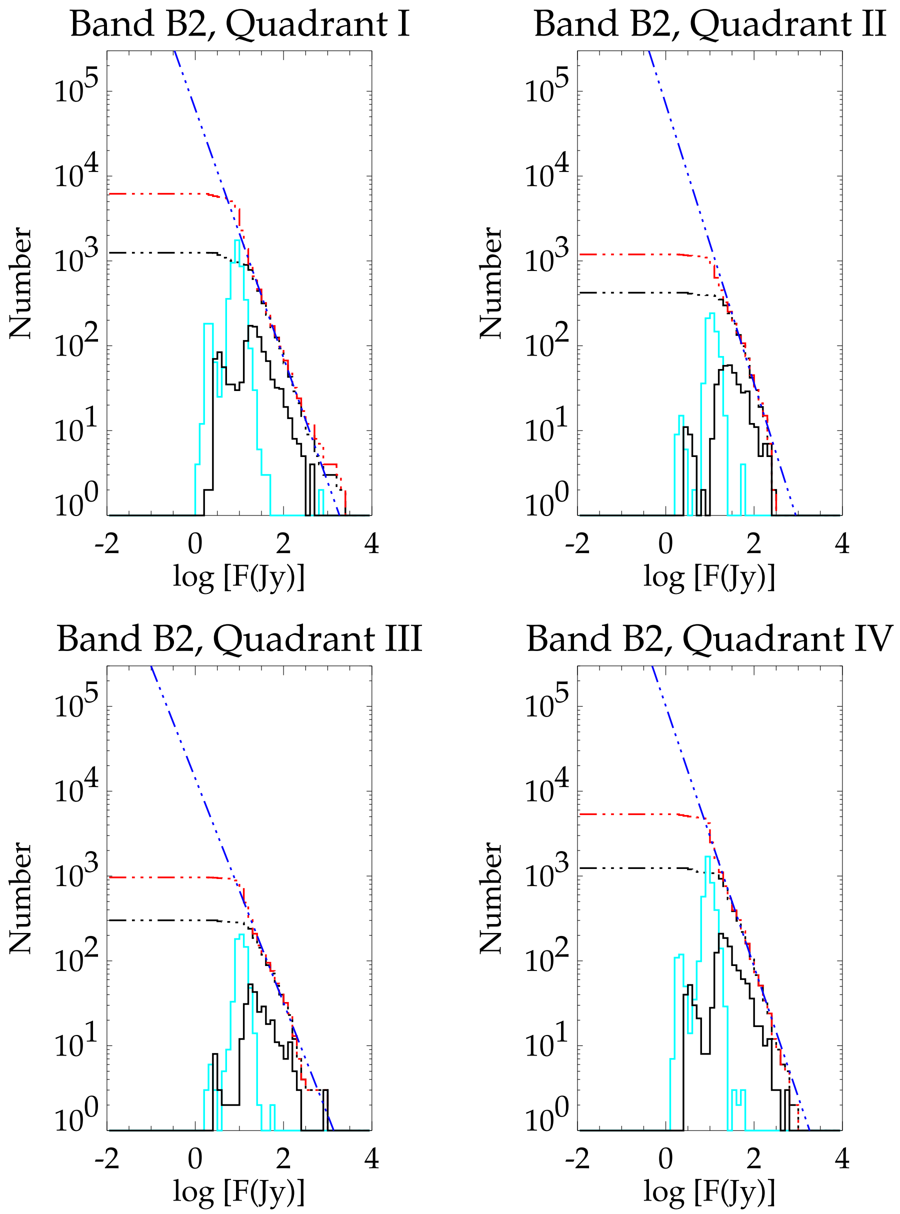

Figure 21: As for Figure 19, but for Band B_2.

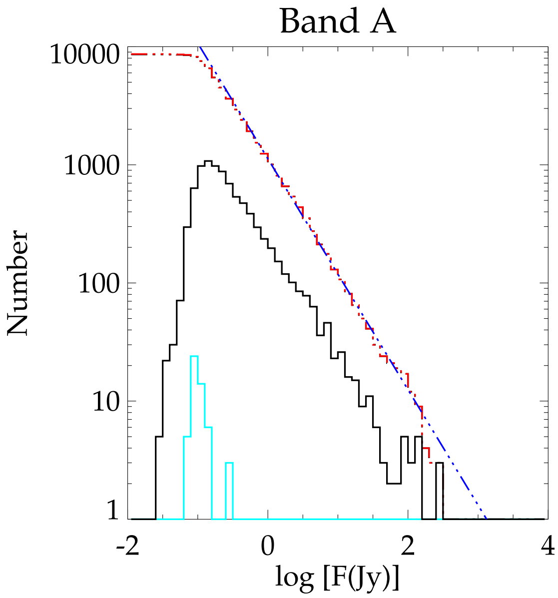

Figure 22: As for Figure 18, but for Band A.

10 times more sensitive than any of the other bands. Only a few sources are detected with the highest SNR in any band other than Band A, so the Band A measurement generally has the highest quality flux measurement. Since Band A photometry has the highest quality, and with $Q_a > 1$ in at least one band required for inclusion in the main catalog, few $Q_A = 1$ sources are contained in the catalog.

The Band A differential source counts (Figure 22) peak at 125 mJy in the high latitude catalog, though the deviation from the linear slope in this histogram and in the cumulative source counts indicates that the -0.8 dex bin is the last complete flux bin. This corresponds to 158 mJy, or mag 6.4 in Band A.

Figure 23 shows differential and cumulative source counts for the A band sources from the Galactic plane catalog. As for the high latitude data, the differential counts begin to roll over at 158 mJy, and drop precipitously below 100 mJy. There are several thousand sources between 20 and 100 mJy, primarily from the source extractions in the CB03 deep scans. The linear fit to the cumulative source counts in the second and third quadrants has a slope of ~ -1, consistent with a disk of uniform density. In the first and fourth quadrants, these slopes steepen slightly to -1.3 and -1.2 respectively, and deviate from linear behavior. The flattening of the slope below 1 Jy (mag 4.4) is consistent with the source count flattening for sources fainter than 5th mag in the IRAS 12 μm band in the inner Galaxy expected by Wainscoat et al. (1992) in their model of the Galaxy. Assuming that this flattening reflects the actual behavior of the source counts, and that the turnover in the differential source counts reflects the completeness limit of the survey, we estimate that the catalog is $> 90\%$ complete in Band A down to a flux limit of $\sim$158 mJy (mag 6.4) and $> 50\%$ complete above 125 mJy.

Band C Figure 24 shows differential and cumulative source counts for the C band sources from the high latitude catalog. The differential source counts for the highly reliable flux measurements ($Q \geq 2$) show the

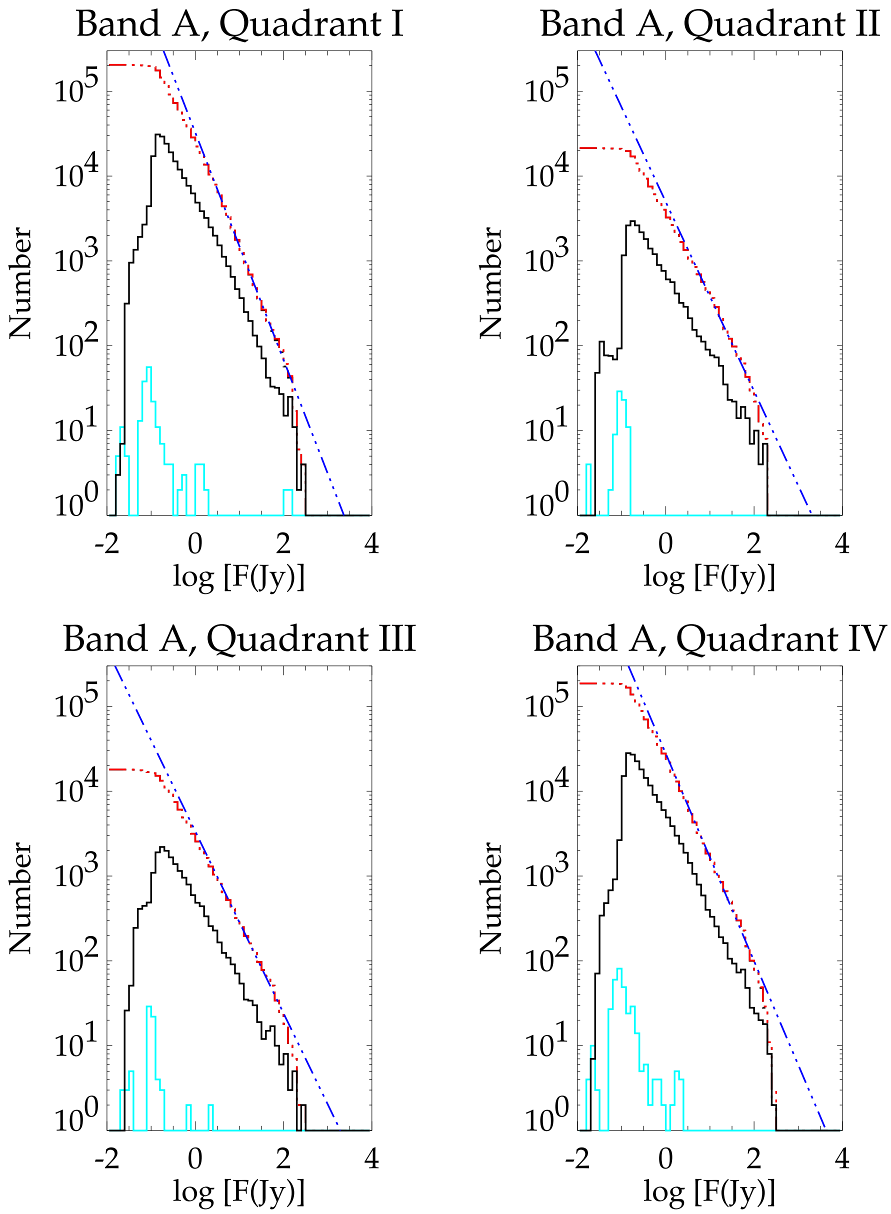

Figure 23: As for Figure 19, but for Band A.

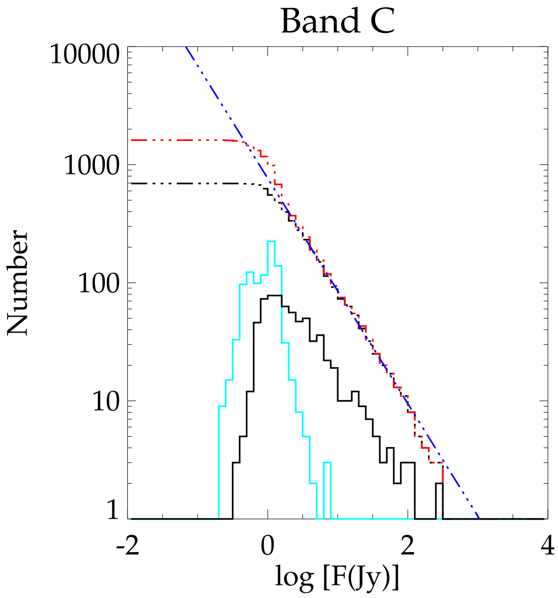

Figure 24: As for Figure 18, but for Band C.

source counts rising until about 1.25 Jy. The $Q = 1$ sources continue to rise through 1 Jy, although some bias of these counts due to flux overestimation is apparent. The minimum measured fluxes in the high latitude catalog are $\sim$0.25 Jy. The high latitude Band C data appear to be complete down to 1 Jy with inclusion of the $Q = 1$ sources.

In the Galactic catalog (Figure 25), the differential and cumulative source counts for the C band sources have slopes consistent with those found for Band A. The differential source counts for the highly reliable flux measurements ($Q \geq 2$) peak at 1.2 Jy, and the $Q = 1$ source counts peak at 1 Jy. The cumulative source counts show that the flux overestimation is minor (resulting in $< 20\%$ excess counts in the 1 Jy bin) for the $Q = 1$ sources. Including all Band C measurements in the cumulative completeness estimate, the catalog contains $> 90\%$ of all sources brighter than 0.7 Jy, and is $>50\%$ complete for sources brighter than 0.3 Jy.

Band D The Band D high latitude data (Figure 26) show similar behavior to that seen in Band C, although Band D is slightly more sensitive. The Band D differential source counts for the highly reliable flux measurements ($Q \geq 2$) rise to the 0.8 Jy bin. The $Q = 1$ sources exhibit a similar increase but also show a plateau of constant counts down to 0.3 Jy before dropping off. The minimum measured fluxes in the high latitude catalog are $\sim$0.2 Jy. In the high latitude region, the Band D data appear to be complete down to 0.8 Jy.

In the Galactic catalog (Figure 27) the differential and cumulative source counts for Band D again have slopes consistent with those found for Band A in each quadrant. The differential source counts for the highly reliable flux measurements ($Q \geq 2$) peak at 1 Jy, and the $Q = 1$ source counts peak at $0.6 - 0.8$ Jy, depending on the quadrant. The cumulative source counts, like those in Band C, show that the flux overestimation is minor (resulting in $< 20\%$ excess counts in the peak bins) for the $Q = 1$ sources. Including

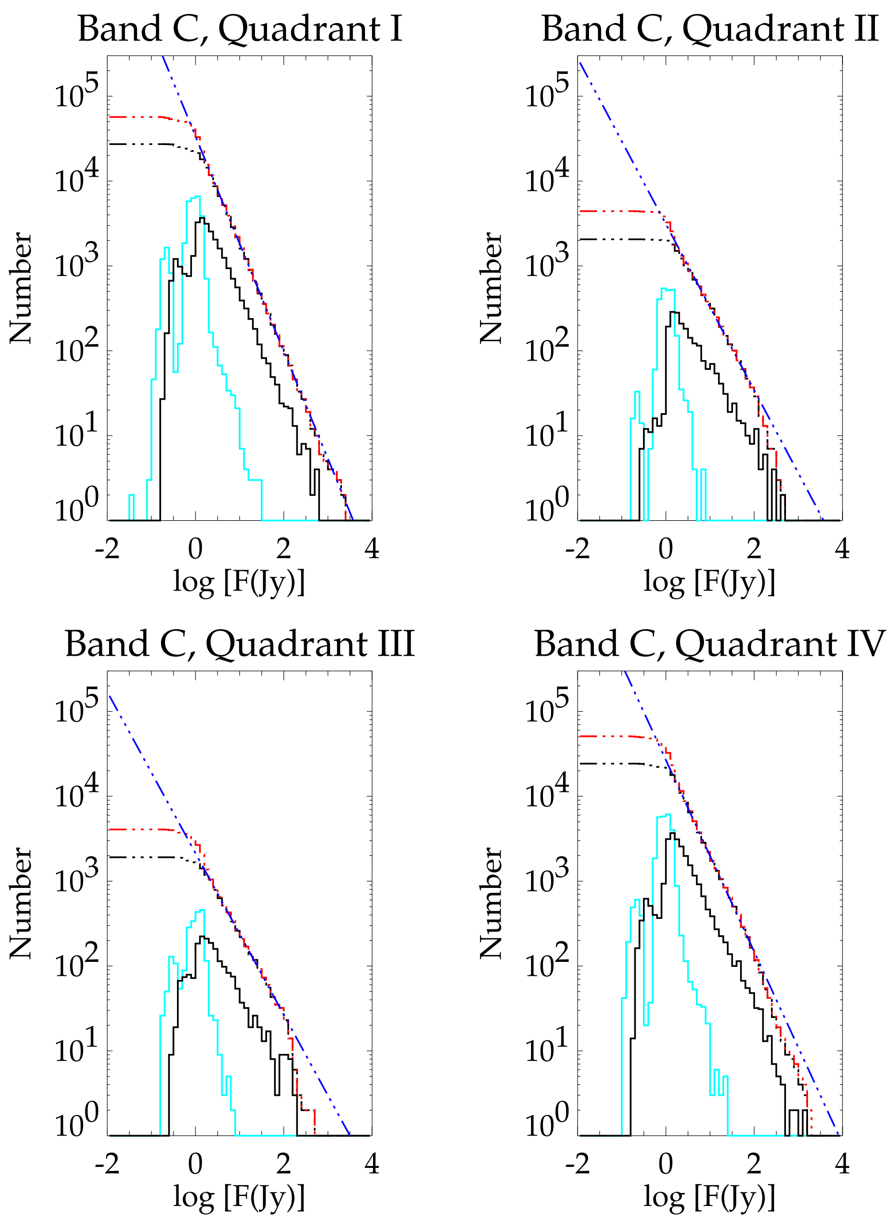

Figure 25: As for Figure 19, but for Band C.

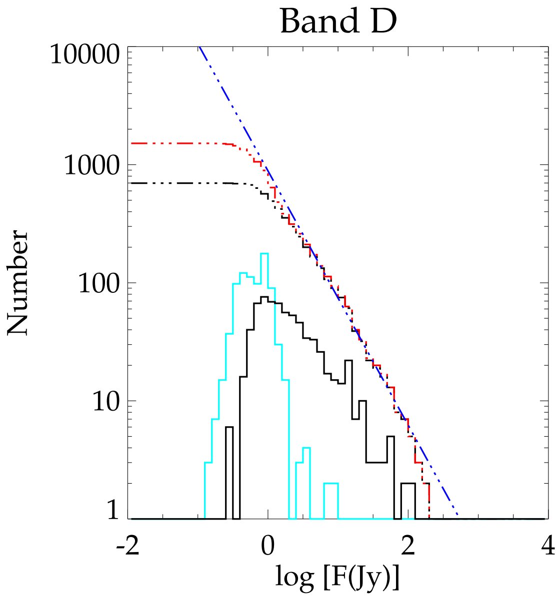

Figure 26: As for Figure 18, but for Band D.

all Band D measurements, we estimate cumulative completeness of $>90\%$ of sources brighter than 0.5 Jy, and $>50\%$ for sources brighter than 0.3 Jy.

Band E Fewer than 1000 sources were detected in the high latitude catalog because of the poor sensitivity of Band E. The differential and cumulative source counts from such a limited sample, shown in Figure 28, resulted rather ragged statistics. The Band E statistics are most similar to the Band B results. The differential source counts have a wide plateau between 1.5 and 50 Jy, with ~20 sources in each 0.1 mag bin for the highly reliable flux measurements ($Q \geq 2$). Like the B band data, there are a large number of low SNR ($Q = 1$) flux measurements that, in this case, lie between 0.3 and 4 Jy.

The much larger numbers of Band E sources available in the Galactic plane catalog (Figure 29) permit meaningful estimates of the catalog completeness in each of the four quadrants. The cumulative source counts in these figures do not follow the Band A slopes as closely as Bands C and D. Instead, the first and fourth quadrants have uniform disk-like slopes of ~ -1, while the second and third quadrants have flatter slopes, ~ -0.84. There is evidence from these source counts that a large fraction (~50% in the peak bins) of sources have a large flux overestimation bias in the $Q = 1$ subset. This is consistent with the poor noise characteristics of the Band E data. The differential source counts for the $Q \geq 2$ flux measurements peak around 3 Jy, with slightly better performance seen in the inner Galaxy versus the outer Galaxy. The $Q = 1$ source counts peak at ~2.5 Jy, with a plateau to 1 Jy. The secondary peak between 0.2 and 1.0 Jy arises from the faint sources extracted from the CB03 Deep image data. Including Band E measurements of all flux qualities, we estimate cumulative completeness of $>90\%$ of sources brighter than 1.5 Jy, and $>50\%$ for sources brighter than 1 Jy. Table 19 summarizes the in-plane completeness estimates for the MSX bands.

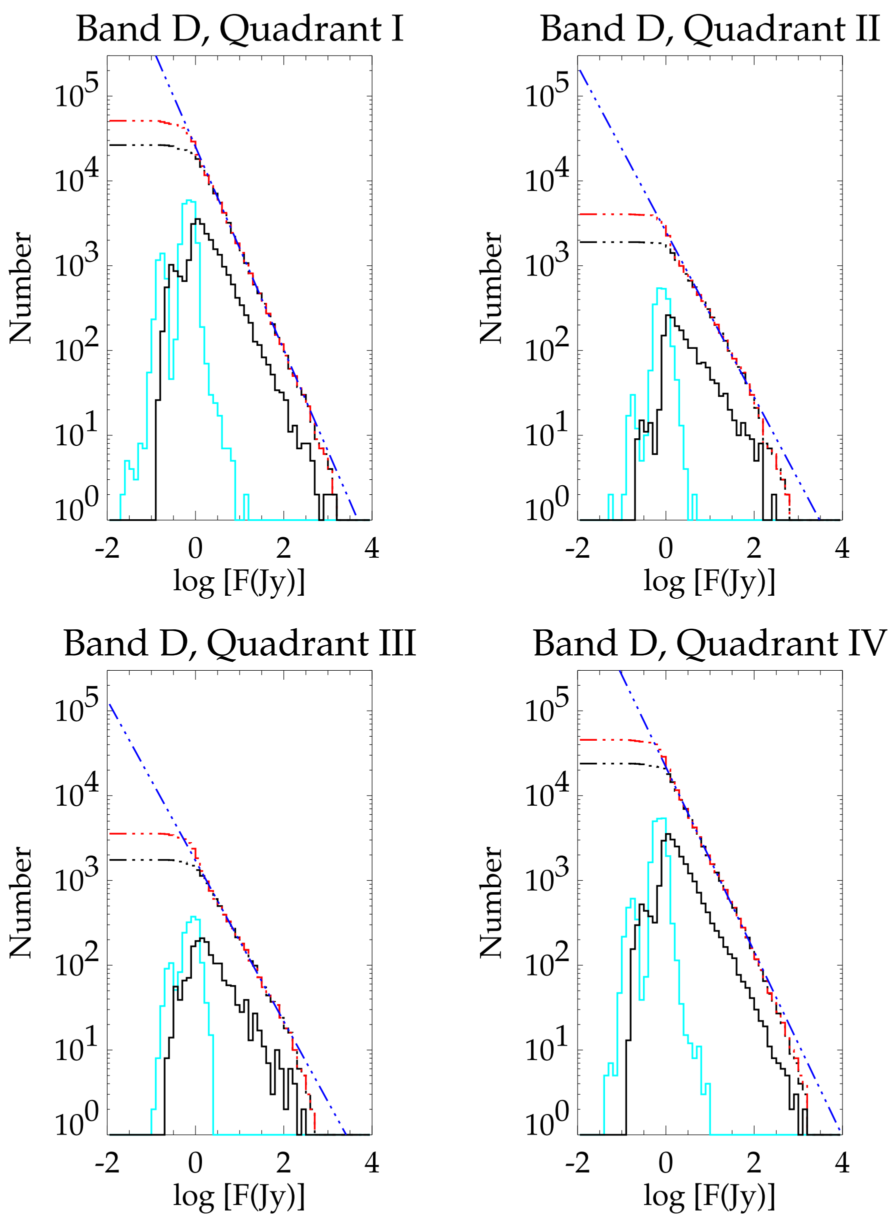

Figure 27: As for Figure 19, but for Band D.

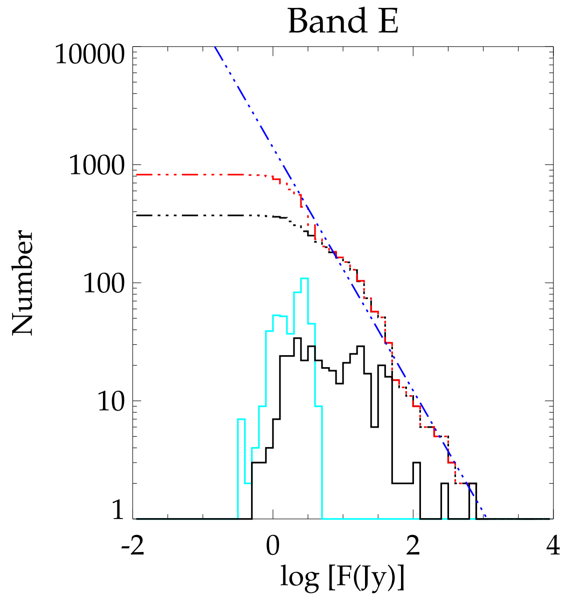

Figure 28: As for Figure 18, but for Band E.

4.4.2 Comparison of Catalog Band A Sources with Deep Survey Image Data

To verify the completeness levels estimated in Section 4.4.1, we compared the PSC V2.3 sources with an independent extraction made using DAOPHOT on two deep CB03 image plates. The CB03 images were created from raster scanned DCEs with 25 raster legs and executed at a scan rate ~2.5 times slower than the nominal rate used for the 180° long Galactic Plane Survey scans. We expect the noise level in these images to be approximately 7.5 times lower than a single CB02 long scan. Therefore, sources with an SNR_{PSX} of 5 would be SNR~38 sources in the CB03 images. By comparing the catalog data to the more complete deep scan observations, we can accurately judge the completeness limits of PSC V2.3.

We examined ~1 square degree from each of two deep scans: CB03_25 between $6.^{\circ}6<l<7.^{\circ}4$, $0.^{\circ}5<b<1.^{\circ}6$ and CB03_32 between $32.^{\circ}6< l <33.^{\circ}4$, $0.^{\circ}5<b<1.^{\circ}5$. In Figures 30 and 31, the black lines display the differential (solid line) and cumulative (dashed) histograms per magnitude bin of the Band A flux density distribution of sources in the PSC V2.3; and the red lines are the corresponding histograms derived from DAOPhot extractions from the CB03 Deep Scan images. The blue histogram in each plot is the flux distribution of the sources extracted ONLY from the DAOPhot run. Figure 30 shows the results for the CB03_25 region. We conclude that the PSC V2.3 is 100% complete at 100 mJy in this region. The 50% completeness limit, defined as the flux at which the PSC V2.3 contains only half of the sources reported in that flux bin by the DAOPHOT results, is at ~50 mJy. The CB03_32 region results are very similar, with Figure 31 showing 100% completeness to flux bins of 70 mJy and brighter, and a 50% completeness level seen at 40 mJy.

For bands other than A, both the PSX and DAOPHOT extracted the same sets of sources, indicating that the catalog approaches 100% completeness in these other bands, to the sensitivity limit of the MSX image data.

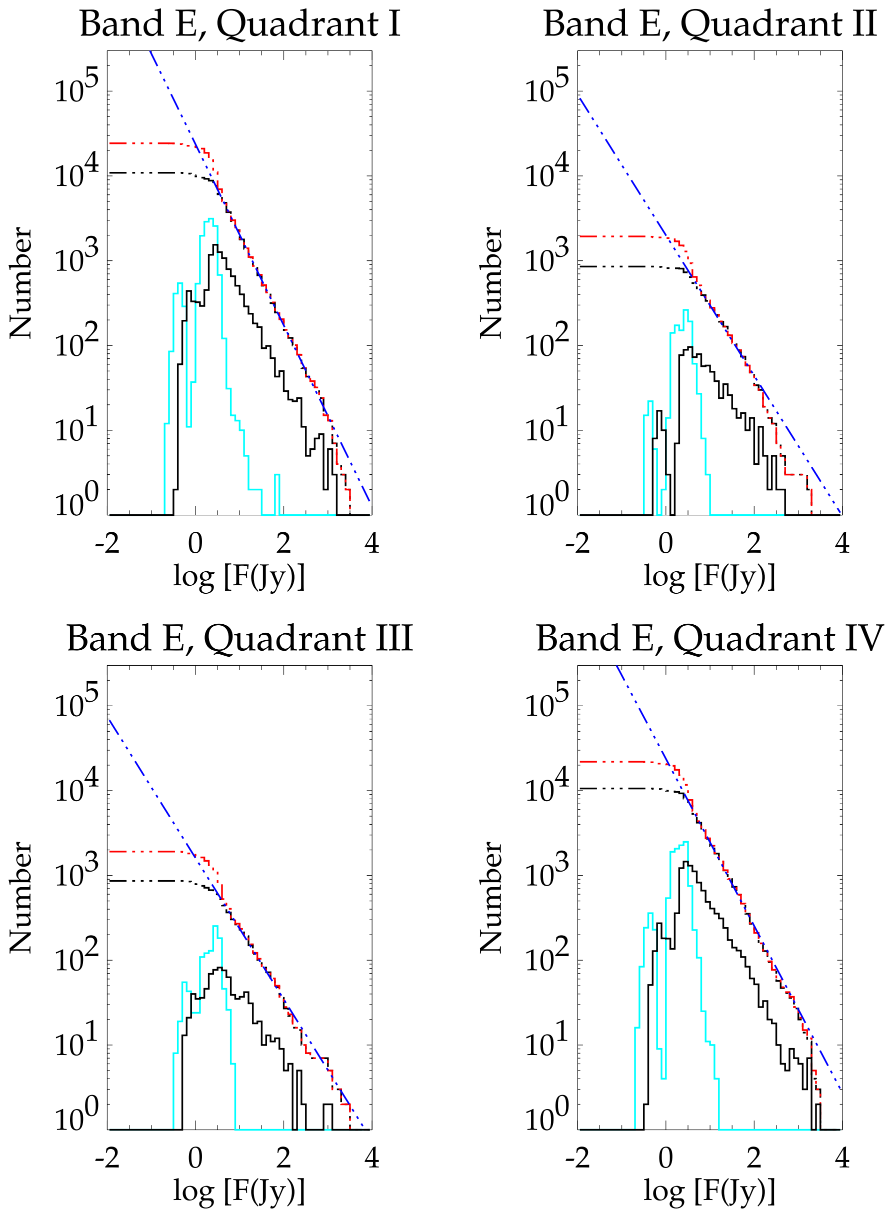

Figure 29: As for Figure 19, but for Band E.

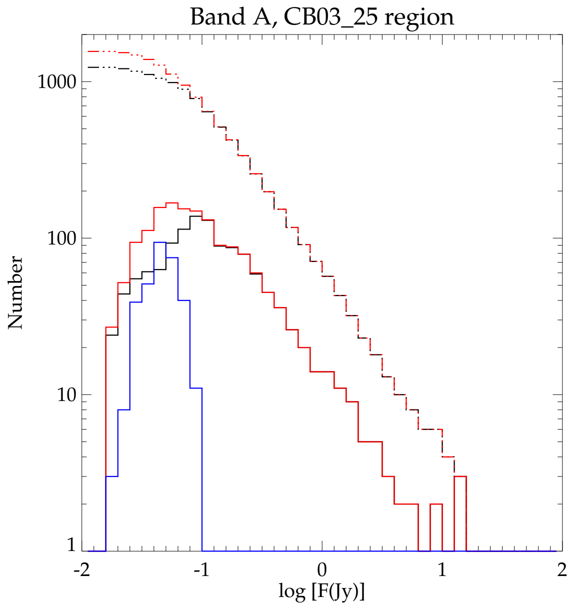

Figure 30: Band A source counts for CB03_25 region.

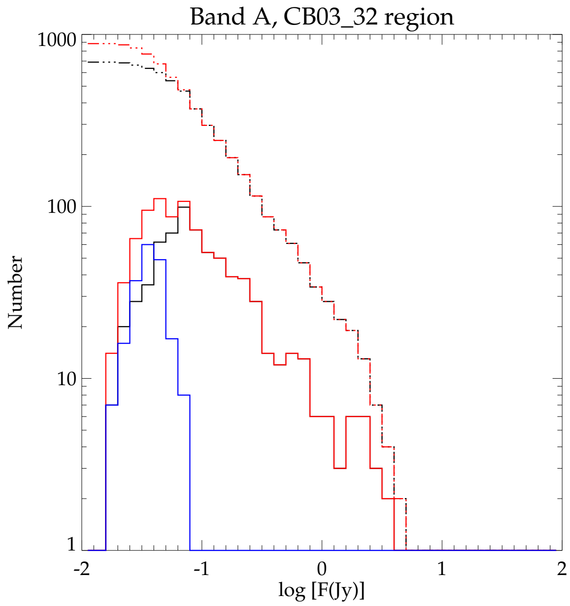

Figure 31: Band A source counts for CB03_32 region.

Table 19: PSC V2.3 In-Plane Completeness Estimates

Band	$\gtrsim$50%	$\gtrsim$90%
B_1	10 Jy	20 Jy
B_2	4	10
A	0.125	0.158
C	0.3	0.7
D	0.3	0.5
E	1.0	1.5

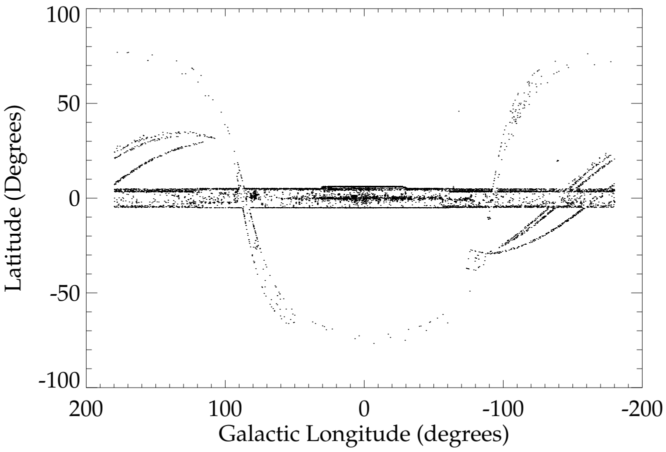

Figure 32: Spatial distribution (Galactic coordinates) of sources in the singleton catalog.

4.5 Singleton Sources Subcatalog

As a supplement to PSC V2.3 we have included a file containing sources that were extracted from only a single scan, but which passed the flux quality criteria required for catalog acceptance. A total of 12,179 sources are included in the singleton catalog. Of these, 11,802 have Band A measurements with $Q_A \geq 1$. For the remaining bands, the breakdown of singleton sources with $Q_a \geq 1$ is: B_1:380; B_2:334; C:3772; D:3415; E:1842. The spatial distribution of the singleton sources is shown in Figure 32. The primary sources of singletons are the CB01 scans, the edges ($|b| > 4.5$) of the Galactic plane survey and IRAS gap surveys, the mis-programmed anti-center CB02, and a cluster of sources near the Galactic center. Histograms of the distribution in Galactic coordinates are shown in Figures 33 and 34.

Figures 35 through 38 detail the differential and cumulative source counts as a function of source flux for the singleton catalogs in Bands A through E. We do not show the B bands because of the small number of sources. These data exhibit behavior similar to that seen in the main catalog, which gives confidence in the reliability of the singleton sources. As outlined by Price et al. (2001), the image construction took pains to remove asteroids, resident space objects, and artifacts that might have contaminated the singleton files.

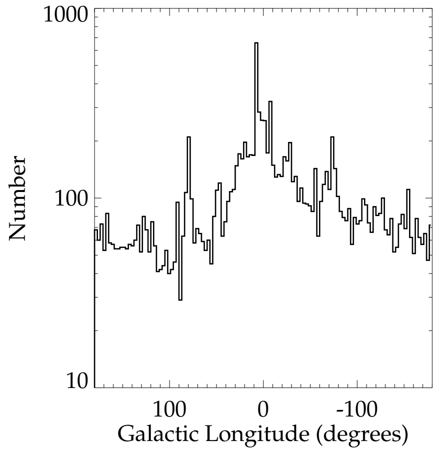

Figure 33: Galactic longitude distribution of singleton sources.

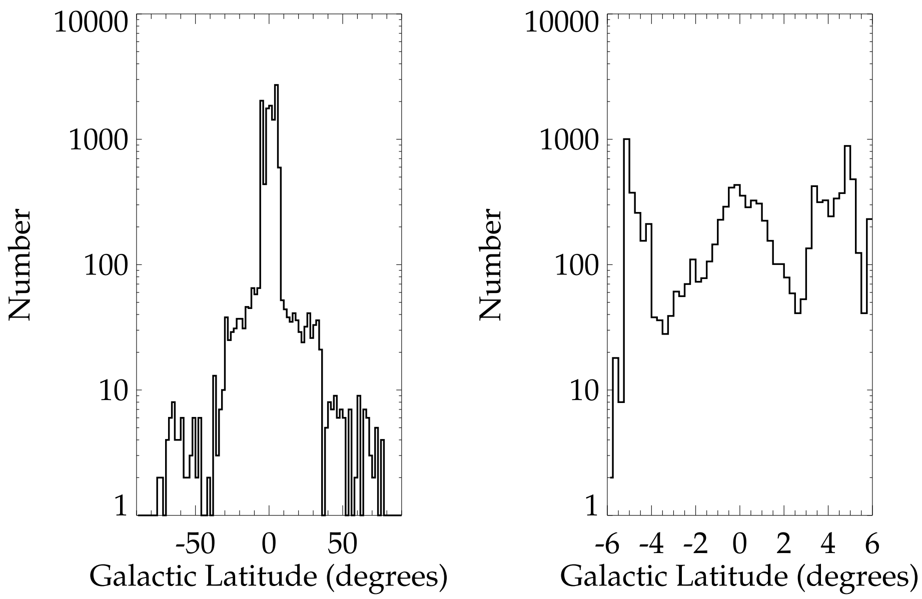

Figure 34: Galactic latitude distribution of singleton sources for (left panel) - full catalog; (right panel) - Galactic plane.

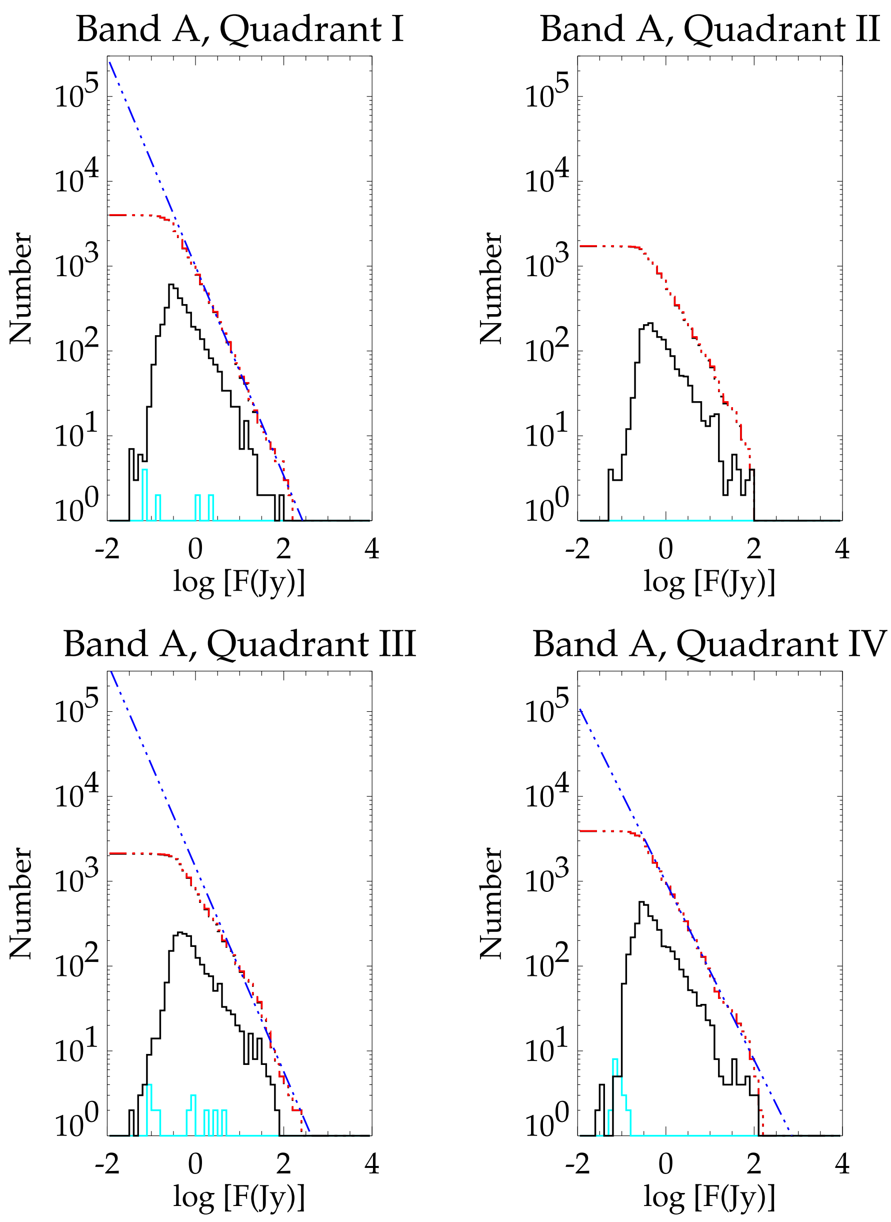

Figure 35: Source counts for the singleton sources in Band A. Colors and line styles as for Figure 27.

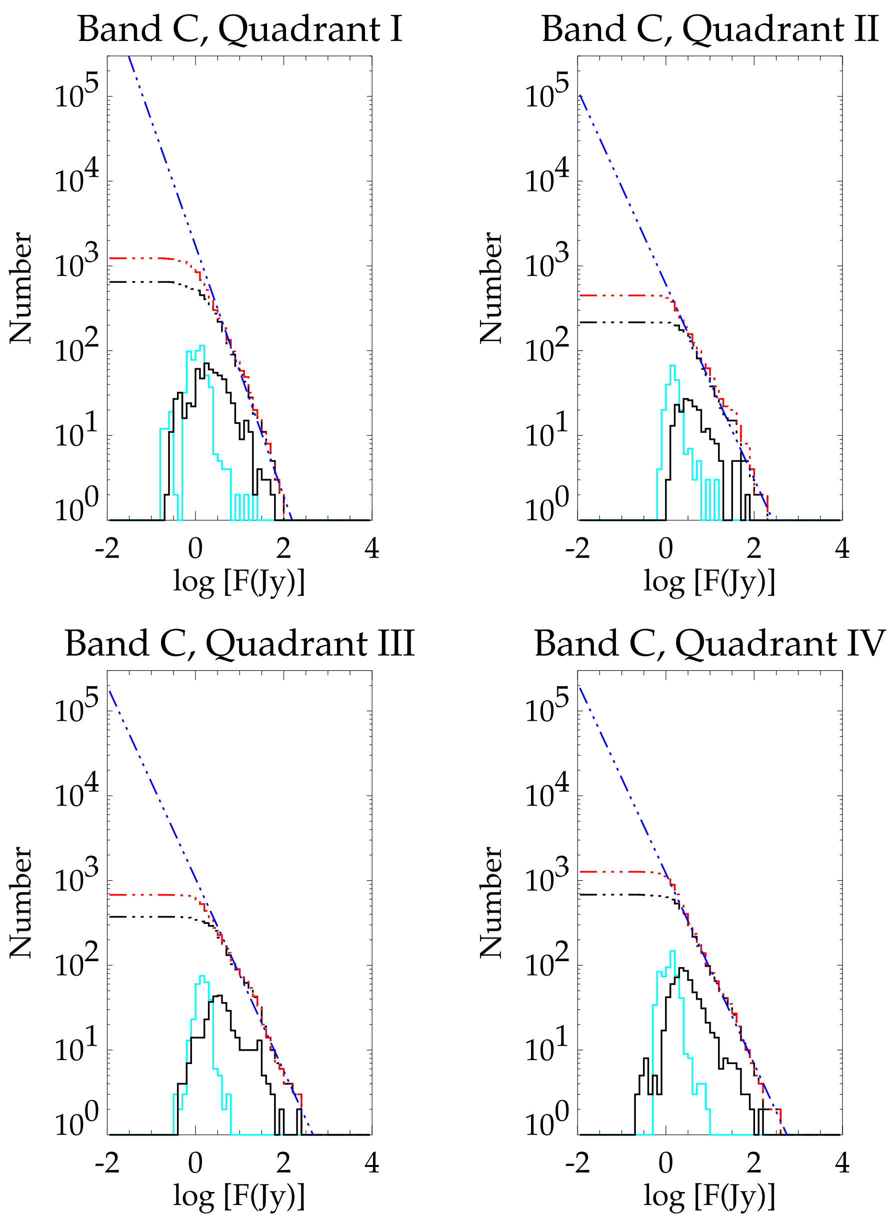

Figure 36: As for Figure 35, but for Band C.

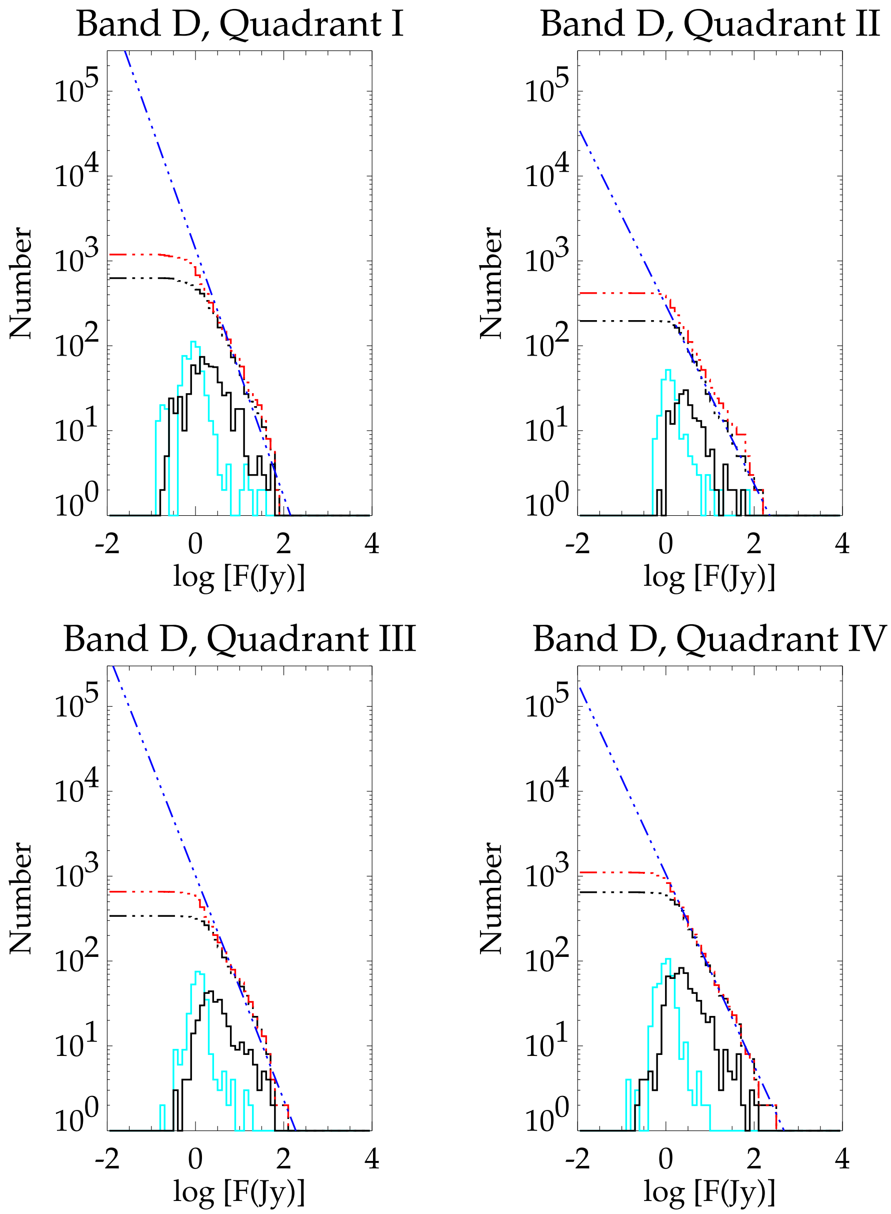

Figure 37: As for Figure 35, but for Band D.

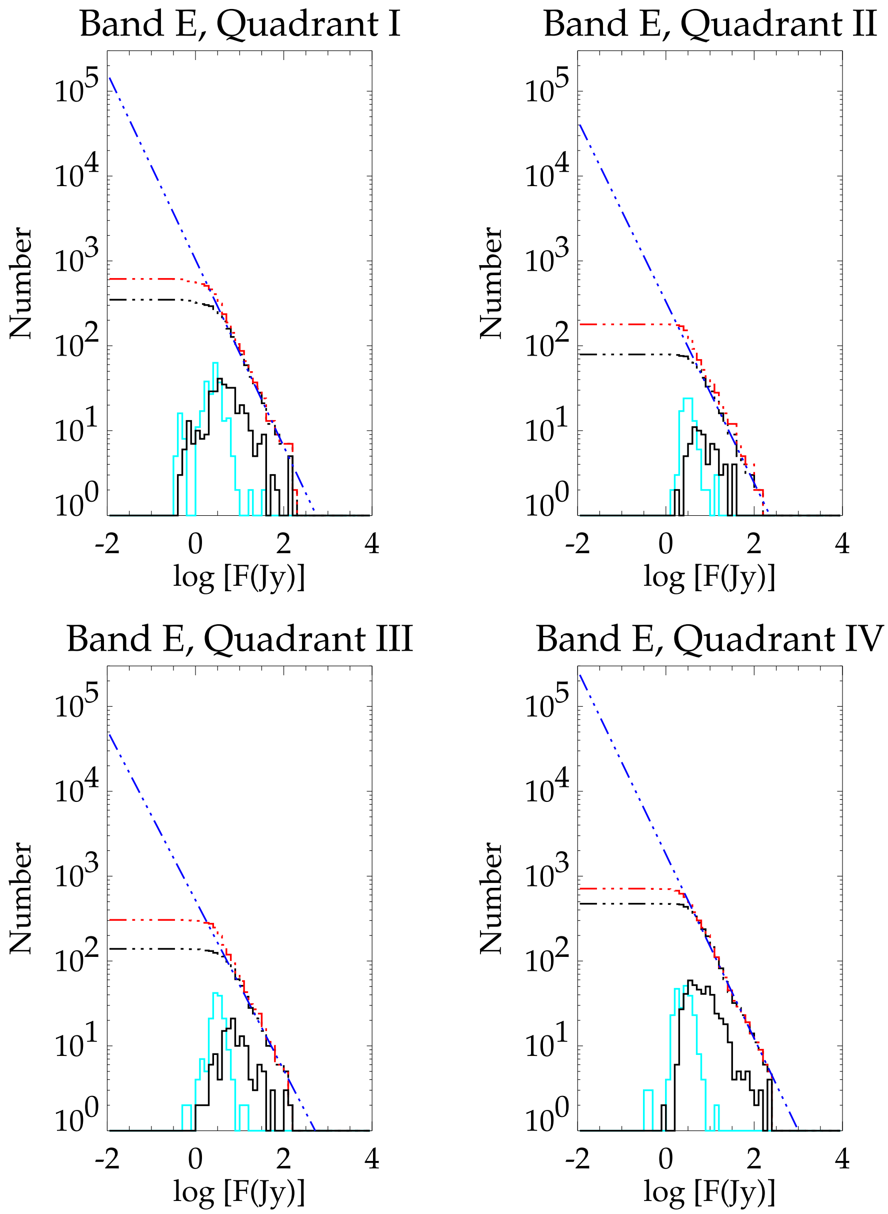

Figure 38: As for Figure 35, but for Band E.

4.6 Low Reliability Source File

We also include a supplemental faint source reject file containing sources with image-based signal-to-noise ratios between three and five. An analysis of the images and the fact that many of these sources were observed multiple times indicates they are in fact real. We expect, though, based on the analysis in Section 4.3, that these objects have a reliability of <80%. This file also contains 75,644 sources. In this case, the maximum flux quality in any band is $Q_A = 1$. The distribution of measurements is: A:75127; B_1:4029; B_2:1960; C:4481; D:4090; E:4671. Some of these are extended objects, or point sources embedded in extended diffuse emission. The different techniques used for background estimation between the PSX and the image-based extraction resulted in many faint sources embedded in emission to have lower SNR_{im} than SNR_{PSX}. Figures 39 through 44 detail the differential and cumulative source counts as a function of source flux for the low reliability catalogs.

4.7 Mini-Catalogs of Selected Areas

The Version 2.3 release of the MSX Point Source Catalog also contains mini-catalogs of sources for a number of isolated regions surveyed in raster scan mode. The processing was analogous to that for the main surveys, except that each region covered an area from one to $\sim$20 square degrees. Also, there was usually no temporal coverage, which rendered the variability flags moot, and individual scan legs were treated as separate events for PSX extraction redundancy. The targets within these regions consisted of galaxies (the LMC was included in the high latitude subcatalog), star forming and HII regions (W3 and the Rosette nebula were included in the Galactic plane subcatalogs), and three "blank" fields at high Galactic latitude.

The PSX source extractor was run for about half the fields by treating each scan leg as an individual scan. The position priors for eight of the galaxies, M31, NGC253, M33, NGC4631, NGC4945, NGC5055, M83, and M101, were extracted from the Band A images by Kraemer et al. (2002) using the DAOPHOT FIND routine, as mentioned in Section 1.2.3, as were the positions of the Band A sources for the Orion region (Kraemer et al. 2003). The DAOPHOT extractions were done before the PSX routines were run and, given the detailed assessment of the results by Kraemer et al. (2002, 2003), little could be added by using PSX. The image-based photometry on these fields used the positions determined by Kraemer et al., which were also associated with objects in SIMBAD.

Pointing and Registration The DAF improvement procedures for the mini-catalog observations are similar to those for raster scan DCEs discussed by Price et al. (2001). However, there are some differences that arise from the fact that these observations have fewer astrometric sources, which result in larger positional errors. We describe the processing for the galaxy images to highlight the issues.

The first step was to register the scan-to-scan offsets. MSX detected fewer than eight astrometric stars on each scan leg for three of the galaxies. For these DCEs, the average deviations between the in-scan and cross-scan astrometric sources and the MSX positions extracted for each scan leg were calculated and applied to the pointing as an initial refinement. This coarse adjustment was necessary because the individual legs exhibited large offsets from astrometric truth and from each other. Least squares cubic splines were fit to the in-scan and cross-scan deviations for each scan leg as a function of time for those galaxies, such as M31, that had eight or more matches between astrometric stars and sources in an individual leg. The spline knots were spaced to include minimum of four position updates between knots, and at least two knots are needed to describe the spline. The spline fits were verified by visual inspection to make sure that they did not "wander" excessively between knots. Subsequently, iterations were made to refine the registration of the individual scan legs to the source positions averaged over all legs. The positions of the astrometric sources

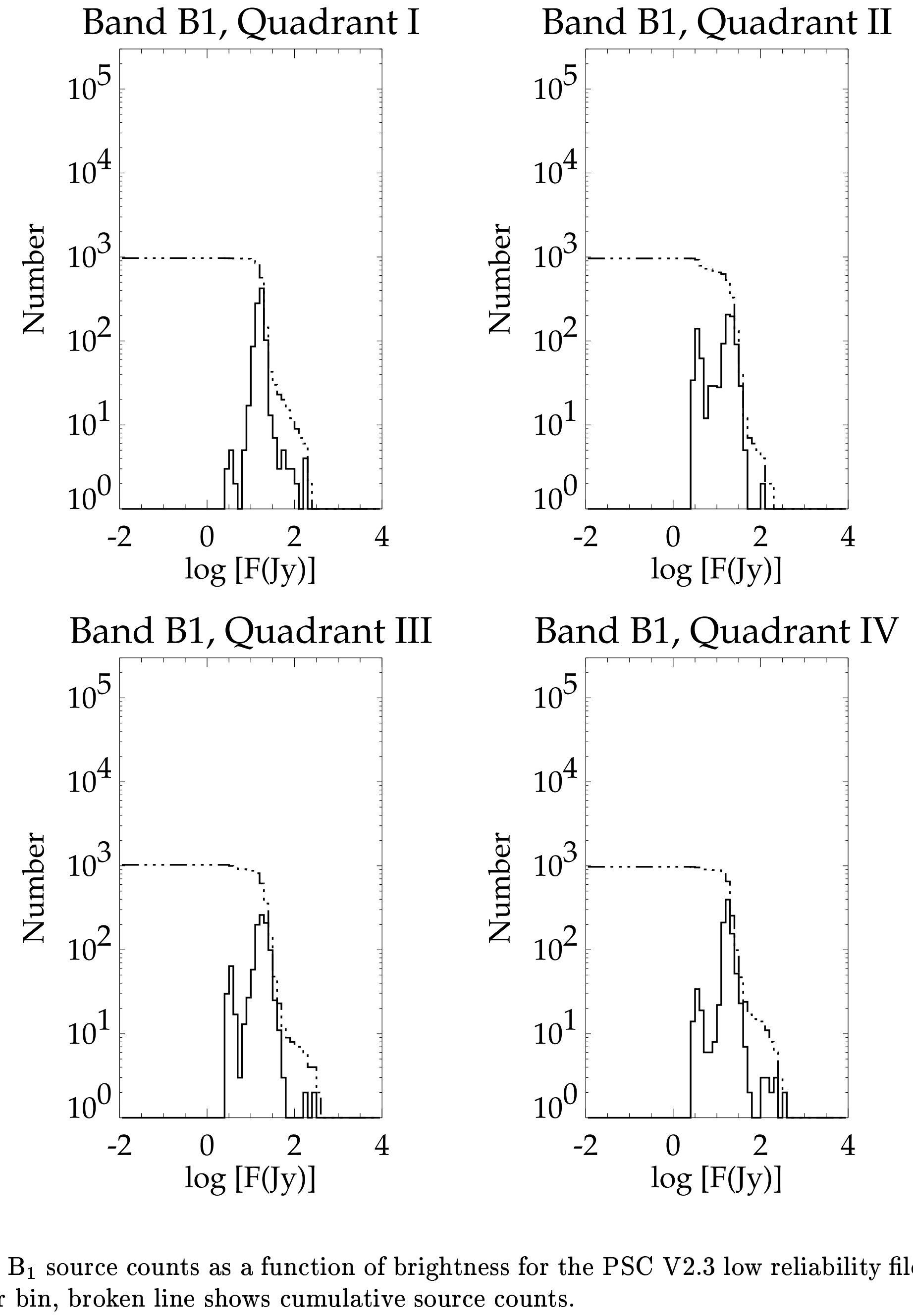

Figure 39: Band B_1 source counts as a function of brightness for the PSC V2.3 low reliability file. Solid line shows counts per bin, broken line shows cumulative source counts.

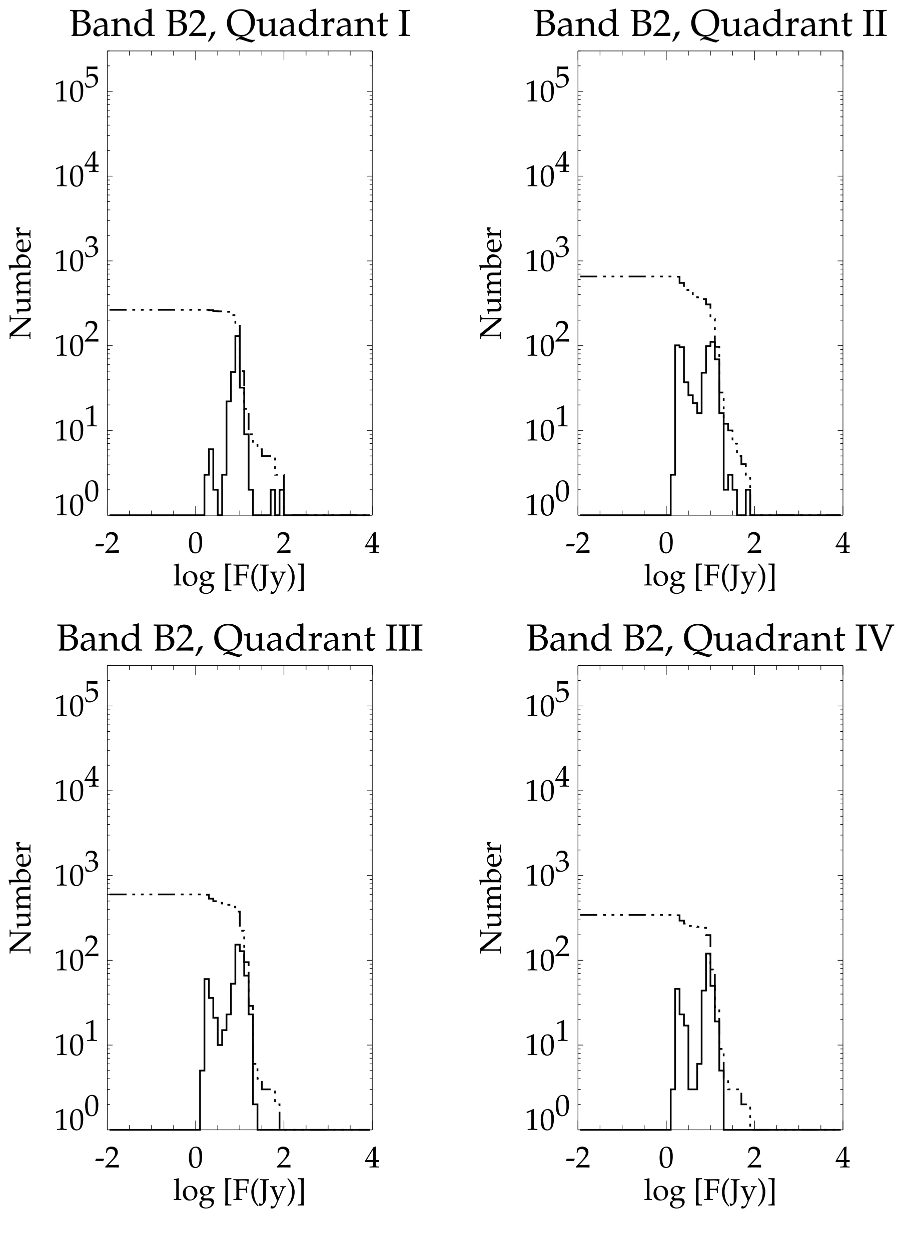

Figure 40: As for Figure 39, but for Band B_2.

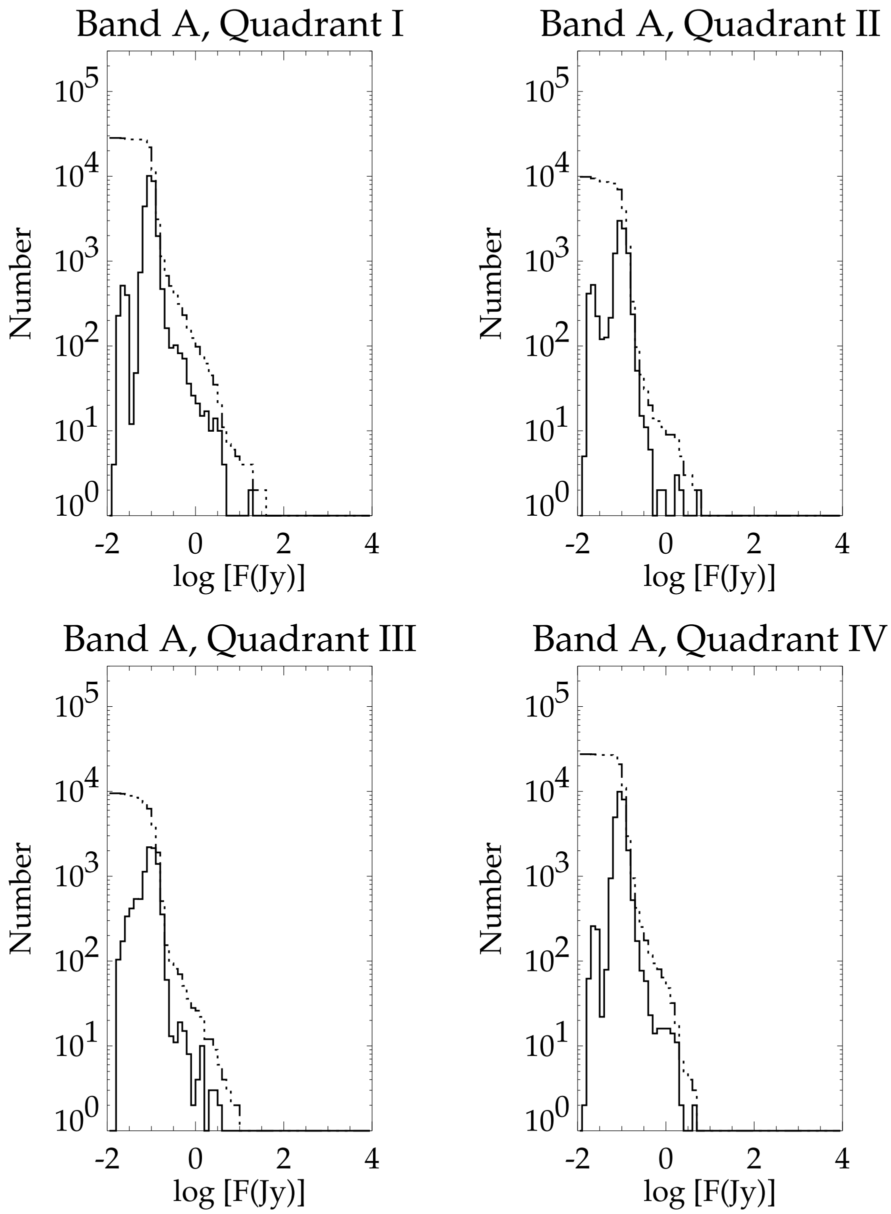

Figure 41: As for Figure 39, but for Band A.

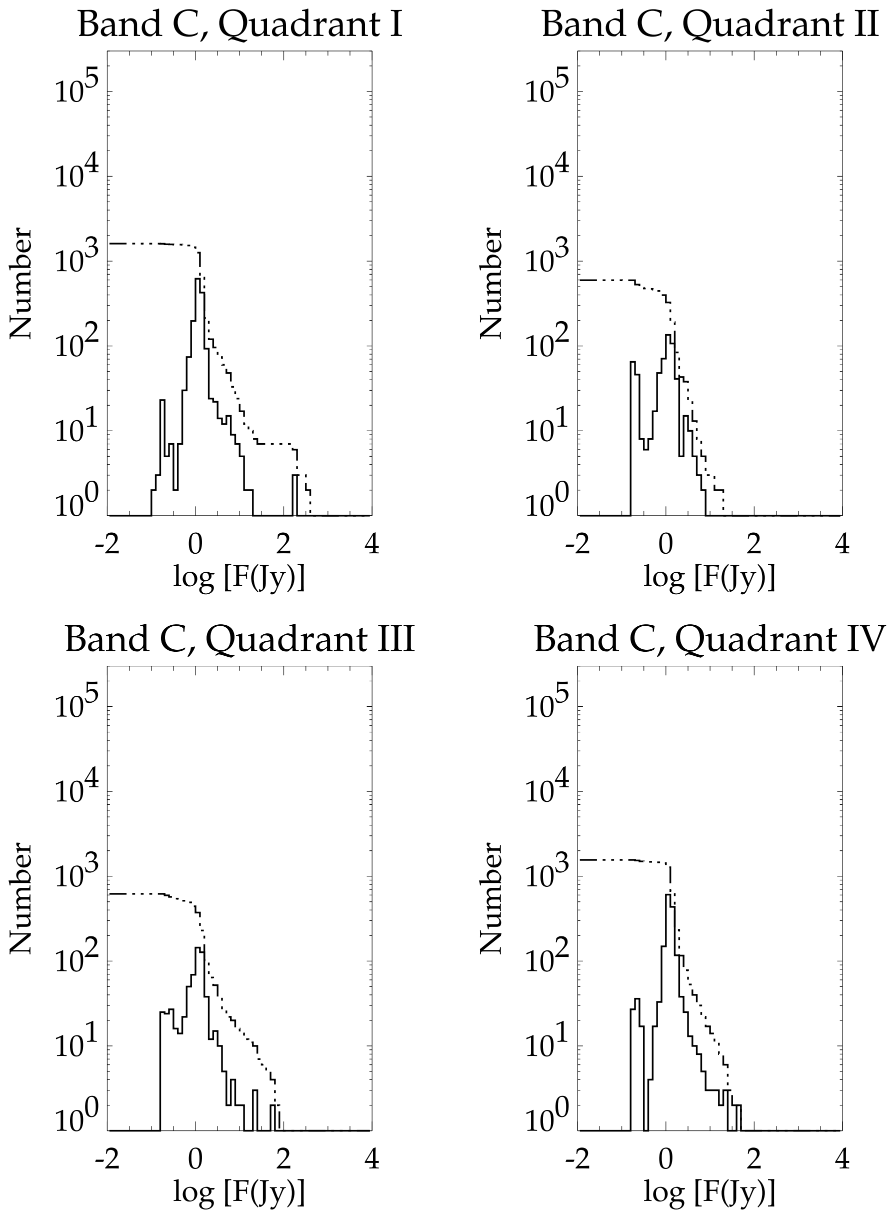

Figure 42: As for Figure 39, but for Band C.

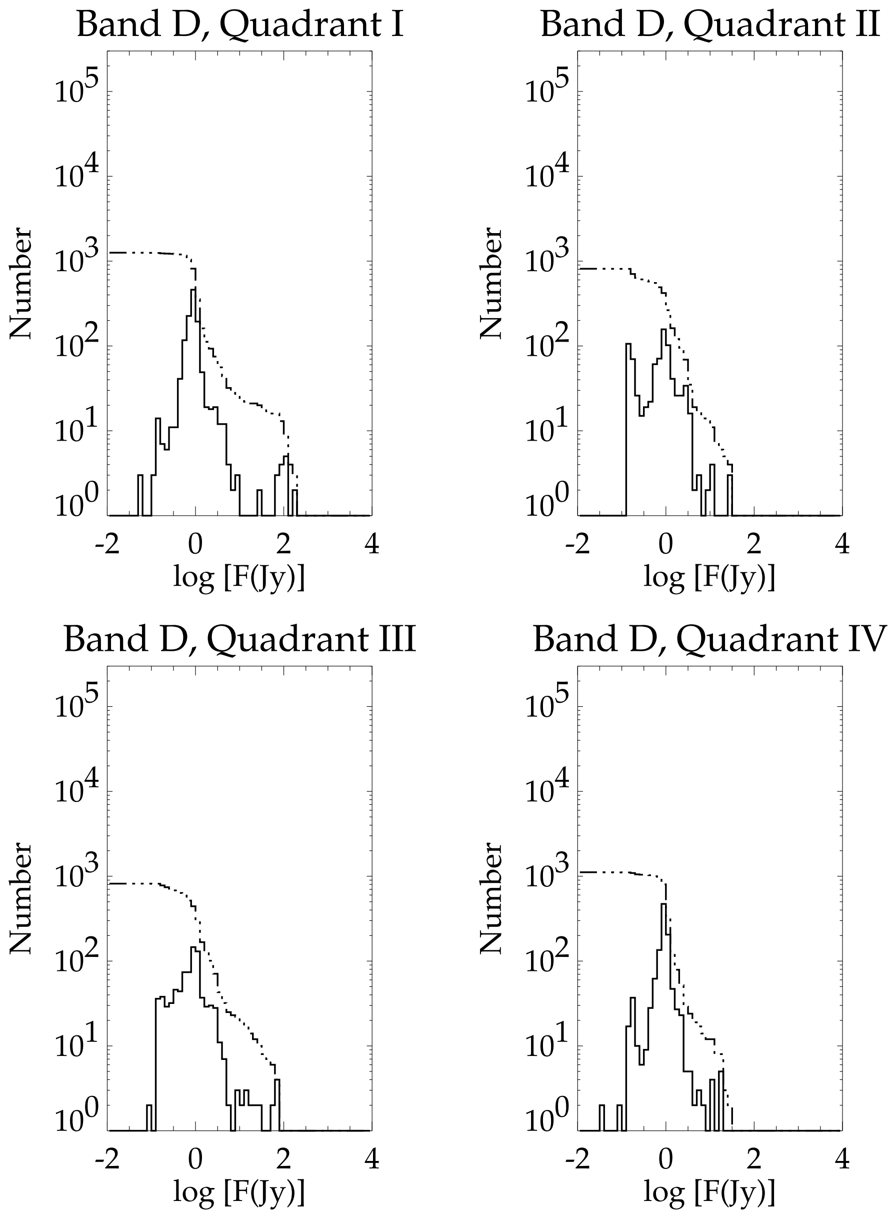

Figure 43: As for Figure 39, but for Band D.

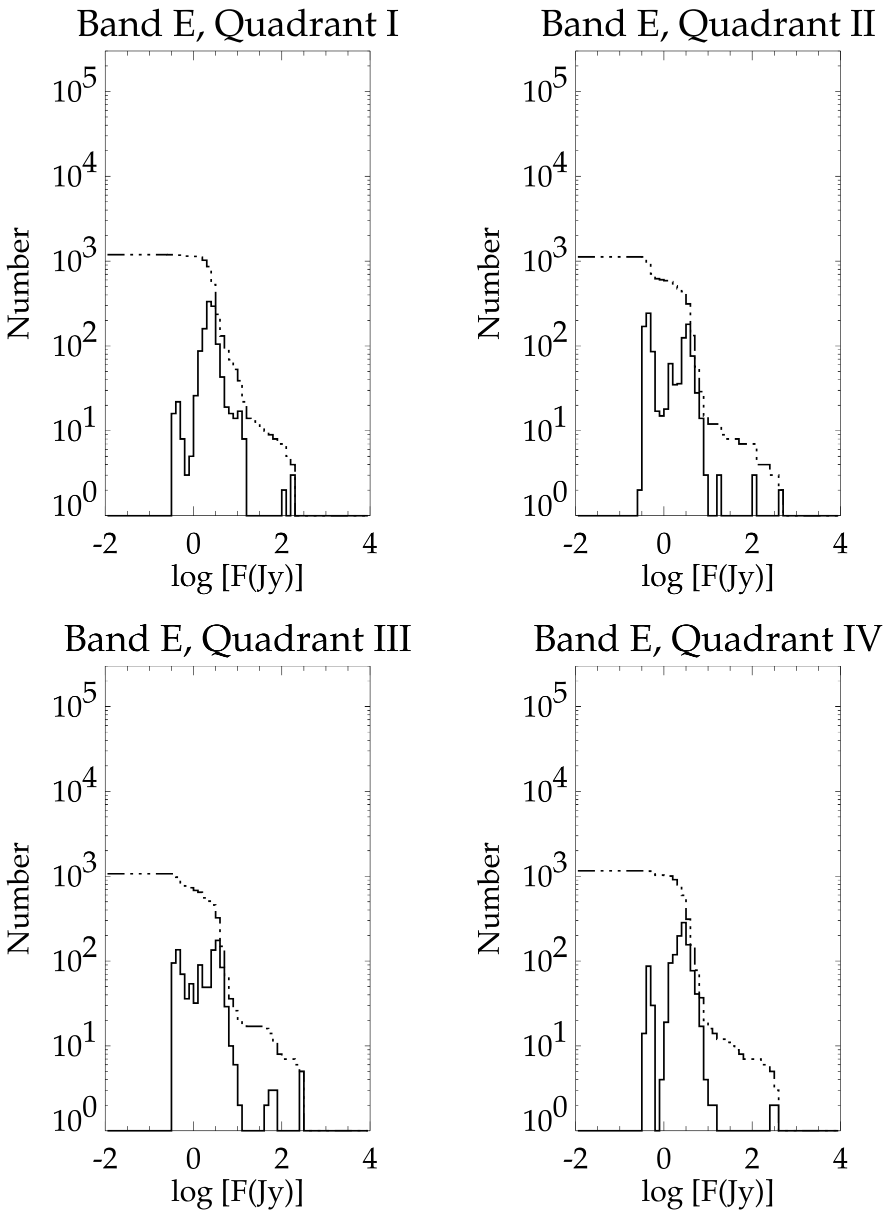

Figure 44: As for Figure 39, but for Band E.

were included in the registration on even iterations. The solution converged within the four iterations performed for all CB05 galaxy rasters.

A final registration was performed on the NGC4631 (CB05_58) observations during construction of the final image. One raster leg image was chosen as the fiducial and the emission peak in each of the other images was compared to it to align the scan legs. A 50×50 pixel (300″×300″) region encompassing the galaxy was selected from each raster image, the emission centroid in that box was determined, and the difference between the emission centroid for a given leg and the fiducial leg was used as the offset. We also performed the cross-correlation between the images from the individual raster legs. The position offsets from the cross-correlation were comparable to those produced by the centroiding method. We believe that the centroid offsets are more reliable because of the rather low signal-to-noise of the emission in the individual raster images.

Results The areas covered and the number of sources detected, in both the main, singleton, and low reliability mini-catalog for each region are listed in Table 20. The astrometric uncertainties for each final image are determined from the variance of the offsets of the centroids of sources in the image and their associated astrometric sources.

5 An Assessment of the MSX Point Source Catalog Version 1.2

Version 1.2 of the MSX Point Source Catalog contained 323,052 sources in the Galactic plane, which is about three times more than in the IRAS catalogs within the same region. The IRAS gap portion of the MSX PSC V1.2 contains 6,260 sources. Improvements in the extraction of candidate sources and determination of the fluxes have rendered the MSX PSC V2.3, which contains 440,487 sources, more reliable, more complete, with better photometric and astrometric accuracy than the previous version.

5.1 Photometric Accuracy

Cohen, Hammersley, and Egan (2000, henceforth CHE00) assessed the flux calibration of the MSX PSC V1.2 by comparing the fluxes for the stars in common with Version 4 of the Calibration Network and the PSC. Cohen et al. (1999) describe Version 3 of the network while Cohen et al. (2001) used the MSX Celestial Backgrounds calibration experiments to assess the accuracy of that network. The results for the full CHE00 sample are reproduced in Table 21. Using the same set of network stars with restrictive selection criteria that we used to assess the calibration of the MSX PSC V2.3 in Section 2.4.4, we find that V1.2 has calibration biases, which are given in Table 22.

CHE00 concluded that the PSC V1.2 calibration was, generally, within the uncertainties for Bands A, C, and D but that there may be systematic biases in the B bands and Band E. Our re-evaluation of the V1.2 calibration confirms CHE00s result for the entire calibration ensemble. However, we also find that the V1.2 results as a function of SNR show the same trends seen in the PSX flux data shown in Figures 2 through 4. While the mean ratios of the PSC V1.2 fluxes to the calibration stars are $\sim$1, PSC V1.2 did suffer from systematic biases in its flux calibration. Most notably, the fluxes were underestimated at low ($<$10) signal-to-noise levels and, at SNR $>$10, the bias increased linearly with increasing SNR, although the bias did remain within the limits of the quoted flux uncertainties for V1.2.

Table 20: Mini-Catalog Areas and Source Statistics

Area	No. Sources	$\sigma_{RA}('')$	$\sigma_{Dec}('')$	Comments
M31	99	2.43	1.63	DAOPHOT priors
NGC253	36	4.66	3.64	DAOPHOT priors
M33	52	2.82	3.83	Offset position correction, DAOPHOT priors
NGC4631	5	5.00	5.00	Offset + centroiding, DAOPHOT priors
NGC4945	56	3.13	2.67	DAOPHOT priors
NGC5055	4	2.96	2.63	Offset position correction, DAOPHOT priors
M83	52	3.19	2.46	DAOPHOT priors
M101	15	2.86	2.84	DAOPHOT priors
SMC	243	···	···	PSX Positions
Pleiades	107	···	···	PSX Positions
S263	101	···	···	PSX Positions
G300.2−16.80	188	···	···	PSX Positions
High Lat. fields	56	···	···	PSX Positions
S. GP field	39	···	···	PSX Positions
Orion	457	···	···	DAOPHOT priors
G159.6−18.5	172	···	···	PSX Positions
Taurus Cloud	28	···	···	PSX Positions

Table 21: PSC V1.2 Calibration Results from CHE00

Band	$F_{PSC1.2}/F_{Cal}$	σ	$F_{\min}$ (W cm^{-2})	$F_{\max}$ (W cm^{-2})	$N_{sources}$
B_1	0.922	0.019	1.60×10^{-17}	1.5×10^{-15}	40
B_2	0.947	0.016	1.67×10^{-17}	2.2×10^{-15}	45
A	0.995	0.005	2.0×10^{-18}	4.1×10^{-15}	107
C	0.991	0.006	2.8×10^{-18}	4.8×10^{-16}	55
D	0.987	0.008	1.7×10^{-18}	2.9×10^{-16}	56
E	1.069	0.025	1.3×10^{-17}	1.8×10^{-16}	15

Table 22: PSC V1.2 Calibration Results Using the Restricted Calibration Star Set of PSC V2.3

Band	$F_{PSC1.2}/F_{Cal}$	σ	$F_{\min}$ (W cm^{-2})	$F_{\max}$ (W cm^{-2})	$N_{sources}$
B_1	0.891	0.116	3.06×10^{-17}	7.64×10^{-16}	31
B_2	0.896	0.102	5.01×10^{-17}	3.1×10^{-15}	37
A	0.909	0.087	1.5×10^{-18}	5.36×10^{-15}	106
C	1.007	0.088	2.83×10^{-18}	6.55×10^{-16}	59
D	1.002	0.086	2.97×10^{-18}	4.09×10^{-16}	56
E	1.085	0.071	9.78×10^{-18}	2.57×10^{-16}	20

5.2 Astrometric Accuracy

The PSC V1.2 used the original APL Definitive Attitude Files (DAFs). While nominally accurate to 20 μrad, the DAFs suffered from occasional excursions of hundreds of microradians when the star camera was affected by glints or lost lock under other problematic conditions. Averaging multiple detections of the sources in PSC V1.2 resulted in in-scan and cross-scan position uncertainties of approximately $2''$. Comparison of the positions of sources in V1.2 with the astrometric positions for the corresponding source in the MSX IR Astrometric Catalog (Egan and Price 1996) showed that the quoted positional uncertainties in the PSC V1.2 agreed well with the measured errors: the deviations have an overall Gaussian distribution but with extended wings. The extended wings indicated that some of the sources had larger than expected errors, most likely due to large DAF errors. Lumsden et al. (2002) also noted that some of the brightest sources were poorly correlated ($>10''$) with the known position. The large positional errors for very bright sources was likely created by a poor PSF fit to a saturated source; the default CONVERT 5 processing eliminated all detector values after saturation. For a small number of overlapping scans, two or more extremely bad DAFs (off by 200 μrad or $\sim 40''$) conspired to give duplicate sources: one with an accurate position, and another with a nearby, discrepant position. There are approximately $\sim$1000 of these "ghost" sources brighter than 0.5 Jy in Band A in PSC V1.2. They are primarily centered in the regions around $(l, b) = (30^\circ, 1\overset{\circ}{.}5)$, $(15^\circ, 4\overset{\circ}{.}0)$ and $(315^\circ, 3\overset{\circ}{.}0)$, where the DAF solution failed, but other areas contain a few discrepant sources as well. The PSC V2.3 was created using DAFs with markedly improved positional accuracy, as described in Section 4.2. The accuracies cited in Table 18 are improved by more than $1''$ in-scan and more than $0\overset{''}{.}5$ cross-scan over those cited for the same table in V1.2.

5.3 Reliability and Completeness

To provide the community with a catalog as quickly as possible, we processed the MSX data for V1.2 with the CONVERT 5 software using the program-approved certified processing. Certified processing flagged and eliminated some of the data, such as the values from a detector after it saturated, or all the data from an observation if the initial internal calibration sequence was missing. The default bad pixel mask was also used, which conservatively eliminated all the "out-of-bounds" detectors in all gains states of both the mirror-fixed and mirror-scanning modes. This mask "flagged" detectors that clustered in one or two locations in the bands, which meant that the sensor could miss detecting a star that transited that region. A track was not kept of the locations of these small "holes" in the coverage. Finally, all sources in V1.2 had to lie in an area scanned at least twice. This eliminated the sources at $|b|>4.5^\circ$ ($+4^\circ$ in the outer Galaxy), and between $3^\circ < b < 4^\circ$ in the outer Galaxy where a scan was misprogrammed into the southern Galactic plane. Thus, not all the areas surveyed were included in the catalog. The "holes" also reduced the maximum number of observing opportunities for a small number of sources but this was not accounted for in the inclusion criteria for the catalog. Because these factors affect such a small area of the total surveyed, though, they had a relatively small affect on the reliability and completeness of V1.2 of the catalog.

One measure of catalog completeness is given by the maximum source density extracted along the Galactic plane. In Figure 45 we plot the number of sources per square degree along the Galactic equator from PSC V1.2 (red) and V2.3 (black). The revised candidate source selection criteria and the improved noise estimation in the plane improved the fidelity of the source extraction in the inner Galaxy. Where V1.2 had an extraction limit of $\sim$500 sources per square degree, V2.3 has more than 2,000 sources per square degree near the Galactic center, and typically 1,000 sources per square degree within $|l| < 30^\circ$. Problems in PSC V1.2 with regions of lower source density were also mitigated, such as when the fainter of a stellar pair was missed because it was

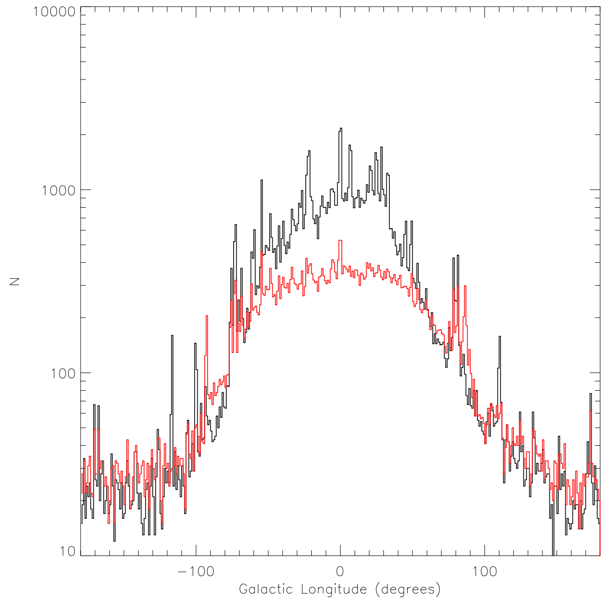

Figure 45: Source density between $|b| < 0\overset{\circ}{.}5$ for PSC V2.3 (black) and PSC V1.2 (red). Longitude bins are 1 degree, therefore bin totals are sources per square degree.

too close to a brighter companion. The other difference seen in Figure 45 is that the contents of the PSC V2.3 do not have spurious sources at the points where the CB04s and CB01s crossed the Galactic plane.

A total of 36,673 sources from PSC V1.2 had no matches with those in any of the PSC V2.3 subcatalogs (including the low reliability and singleton supplements to V2.3). Figure 46 shows the flux distribution of these sources in Band A. Approximately 90% of these sources had reported flux densities below 158 mJy. The sources brighter than 158 mJy that make up the linear portion of the source count distribution are the "ghost" sources created by the bad DAF files discussed above.

The six main V2.3 subcatalogs contain 276,277 sources that are matched to sources in the PSC V1.2. The cumulative source counts for these confirmed PSC V1.2 sources are compared to the source counts for each band from PSC V2.3 in Figure 47. The counts show the enhanced catalog completeness in Bands B, C, D, and E due to the increased sensitivity gained by extracting fluxes from the co-added images.

The difference in quoted fluxes due to the changes in the calibration and flux extraction method between the PSC V1.2 and V2.3 are shown in Figure 48. This figure plots the ratio of V1.2 flux to V2.3 flux as a function of source intensity for each band. The effect of the faint source underestimation, due to the background subtraction, can be seen in all bands as $F_{V1.2}/F_{V2.3}$ tails off toward $\sim$0.7 at the low SNR values. In Bands B, C, D, and E, and to a lesser extent in A, we see that the ratio then rises to $F_{V1.2}/F_{V2.3} > 1.0$ for the very faintest sources. These sources are typically V1.2 $Q_a = 1$ sources, which had upper limit flux values. The increased sensitivity afforded by the image extraction in V2.3 has resulted in better photometry for these sources, especially in the longer wavelength bands.

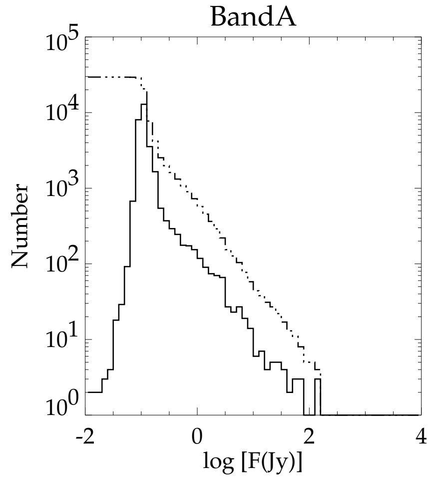

Figure 46: Band A source counts for PSC V1.2 with ***no*** counterpart in PSC V2.3.

Table 23: V2.3 Sources with Saturation Issues

MSX Name	Common Name	Affected Bands
MSX6C G287.5966−00.6307	η Car	ACDE
MSX6C G008.3436−01.0024	VX Sgr	A
MSX6C G080.7981−01.9210	NML Cyg	A
MSX6C G333.6044−00.2120	IRAS 16183−4958	ACDE
MSX6C G068.5387+03.2766	AFGL 2465	A
MSX6C G086.5361+03.7670	V Cyg	A
MSX6C G047.0645−02.5406	IRC+10420	A

6 Final Notes to the User

6.1 Artifacts Near Bright Sources

The SPIRIT III focal plane suffered from internal glints from the brightest IR sources, notably in the cross-scan direction. Typically these are not point-like and should have been removed by the cascade-average filtering process. However, it is possible that these glints may cause spurious companions to very bright ($\geq$ a few hundred Jy) sources. Other events, notably near η Car and NML Cyg, have been removed by hand in the final catalog construction process. However, users of the catalog should check cataloged sources against the image data near any extremely bright sources.

The seven sources which had obvious saturation issues in their catalog entries are noted in Table 23. The affected bands have had the flux quality flag set to 1 - regardless of the value given in the SNR_{im} and SNR_{PSX} columns.

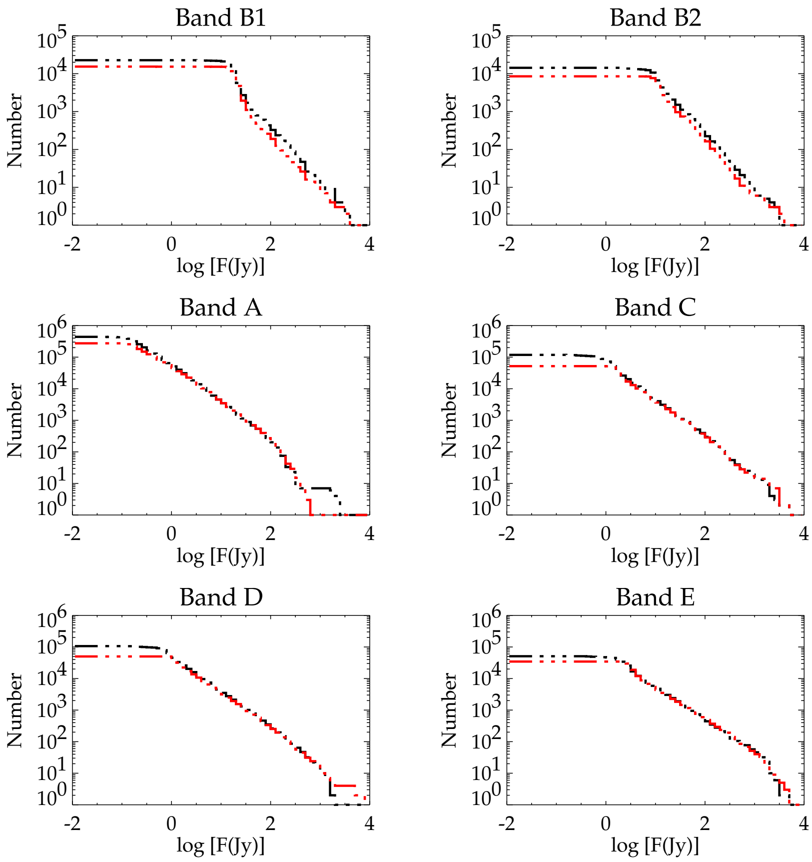

Figure 47: Cumulative source counts for confirmed V1.2 sources (red) compared to those in V2.3 (black).

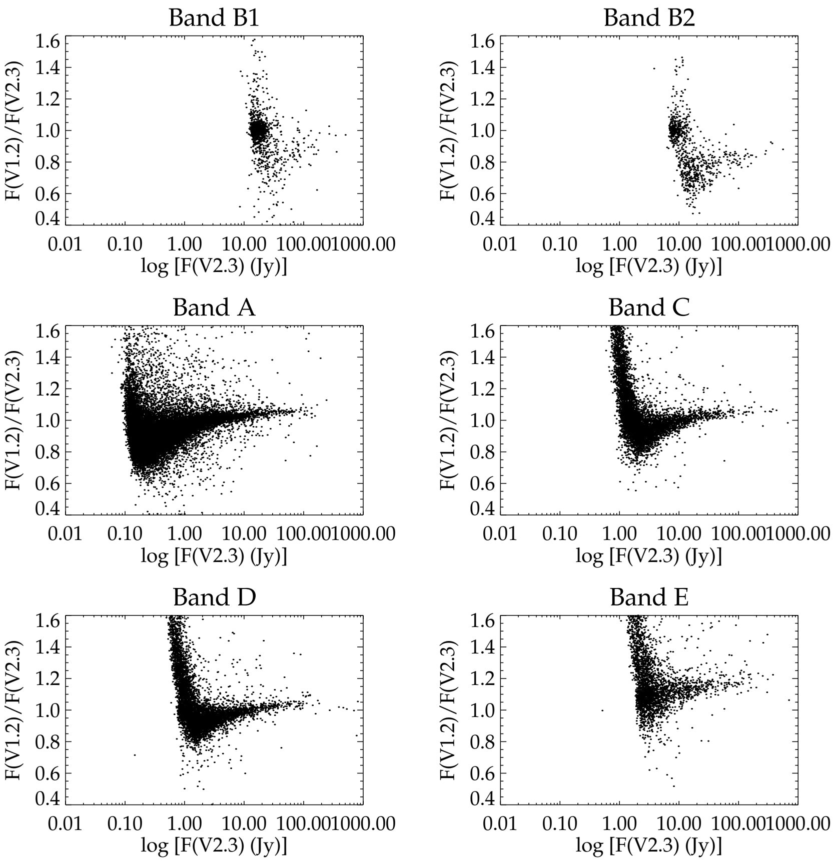

Figure 48: $F_{V1.2}/F_{V2.3}$ vs. $F_{V2.3}$ for all MSX bands.

6.2 Emission Ridge Line Sources

The Band A images show that within $\pm 1\overset{\circ}{.}5$ of the Galactic equator, the background is dominated by bright, highly structured diffuse emission. To the point source extractor, knots in this emission may appear to be point-like. In some areas, notably the Cygnus region, we often see point sources in a line along a ridge of emission. Whether there are actually embedded objects in these knots is not known. In V2.3, most of these appear in the low reliability file, as the background and noise estimation for the image-based flux extraction tends drive SNR_{im} lower than expected based on SNR_{PSX}.

References

[1] Beichman, C. A., Neugebauer, G., Habing, H. J., Clegg, P. E., & Chester, T. J. (1988) *IRAS Catalogs and Atlases, Version 2. Explanatory Supplement*, NASA Ref. Publ. 1190

[2] Burdick, S. V., & Morris, D. C. (1997), "SPIRIT III Calibration Stars: In-Band Irrradiances and Uncertainty," *Optical Engineering*, **36**, 2971

[3] Cohen, M., Hammersley, P., & Egan, M. P. (2000), "Radiometric Validation of the Midcourse Space Experiment (MSX) Point Source Catalogs and the MSX Properties of Normal Stars," *AJ*, **120**, 3362

[4] Cohen, M., Walker, R. G., Barlow, M. J., & Deacon, J. R. (1992a), "Spectral Irradiance Calibration in the Infrared. I. Ground Based and IRAS Broadband Calibration," *AJ*, **104**, 1650

[5] Cohen, M., Walker, R. G., Carter, B., Hammersley, P., Kidger, M., & Noguchi, K. (1999), "Spectral Irradiance Calibration in the Infrared. X. A Self-Consistent Radiometric All-Sky Network of Absolutely Calibrated Stellar Spectra," *AJ*, **117**, 1864

[6] Cohen, M., Walker, R. G., Jayaraman, S., Barker, E., & Price, S. D. (2001), "Spectral Irradiance Calibration in the Infrared. XII. Radiometric Measurements from the Midcourse Space Experiment (MSX)," *AJ*, **121**, 1180

[7] Cohen, M., Walker, R. G., Witteborn, F.C. (1992b), "Spectral irradiance calibration in the infrared. II - Alpha Tau and the recalibration of the IRAS low resolution spectrometer," *AJ*, **104**, 2030

[8] Egan, M. P., & Price, S. D. (1996), "The MSX Infrared Astrometric Catalog," *AJ*, **112**, 2862

[9] Egan, M. P., Price, S. D., Moshir, M. M. Cohen, M. Tedesco, E. F., Murdock, T. L., Zweil, A., Burdick, S., Bonito, N., Gugliotti, G. M., & Duszlak, J. (1999), *MSX Point Source Catalog Explanatory Guide Version 1.2*, AFRL-VS-TR-1999-1522, Air Force Research Laboratory, AD-A381933

[10] Egan, M. P. Van Dyk, S. D., & Price, S. D. (2001), "MSX, 2MASS and the LMC: A Combined Near- and Mid-Infrared View," *AJ*, **122**, 1844

[11] Garlick, D. S., Greenman, M., Larsen, M. R., Sargent, S., & Hanson, J. S. (1996), "Algorithms for Calibration and Point Source Extraction for an LWIR Space Based Sensor," *Proc. SPIE*, **2759**, 182

[12] Hanson, S., Peterson, J., & Tansock, J. (1998), "Radiative Spectral Response Reference Detector Updates," in *Proc. SDL/USU Symposium on Infrared Radiometric Calibration Sept 22–24, 1998* (available from USU/SDL)

[13] Høg, E., Fabricius, C., Makarov, V. V., Bastian, U., Schwekendiek, P., Wicenec, A., Urban, S., Corbin, T., & Wycoff, G. (2000), "Construction and Verification of the Tycho-2 Catalogue," *A&A*, **357**, 267

[14] Kleinmann, S. G., Cutri, R. M., Young, E. T., Low, F. J., & Gillett, F. C. (1986) *IRAS Serendipitous Survey Catalog* (U.S. GPO: Washington DC)

[15] Kraemer, K. E., Price, S. D., Mizuno, D. R., & Carey, S. J. (2002), "Observations of Galaxies with the Midcourse Space Experiment," *AJ*, **124**, 2990

[16] Kraemer, K. E., Shipman, R. F., Price, S. D., Mizuno, D. R., & Kuchar, T. (2003), "Observations of Star-Forming Regions with the Midcourse Space Experiment," *AJ*, **126**, 1423

[17] Larsen, M. F., & Sargent, S. D. (1997), "Temperature-Dependent Linearity Calibration for the SPIRIT III Radiometer," *Opt. Eng.*, **36**, 2956

[18] Lumsden, S. L., Hoare, M. G., Oudmaijer, R. D., & Richards, D. (2002), "The Population of the Galactic Plane as Seen by MSX," *MNRAS*, **336**, 621

[19] Mazuk, S., & Lillo, W. (1998) "Applications of Neural Networks to Modeling the Point Response for the Spatial InfraRed Imaging Telescope III (SPIRIT III) Radiometer," in *Proc. SDL/USU Symposium on Infrared Radiometric Sensor Calibration Sept 22–24, 1998* (available from USU/SDL)

[20] Moshir, M., Kopman, G, & Conrow, T. A. O. (1992), *IRAS Faint Source Survey Explanatory Supplement Version 2* (IPAC: Pasadena)

[21] Pratt, W. K. (1991), *Digital Image Processing, Second Edition*, (Wiley-Interscience: New York)

[22] Pratt, W. K., Cooper, T.J., & Kabir, I. (1984), "Pseudomedian Filter" in *Proc. SPIE Conf.*, Los Angeles, CA, January 1984

[23] Press, W. H., Teukolsky, S. A., Vetterling, W. T., & Flannery, B. P. (1992), *Numerical Recipes in Fortran, 2e*, (Cambridge University Press: Cambridge)

[24] Price, S. D., Egan, M. P., Carey, S. J., Mizuno, D. R., & Kuchar, T. A. (2001), "MSX Survey of the Galactic Plane," *AJ*, **121**, 2819

[25] Price, S. D., & Kraemer, K. E. (2004), "Background Sources for Calibrating Space-Based Sensors," *AIAA Conference Proc.*, in press

[26] Price, S. D., Noah, P. V., Mizuno, D. R., Walker, R. G., & Jayaraman, S. (2003), "Midcourse Space Experiment Mid-Infrared Measurements of the Thermal Emission from the Zodiacal Dust Cloud," *AJ*, **125**, 962

[27] Sargent, S. D. (1997), "Temperature-Dependent Responsivity Correction for the SPIRIT III Radiometer," *Opt. Eng.*, **36**, 2948

[28] Thurgood, V. A., Larsen, M. F., & Sargent, S. D. (1998), "SPIRIT III Ground Calibration Overview," presentation in *Proc. SDL/USU Symposium on Infrared Radiometric Sensor Calibration Sept 22 – 24 1998* (Available from USU/SDL)

[29] Wainscoat, R. J., Cohen, M., Volk, K., Walker, H. J., & Schwartz, D. E. (1992), "A Model of the 8–25 μm Point Source Infrared Sky,"*ApJS*, **83**, 111

[30] Wright, C. O., Egan, M. P., Kraemer, K. E., & Price, S. D. (2003), "The Tycho-2 Spectral Type Catalog," *AJ*, **125**, 359

[31] Wright, C. O., Egan, M. P. & Price, S. D. (2002), "A Tycho-2 Based Infrared Astrometric Catalog," *2002 AMOS Technical Conference Proceedings*, in press

Acronyms

AFRL	-	Air Force Research Laboratory
APC	-	Attitude Processing Center
APL	-	Applied Physics Laboratory
CB	-	Celestial Background experiment
CHE00	-	Cohen, Hammersley, and Egan (2000)
COBE	-	Cosmic Background Experiment
CWW	-	Cohen, Walker, and Witteborn
DAC	-	Data Analysis Center
DAF	-	Definitive Attitude File
DCATT	-	Data Certification and Technology Team
DCE	-	Data Collection Event
Dec	-	declination
DPC	-	Data Processing Center
ECI	-	Earth Centered Inertial
EFOV	-	effective field-of-view
FSC	-	IRAS Faint Source Catalog
FSR	-	Faint Source Reject File
IAU	-	International Astronomical Union
IRAS	-	Infrared Astronomy Satellite
ISO	-	Infrared Space Observatory
JHU	-	Johns Hopkins University
LMC	-	Large Magellanic Cloud
MAD	-	mean absolute deviation
MCC	-	Mission Control Center
MIC2	-	Multifunctional Infrared Calibrator 2
MPC	-	Mission Planning Center
MSX	-	Midcourse Space Experiment
NASA	-	National Aeronautics and Space Agency
NIST	-	National Institute for Standards and Technology
PAT	-	Performance Assessment Team
PI	-	Principal Investigator
PRF	-	point response function
PSC	-	Point Source Catalog
PSF	-	point spread function
PSX	-	Point Source Extractor
RA	-	right ascension
RIP	-	Radiometer Instrument Product
RMS	-	root-mean-squared
RSR	-	relative spectral response
RSS	-	root-sum-squared
SDL	-	Space Dynamics Laboratory
SMC	-	Small Magellanic Cloud
SNR	-	signal-to-noise ratio
SPIRIT III	-	Spatial Infrared Imaging Telescope III
SSC	-	IRAS Serendipitous Survey Catalog
USU	-	Utah State University
2MASS	-	2 Micron All Sky Survey